

Metamodel-based methodology for fast prediction of human exposure to high power systems

Métamodélisation pour le calcul rapide d'exposition des personnes aux systèmes haute puissance

Thèse de doctorat de l'université Paris-Saclay et de l'université Politecnico di Torino

n°575 : electrical, optical, bio : physics and engineering (EOBE)
Spécialité de doctorat : Génie électrique

Graduate School : Sciences de l'ingénierie et des systèmes. Référent : CentraleSupélec

Thèse préparée dans les unités de recherche **Laboratoire de Génie Electrique et Electronique de Paris , Université Paris-Saclay, CentraleSupélec, CNRS**, sous la direction de **Lionel Pichon**, Directeur de Recherche CNRS, et **Department of Energy "G. Ferraris", Politecnico di Torino**, sous la direction de **Fabio Freschi**

Thèse soutenue à Paris-Saclay, le 27 mars 2023, par

Paul LAGOUANELLE

Composition du Jury

Membres du jury avec voix délibérative

Alain Reineix Directeur de Recherche, XLIM	Président, Rapporteur & Examineur
Giambattista Grusso Professor, Politecnico di Milano	Rapporteur
Eric Labouré Professeur des Universités, GeePs	Examineur
Luca Giaccone Professor, Politecnico di Torino	Examineur

Declaration

I hereby declare that, the contents and organization of this dissertation constitute my own original work and does not compromise in any way the rights of third parties, including those relating to the security of personal data.

Paul Lagouanelle
2023

I would like to dedicate this thesis to my mother

Acknowledgements

I would like to acknowledge the great help of many people who helped me throughout this long journey.

First of all, I wish to thank Lionel Pichon, my French supervisor, who offered me the opportunity to work with him and kept providing me with useful guidance and great support for the development of my research. The same feeling goes to Fabio Freschi, my Italian supervisor, who welcomed me with open arms at PoliTO and enhanced the range of possibilities on my thesis work.

Then, I would like to thank all the good people I had the chance to work with. Oriano Bottauscio and Mauro Zucca at the INRiM in Torino, for providing us a new model to develop our numerical methods on. Giulia Di Capua, Nicola Femia, Antonio Maffucci and Salvatore Ventre from UNICAS and UNISA for their collaboration on their dynamical WPT model on which I first tried my algorithm on. Wassim Kabbara and Mohamed Bensetti for the use of their experimental setup at the GeePs with the measurements conducted by Chloé Bourion and German Orlov. Luca Giaccone at PoliTO, who really made me discover human exposure assessment and helped me on the matter more than once. My friend and colleague Charles Boulitrop along with his supervisor Marc Lambert for our common work at the GeePs on innovative optimization methods for WPT systems.

I got a special thank to give to my former colleague and friend Vincenzo Cirimele who not only was my great office mate for a year but also showed me his way around the beautiful city of Torino. Without him, my year in Italy would have been completely different. On the same matter I want to thank my long term friend Elisa Zanchi along with our common friend Federico Bertin who both welcomed us at Torino and made our stay in Italy

never-to-be-forgotten. I would like to express my gratitude to the group at the Department of Energy at PoliTO who made us feel at home even if the Covid broke the fun, Maurizio, Aldo, Paolo along with all the PhD students there: Alessandro, Michele, Luigi, Angela... My Italian teacher Mariella along with my friends who helped me practice when I was not in Italy: Davide and Mattia.

This work would not have been possible without all the people making GeePs and the Department of Energy at PoliTO up and running every day. Many thanks to Pia in Italy who greatly helped us at the start. In the Geeps, I would like to thank particularly Sylvie for her dedicated work at managing my missions, Séverine for all her help, along with Léonor, Nathalie, Claude and Philippe. Huge thanks to the information technology team Olivier and Anthony along with our computing engineer Laurent for their help on a daily basis. I would also like to thank Adrien Mercier, my senior office mate and Xavier Mininger, who both helped me from time to time during the writing of my PhD.

My deeper thoughts are for the people who helped me enjoy my third year after the difficult time I faced during the COVID-19 outburst. The point K team with Koffi, Guillaume, Nicolas, Kokouvi, Tanbir, Charles... along with all the other PhD students or post-doctoral fellows at the GeePs. Thomas, Jennifer and Benjamin for my never-ending Tuesdays at the ENS along with all of my old PHYTEM team: Rémi, Piwi, Arthur, Théo, Benjamin, Haëck, Pellet and Charlie.

Finally, I would like to deeply thank my girlfriend Jessie, as well as my mother and my grand-father, who have always been by my side throughout this amazing journey.

Abstract

Keywords: Sensitivity analysis, inductive power transfer, human exposure

Wireless power transfer systems (WPT) are a key factor in the development of electric mobility. Such high power systems create a high level of magnetic field in the vicinity area, which can be dangerous for operators or bystanders. Thus, when designing new WPT systems, the human exposure needs to be properly assessed in order to be compliant with the current standards and guidelines.

The work presented here used non-intrusive stochastic tools to build a consistent predictor of complex computational models. The resulting predictor is a metamodel which is simply an analytical function that can be used afterwards to perform fast computation on the outputs of the real model such as Sobol'-based sensitivity analysis or optimization. Based on initial observations on basic metamodels for both simplified and realistic WPT systems, an active learning metamodeling algorithm has been developed to build consistent predictor and perform accurate sensitivity analysis at a low computation cost. The algorithm has been validated for the evaluation of mutual inductance in the case of dynamic charging. Consistent predictors have been computed for a realistic WPT computational model which have been used to optimize its design of 3F3 ferrite cores (position and dimension).

Finally, a dosimetric methodology for assessing the safety of WPT systems at a low computation cost, using the adaptive algorithm coupled with a voxelized 3D human model, has been developed. Safety areas for a simulated WPT system and a practical system available at the GeePs have been computed. The methodology has been applied to a system needier of human exposure assessment: mid-frequency Direct Current welding guns, treating the case of exposure to a pulsed magnetic field.

Contents

List of Figures	xi
List of Tables	xviii
1 Introduction	1
2 Sensitivity analysis for high-power systems: technical evolution	4
2.1 The importance of uncertainty analysis for high-power systems	5
2.1.1 Parameters variability for the design of high-power systems	6
2.1.2 Dangers of human exposure to electromagnetic fields	7
2.2 Human exposure to low-frequency electromagnetic fields . .	11
2.2.1 Guidelines and standards	12
2.2.2 Human models	14
2.3 Development of sensitivity analysis	16
2.3.1 Classical sensitivity analysis computations	16
2.3.2 Global sensitivity analysis for complex models	17
2.4 A possible solution: metamodelling	20
2.4.1 Surrogate models	21
2.4.2 Metamodelling for sensitivity analysis	24
2.4.3 Metamodels for computational electromagnetics . . .	28

3	Metamodelling for electromagnetic systems	30
3.1	Surrogate models	30
3.1.1	Kriging: a Gaussian process	31
3.1.2	Polynomial Chaos expansion	35
3.1.3	Polynomial Chaos-Kriging metamodel	38
3.1.4	A posteriori error estimation	38
3.1.5	Sobol' indices	40
3.1.6	PCE-based sensitivity analysis	44
3.2	Analysis of a simplified WPT model	45
3.2.1	Description of the first input model	45
3.2.2	Kriging: trends and correlation functions tuning	48
3.2.3	Truncation schemes and computation of Polynomial Chaos-based metamodels	53
3.2.4	Polynomial Chaos-Kriging metamodel parameters	56
3.3	A realistic car model	61
3.3.1	The INRiM model	61
3.3.2	Sub-sampled metamodels	62
3.4	Conclusions	68
4	Active learning metamodelling	70
4.1	Subgridding technique	70
4.1.1	Adaptive sampling strategy	71
4.1.2	Base algorithm	75
4.1.3	Comparison of sampling methods	76
4.2	Accurate sensitivity analysis for a dynamic WPT system	82
4.2.1	The input model	82
4.2.2	Dynamic charging applications with one TX coil	84

4.2.3	Dynamic charging applications with two TX coils . . .	87
4.2.4	Best sensitivity analysis	89
4.2.5	Discussion on the parameters ε and m	91
4.2.6	Higher input dimensions	94
4.2.7	Performance	96
4.3	Multi-parameter predictor for a complex WPT charger model	97
4.3.1	Modelling a realistic WPT model	98
4.3.2	Consistent predictor and sensitivity analysis	99
4.4	Multi-objective ferrites optimisation	105
4.4.1	Optimisation method	105
4.4.2	Optimisation problem	107
4.4.3	Results	109
4.5	Conclusions	114
5	Human exposure assessment	117
5.1	Exposure to a standardized WPT charger	119
5.1.1	Posture analysis	120
5.1.2	Sensitivity analysis regarding the position of the human body around the charger	123
5.2	Exposition to an MFDC spot welding gun	127
5.2.1	Simple model for a welding gun	128
5.2.2	Multi-frequency metamodelling	130
5.2.3	Compliance safety areas	135
5.3	Exposure to a practical WPT system	142
5.3.1	Experimental WPT system	142
5.3.2	Magnetic field mapping	143
5.4	Conclusions	150

6 Conclusion

153

References

156

List of Figures

1.1	Flux lines of stray magnetic field around IPT coils. Stray field represents either leakage field or coupling field depending on the distance to the coils. Taken from [1].	2
2.1	Overview of electronic power devices (taken from [3])	5
2.2	EMF Exposure at the Workplace, Common Applications Resulting in EMF Emission, taken from Hansson Mild et al. in [10]	10
2.3	Comparison between the exposure limits for the magnetic flux density of ICNIRP guidelines 1998 [18] and 2010 [19] for both public and occupational exposure in the frequency range (1 Hz – 10MHz)	12
2.4	Overview of some Virtual Population (ViP) models developed at the IT'IS Foundation [27]	15
2.5	Example of the Morris method on the analytical function $f(X) = x_1 + x_2^2 + x_2 \sin(x_3) + 0.1x_4$ taken from https://mogp-emulator.readthedocs.io/en/latest/methods/exam/ExamScreeningMorris.html using four levels of a given OAT design (20 total samples)	18
2.6	Basic principles of a metamodelling process, Cheng et al. [48]	22
3.1	Example of a kriging metamodel for predicting the function $f: x \rightarrow \frac{1}{x^2}$	32
3.2	Example of a PCE metamodel for predicting the function $f: x \rightarrow \sqrt{x^3 + 1}$	36

3.3	Our COMSOL model based on the WPT system studied in Vincenzo Ciremele's PhD [85]	46
3.4	Mesh of our COMSOL model	47
3.5	Position of the COMSOL probe to measure the magnetic field ($x = 50\text{cm}$, $y = 50\text{cm}$ and $z = 1\text{m}$)	49
3.6	Kriging metamodel on the COMSOL model for a sweep on the shield conductivity for various trends	50
3.7	Kriging metamodel on the COMSOL model for a sweep on the shield conductivity for various correlation families	52
3.8	Extreme values (0 to 0.5m) for the receiver position on the COMSOL model	53
3.9	PCE metamodel on the COMSOL model for a 2-D sweep (25 datapoints) on the shield conductivity and the receiver position	54
3.10	PCE metamodel on the COMSOL model for a 2-D sweep (100 datapoints) on the shield conductivity and the receiver position with the maximum allowed degree $p = 14$	54
3.11	Magnitude of the coefficients in the PCE metamodel of a 2-D sweep against the polynomial degree p	55
3.12	PCK metamodel on the COMSOL model for a 2-D sweep (25 datapoints) on the shield conductivity and the receiver position	57
3.13	PCK metamodel on the COMSOL model for a 2-D sweep (100 datapoints) on the shield conductivity and the receiver position	57
3.14	Investigation line (in red) on COMSOL for a typical bystander position, 10 values along $x = 50\text{ cm}$, $y = 50\text{ cm}$ and $z = 0$ to 2 m	59
3.15	Chosen samples in the parameter space for the accuracy comparison of PCK metamodels on a 3-D sweep: 27 (on the right) and 127 datapoints (on the left)	59
3.16	INRiM WPT car model (credits to Oriano Bottauscio and Mauro Zucca)	61
3.17	Different coil and measure positions available in the INRiM model	62

3.18	FEM mesh model of the INRiM model with the central position and the investigation line	62
3.19	Distribution of the different samples in the parameter space for our first dataset	64
3.20	Distribution of the different random sub-samples in the parameter space for the considered bidimensional sweep	64
3.21	B-field along the investigation line for the model with 39/78 datapoints (estimated) against the one with the full dataset (input model) for a given datapoint	67
4.1	Visual representation of different sampling strategies, taken from [88]	71
4.2	Flowchart of an active learning metamodelling process, with the blue processes being the computationally expensive steps	72
4.3	Test functions for comparing sampling methods on our sub-gridding algorithm	78
4.4	Test functions for comparing sampling methods on our sub-gridding algorithm	79
4.5	Test functions for comparing sampling methods on our sub-gridding algorithm: $n_{samples}$ against the <i>LOO</i> of the computed PCK metamodel	81
4.6	Different trajectories of the RX coil moving along two TX coils. The nominal trajectory is represented by a red arrow.	83
4.7	Mutual inductance values for a single pair RX-TX against the longitudinal displacement Δy and the lateral misalignment Δz for any trajectory (with $m = 4$ and $\varepsilon = 10^{-3}$)	85
4.8	Parameter domains and relevant samples used to build the metamodel for the mutual inductance for a single pair RX-TX against the longitudinal displacement Δy and the lateral misalignment Δz for any trajectory (with $m = 4$ and $\varepsilon = 10^{-3}$)	86

4.9	Mutual inductance values for a single RX coil and two TX coils against the longitudinal displacement Δy and the lateral misalignment Δz for any trajectory (with $m = 4$ and $\varepsilon = 10^{-3}$)	87
4.10	Parameter domains and relevant samples used to build the metamodel for the mutual inductance for a single RX coil and two TX coils against the longitudinal displacement Δy and the lateral misalignment Δz for any trajectory (with $m = 4$ and $\varepsilon = 10^{-3}$)	88
4.11	Percentage error of the metamodel predictor build with any trajectory against the values from the dataset 1 and 2 (with $m = 4$ and $\varepsilon = 10^{-3}$)	90
4.12	Mutual inductance values for a single RX coil and two TX coils against the longitudinal displacement Δy and the lateral misalignment Δz for any trajectory (with $m = 3$ and $\varepsilon = 0.5$)	92
4.13	Parameter domains and relevant samples used to build the metamodel for the mutual inductance for a single RX coil and two TX coils against the longitudinal displacement Δy and the lateral misalignment Δz for any trajectory (with $m = 3$ and $\varepsilon = 0.5$)	92
4.14	Percentage error of the metamodel predictor build with any trajectory against the values from the dataset 1 and 2 (with $m = 3$ and $\varepsilon = 0.5$)	93
4.15	Reciprocal position of the two coils given by the coordinates $(\Delta x, \Delta y, \Delta z)$ of the RX coil center with respect to the TX coil center point, and a by rotation angle α , taken from [100]	94
4.16	Mutual inductance values from the GP input model (blue) and the predictor (green) for the Dataset T	96
4.17	Percentage error of the metamodel predictor against the GP model value	96
4.18	CAD model of the main components of the receiver structure from [85]	98

4.19	COMSOL model for the complete PoliTO model with 3F3 ferrites cores and an optimized shielding structure	99
4.20	Variations of the coupling factor k against the z misalignment Δz and the roll γ ($\Delta x = \Delta y = 0$ m and $\alpha = \beta = 0^\circ$)	101
4.21	Relevant geometrical parameters in the plane (x, z) for the optimisation problem on the COMSOL model displayed on figure 4.19	109
4.22	Optimised geometry for the 3F3 ferrites cores for the complete PoliTO WPT model for maximizing the coupling factor k	110
4.23	Pareto front for the multi-objective optimisation to minimize the ferrite volume V and maximize the coupling factor k	112
4.24	Chosen optimised geometry (arbitrary coil misalignments) for the 3F3 ferrites cores for the complete PoliTO WPT model for maximizing the coupling factor k and minimizing the ferrite volume V	113
4.25	Percentage gain for the coupling factor k with the optimized geometry from the coupling factor with the nominal geometry k_0 against the misalignments Δx and Δy	114
5.1	Cut plane (a) and 3D view (b) of the WPT3 (class Z3) system taken from from the SAE J2954 standard [117]	119
5.2	WPT3/Z3 system model from SAE J2954 (maximum misalignment between the coils) with the investigation area (blue box of $1.2\text{ m} \times 1.2\text{ m} \times 1.8\text{ m}$ along the x, y and z axis)	120
5.3	Investigated positions for the human exposure around the WPT3/Z3 charger displayed with Sim4Life	122
5.4	PCK metamodel ($n_{samples} = 35, LOO = 0.1945$) of $EI_{\max}(x, y)$ for various positions of a crouched operator around the WPT3/Z3 system (black rectangle)	125
5.5	Working area where welding operations are performed (a) with an MFDC welding gun (b), taken from [121]	127

5.6	Real welding current pulse measured at PoliTO (in blue) with the simplified pulse considered in our simulation (in red) (a), original and simplified spectrum of the measured current pulse with the black line at 1% of the fundamental (b)	128
5.7	Simplified spectrum for the MFDC current pulse with all the components below 0.5% of the fundamental ignored	129
5.8	Duke's model for the operator facing the rectangular current loop (in blue) from the MFDC spot welding gun	130
5.9	Gain (a) and phase (b) of the WPM filter for CNS tissue of the head in the case of an occupational exposure (blue) and general exposure (red) for the induced E-field	131
5.10	Variation of the conductivity against the frequency for the considered tissues in the exposure analysis	134
5.11	Vicinity area considered for the exposure problem behind the MFDC welding gun	135
5.12	Weighted peak method for the skin for two different positions (a) and (b) around the MFDC spot welding gun (the limit at $I_{WP} = 1$ is displayed in red)	137
5.13	Variation of the exposure index and safety area ($\max(I_{WP}^i) < 1$) behind the MFDC welding gun for occupational exposure (a) and general public exposure (b)	138
5.14	Variation of the exposure factor and safety area ($I_{WP} < 1$) behind the MFDC welding gun for the different tissues investigated in the case of general exposure	141
5.15	WPT structure developed by Wassim Kabbara at the GeePs (a) and its corresponding COMSOL model (b)	143
5.16	Bench for measuring the magnetic field around the working WPT charger with the WAVACONTROL SMP2 probe	144
5.17	Points around the charger where the magnitude of the B-field has been measured with the WAVACONTROL SMP2 probe	145

5.18	Magnitude of the B-field predicted with the PCK metamodel (sampling points in red) for the experimental WPT structure (in black) on various cut planes at $P_{output} = 600\text{ W}$	147
5.19	Magnitude of the B-field predicted with the exposure limit for the experimental WPT structure (in black) on various cut planes for $P_{output} = 3\text{ kW}$ (scaled up)	149
5.20	Safety area ($B < 27\text{ }\mu\text{T}$) around the WPT structure at $P_{output} = 3\text{ kW}$ (scaled up)	150

List of Tables

2.1	Comparison of the Sobol' indices estimated by Monte Carlo sampling of a real flood model ($n_{samples} = 7 \cdot 10^7$ model evaluations) with the same SA performed on a Kriging metamodel built with $n'_{samples} = 100$ model evaluations, taken from [37]	21
2.2	Commonly used metamodeling processes: sampling methods, surrogate techniques and fitting criteria (based on an early review in 2006 by Wang and Shan [53])	24
3.1	Commonly used trends	34
3.2	Classical univariate polynomial families [81]	37
3.3	Dimensions of our first COMSOL model (see figure 3.3)	47
3.4	Input dataset for our first metamodel (rounded to two digits)	48
3.5	Properties of the output metamodels on the 3-D sweep ($S_{\mu_r} = 0$ at 3 significant figures)	60
3.6	First dataset from the INRiM model: 24 datapoints with the conductivity of the chassis σ , the relative permeability of the chassis μ_r and the relative permeability of the ferrites μ_f	63
3.7	Properties of the output PCK metamodels on the bidimensional sweep from the INRiM (OSE=NaN for the full experimental design, see equation 3.19)	65
3.8	LOO, OSE and Sobol sensitivity analysis for the sub-samples metamodels on the INRiM 3-D sweep	66

3.9	LOO, OSE and Sobol sensitivity analysis for our second meta-models	67
4.1	Coefficient values for the model given in equations 4.3 and 4.4	84
4.2	Sobol index analysis of the mutual inductance for a single pair RX-TX, against Δy and Δz (with $m = 4$ and $\varepsilon = 10^{-3}$) . . .	86
4.3	Sobol index analysis of total mutual inductance over two TX coils, against Δy and Δz for various trajectories (with $m = 4$ and $\varepsilon = 10^{-3}$)	89
4.4	Validation errors R^2 on the values from datasets 1 and 2, against the metamodel predictors built with various trajectories.	90
4.5	80 coils misalignment conditions (validation dataset T) . . .	94
4.6	Sobol analysis of the mutual inductance of 2 coils against the vertical distance Δx , the lateral misalignment Δz and the rotation α of the RX coil around the x-axis	95
4.7	Relevant parameters tunable in the complete COMSOL model (the system coordinates are specified on figure 4.19)	100
4.8	Parameters with their corresponding ranges for the analysis of a dynamic WPT system ($LOO \simeq 3.002 \cdot 10^{-2}$, $n_{samples} = 65$)	102
4.9	Parameters with their corresponding ranges for the analysis of a dynamic WPT system ($LOO \simeq 1.410 \cdot 10^{-2}$, $n_{samples} = 17$)	103
4.10	Parameters ranges for the model displayed on figure 4.21 . . .	108
4.11	Optimized parameters for maximizing the coupling factor k with their Sobol' indices ($LOO \simeq 6.907 \cdot 10^{-10}$, $n_{samples} = 517$)	110
4.12	Optimized parameters for maximizing the coupling factor k and minimizing the ferrite volume V with their Sobol' indices ($LOO \simeq 3.698 \cdot 10^{-5}$, $n_{samples} = 35$)	111

5.1	Maximum, 99.9 th percentile and volume-averaged induced E-field (V m^{-1}) in the whole body and the pelvis area for the three studied postures exposed to the WPT3/Z3 charger . . .	121
5.2	Relevant tissues considered in our WPM analysis with the number of studies in the literature used to build the low frequency dielectric model in the IT'IS database [28]	134
5.3	Sensitivity analysis for the 99.9 th percentile induced E-field in the relevant tissues considered in our WPM analysis against the position of the human body behind the welding gun ($n_{samples} = 28$, mean $LOO = 5.454 \cdot 10^{-2}$)	136
5.4	Material parameters of the coils in the WPT system studied at the GeePs (at 85 kHz)	142
5.5	Sensitivity analysis and consistency of the PCK metamodels built from the experiments on the real WPT structure at the GeePs	146

Chapter 1

Introduction

Since the end of the Second World War, the development of electronic devices has been growing constantly to their omnipresence in our daily life nowadays. As population are constantly exposed to electromagnetic fields (EMFs), both inside (household appliances) and outside their homes (power lines, communication devices...), proper standards had to be defined accordingly regarding the human exposure. Although the human exposure to EMFs from various communication devices (GSM, RF, WiFi...) has already been widely studied, the levels of vicinity fields around many high power electromagnetic devices are yet to be properly assessed.

Indeed, the case of an inductive power transfer (IPT) system is displayed on figure 1.1 where the magnetic flux lines have been drawn. If the levels of stray magnetic field are important, it can be seen that a bystander position might be dangerous due to the induced EMFs. This work aims at exploring the uncertainty quantification of human exposure around such high power systems. An adequate knowledge of the exposure can be used to develop mitigation solutions to insure the safety of the device.

Due to the complexity of both human models and realistic inductive power transfer system models, complete and detailed computations of human exposure can lead to extremely long simulations. Thus, the goal is to combine non-intrusive stochastic methods to save a lot of computation time on our complex models. The resulting predictors can then be used

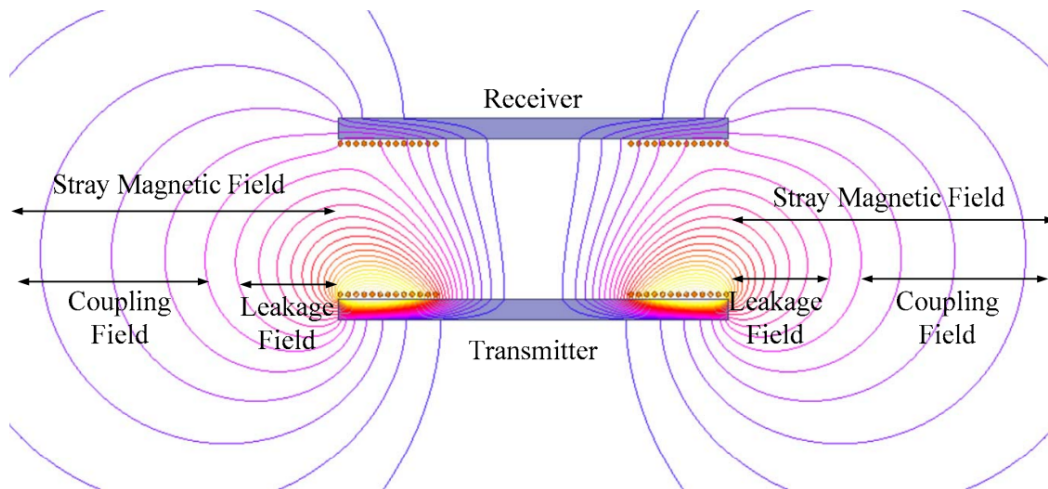


Fig. 1.1 Flux lines of stray magnetic field around IPT coils. Stray field represents either leakage field or coupling field depending on the distance to the coils. Taken from [1].

for various analysis: sensitivity analysis, optimization, development of mitigation solutions...

Firstly, a proper definition of the need for accurate sensitivity analysis on complex models will be detailed in chapter 2. To link this to human exposure, the computation of induced field quantities within the human body (dosimetric analysis) will be presented shortly and positioned regarding the existing standards and guidelines for human exposure to EMFs. A possible solution to reduce the great computation time for such global sensitivity analysis will also be presented: the metamodelling processes.

Then, in chapter 3, the different surrogate metamodelling used in our analysis are described: Kriging, Polynomial Chaos expansion (PCE) and Polynomial Chaos - Kriging (PCK). These metamodelling are compared in terms of consistency and Sobol-based sensitivity analysis. A first case of a simplified WPT system is treated for various dimensionalities. The results have been extended to a realistic car model needier of cheap computation time. These analysis showed the usefulness of surrogate models on two different WPT models but also the need to develop an adequate sampling strategy to greatly reduce the total computation time.

Therefore, chapter 4 is explaining the development of an adaptive algorithm for computing fastly a consistent metamodelling, where various sampling

strategies are compared on different test functions. The active learning metamodelling algorithm is validated on an analytical mutual inductance model for dynamic WPT charging but also a realistic WPT system computational model. The use of the resulting predictor for a trade-off optimization design is also detailed.

Finally, in chapter 5, our algorithm has been used for various human exposure assessments. The standardized WPT3 (class Z3) model with a complex human model has been treated to find safety areas around the charging device at a low computation cost. Mitigation solutions and safety areas have also been analyzed for another kind of high power system, needier of human exposure assessment: a mid-frequency direct current (MFDC) welding gun. Some experimental data from an existing WPT coupler for dynamic charging available in our research group has also been treated in the case of human exposure.

Most results presented here have been developed in the framework of the EMPIR 16ENG08 MICEV Project [2]. The EMPIR initiative is co-funded by the European Union's Horizon 2020 research and innovation program and the EMPIR participating States. This work has also been made possible by the French-Italian University with the help of the Vinci scholarship program.

Chapter 2

Sensitivity analysis for high-power systems: technical evolution

This chapter will first be explaining the importance of accurate sensitivity analysis for uncertainty quantification of electromagnetic problems and especially for estimating the levels of human exposure to electromagnetic fields. Such exposure problems are becoming more and more frequent due to the ongoing omnipresence of new technologies and their development.

Among the various types of EMF exposures, the applications studied here are focusing on low-frequency (LF) fields which can lead to severe damages on human bodies if the field levels are too high. Thus, the description of various standards and guidelines have been developed here in order to define proper limits for non-ionizing radiations. Along the development of standards followed the development of numerical models for human bodies, in order to properly estimate the induced electromagnetic quantities (dosimetric quantities) within humans.

Then, the development of sensitivity analysis is detailed which can be used to estimate the variations of such electromagnetic and dosimetric quantities. Due to obvious numerical expenses, some sensitivity analysis are impossible to compute with classical methods for complex models. Therefore, the evolution of a possible solution to complex sensitivity analysis is also discussed: the use of metamodels and particularly Kriging and Polynomial Chaos expansion.

2.1 The importance of uncertainty analysis for high-power systems

In the recent decades, due to the growth of electrical engineering for both domestic and industrial applications, the need of fast and accurate sensitivity analysis for such complex systems has been constantly increasing. An overview of existing electronic devices ranked by rated voltage and rated current is displayed on figure 2.1 (taken from [3]). From low voltage applications such as small electronic devices (phones, computers, servers...) to automotive applications, home appliances or high voltage power lines, the safety of human around such systems needs to be properly assessed.

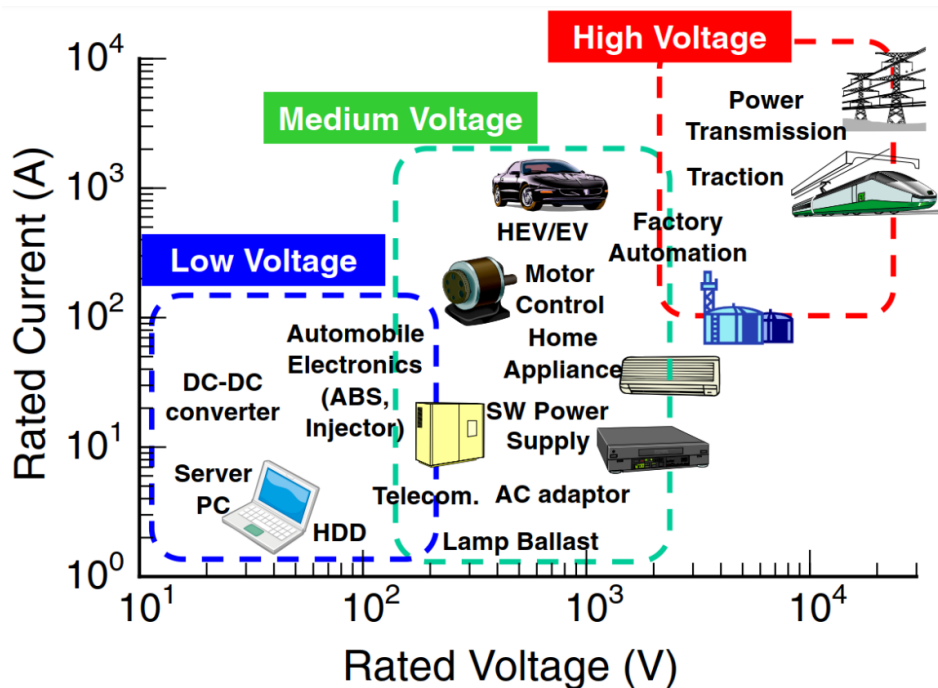


Fig. 2.1 Overview of electronic power devices (taken from [3])

For medium to high power systems, the levels of generated EMFs are greater and could represent a danger to humans in their vicinity. Consequently, these sensitivity analysis methods have been used notably to investigate the safety of such high-power systems for human exposure. The goal of such sensitivity studies is to assess the variability of a given output against several considered inputs. The output could be data from a

solver or from experimental results while the inputs are mainly the defining parameters of the device.

2.1.1 Parameters variability for the design of high-power systems

Sensitivity analysis can be used on both simulation model but also experimental prototypes in order to predict and quantify the variations of an output of interest regarding defined variations of input parameters. This can help in the design of new systems and the improvement of existing devices. Here are some examples of the use of sensitivity analysis on various systems:

- **Finding the most important parameters.** Often called **factor prioritization**, the goal of such an analysis is to identify among a given set of parameters which one has the greatest influence on the variance of the output. After identifying such a factor, a new design could imply taking a greater care at its dimensioning or insuring a lower level of uncertainty when building it. For example, in this article [4] Saltelli and Tarantola are proposing a protocol to find the input having the most influence on a considered model: the Level E model used in safety assessment for nuclear waste disposal.
- **Easily test new designs.** Once an accurate sensitivity analysis has been computed on a given set of input parameters. The knowledge of their variability ranges and their corresponding effects on the output variance can help in trying new configurations of the system. Optimisation for better performance or mitigation solution like cost reduction can be tried out. In [5], Curran, Allaire, and Willcox are performing sensitivity analysis on a high-pass filter circuit in order to identify trade-offs cost-performance solutions without performing additional model evaluations.
- **Simplifying the model.** By knowing the exact influence of all the input parameters, one can identify the non-influential parameters within the considered space design. Thus, these parameters can be fixed

at any value within their own range of variation without modifying significantly the output variance. Such screening techniques have been used for over two decades (see [6]) and can help at reducing the number of relevant parameters and thus simplify simulation model but also experimental designs.

- **Quantifying the propagation of uncertainties on input parameters.** For any system aiming at a defined level of performance, a proper accuracy on the output has to be defined. Therefore, when creating a simulation model or when building a prototype, one needs to be able to fully describe the uncertainty on the output measured (or computed). Thus, sensitivity analysis are used as a tool to propagate the known uncertainties on the various input parameters, like manufacturing uncertainty or the accuracy from measuring with sensors. For example, in [7], Oh et al. are developing a model for predicting the lifetime of electronic packages regarding the reliability of their composing electronic chips.

Therefore, for complex systems and especially high-power electronic devices, the need of an accurate sensitivity analysis is crucial. All of the sensitivity analysis examples cited earlier have been conducted on simpler or simplified models. Unfortunately for complex models, due to their dimensionality, the high interaction of input parameters and usually the non-linear responses of the model, global sensitivity analysis are extremely difficult to perform at a decent computation cost. This point will be developed later in section 2.3. Such high computation cost analysis includes notably a proper estimation of the sensitivity of human exposure within the working range of high-power devices.

2.1.2 Dangers of human exposure to electromagnetic fields

In our daily life, the human body has to be subjected to many types of electromagnetic fields, from power lines with alternative currents to radio frequencies, microwaves or WiFi. All of these EMF fall into the non-ionizing part of the spectrum, meaning they are unable to break the chemical bonds

between molecules and produce ionization. However, any non-ionizing electromagnetic wave surrounding us is interacting with the human body, whose effects are depending on the field frequency and the period of exposure. These effects can be beneficial (in the case of radio-frequency ablation for cancerous tumors for example), harmless but also extremely dangerous.

In order to properly assess such effects for a given system, the variability of the EMF properties against the various input parameters needs to be known. Hence why sensitivity analysis is crucial for defining the safety of electromagnetic systems regarding human exposure to EMFs.

Principle

From an electromagnetic point of view, our body (and any biological system) can be simply decomposed as a succession of media with varying physical properties (conductivity, permittivity) depending on the frequency. When subjected to an external electromagnetic wave, an EMF will be induced inside a given tissue and the distribution of the internal field will be dependent on both the body physiological parameters, its geometry and the properties of the incident EMF (polarization, frequency, intensity) [8].

The effects of non-ionizing EMF on the human body can be separated in two different categories according to the World Health Organisation [9]:

- **Low-Frequency EMF.** LF electric fields are modifying the charge distribution on tissue surfaces, thus, inducing electric currents within the body. While LF magnetic fields directly induce currents within the human body.
- **High-Frequency EMF.** At higher frequencies, the fields are absorbed shortly and do not penetrate much into the body due to the skin effect. However, some thermal effects are present and thus not harmless as it can cause a clear rise in the body temperature for long-term exposure.

Main dangers

From static fields (0 Hz) to X-rays ($f > 10^{16}$ Hz), all electromagnetic waves can have a hazardous impact on the human body depending on the magnitude of the incident wave and the period of exposure. Humans can face these dangers with domestic appliances at home or in public places, such exposure is called **general public exposure**, but also in the workplace with **occupational exposure** (see figure 2.2).

EMF Source	EMF Frequency Related To Application				Workers' EMF Exposure		
	Static	ELF	IF	RF/MW	Probably Low-Level*	Possibly High-Level**	Probably High-Level***
Induction heating		oo	o			xx	x
Surgical and physiotherapeutic use of diathermy			oo	oo		xx	x
Dielectric heating (RF: glue drying and plastic welding & MW: heating and vulcanization applications)				oo		xx	x
Arc-welding (MIG, MAG, TIG, etc.)	oo	oo	o			xx	xx
Spot welding	o	oo	o			xx	x
Electrochemical installations or other ones using microwaves (e.g., chemical activation of processes)				oo	NAD		
Electrolytic installations	o	oo			xx	x	
Industrial microwave ovens				oo	xx	x	
MRI medical diagnostic equipment	oo	oo		oo		xx	o
NMR spectrometers	oo			oo	x	x	x
Electric vehicles (trains, trams, metro)	o	o			xx	x	
Plasma discharge equipment				o	NAD		
Plasma polymerization at RF				o	NAD		
Radar and other systems				oo			xx
Broadcasting systems and devices (radio and TV: AM, VHF, UHF)		o	o	o	xx	x	x
Mobile telephony base stations				oo	xx	x	x
Military and research RF systems			o	oo	x	xx	x
RFID, EAS and other security equipment	o	o	o	o	xx	x	x
WLANs				oo	xx		
Cordless phones				o	xx		x
Bluetooth devices and hand-free kits				oo	xx		x
Electricity supplying networks and electricity distribution and transmission equipment	o				xx	x	
Electric handheld tools		o			xx	x	x
Industrial magnetizers demagnetizers	o	oo				x	

Notes. EMF—electromagnetic fields, ELF—extremely low frequency, IF—intermediate frequency, RF—radiofrequency, MW—microwave, MIG—metal inert gas, MAG—metal active gas, TIG—tungsten inert gas, NMR—nuclear magnetic resonance, MRI—magnetic resonance imaging, AM—amplitude modulation, VHF—very high frequency, UHF—ultra high frequency, RFID—radio-frequency identification, EAS—electronic article surveillance, WLAN—wireless local area network; NAD—no available data; oo—basic frequency range, which is in the most common use for specific applications; o—other frequencies, which can be used for specific applications; xx—the most common situation in the work environment; x—a possible situation in the work environment; *—detailed exposure assessment not necessary; **—assessment with external measures, using environmental measurements; ***—assessment with internal measures, computational assessment may be needed.

Fig. 2.2 EMF Exposure at the Workplace, Common Applications Resulting in EMF Emission, taken from Hansson Mild et al. in [10]

A common effect, yet harmless, of short-term EMF exposure can be phosphenes appearing at the external visual field. But as described by Greenebaum and Barnes in [11], humans could be at risk with much severe effects when exposed to EMFs [12]. Exposure to EMFs could lead to severe health effects such as Central Nervous System (CNS) failures, miscarriages, defection of the reproduction system... The various effects of long-term

exposure are currently extremely controversial and thus widely investigated in the literature.

In figure 2.2, various industrial applications are detailed with their most common frequency ranges and their corresponding risk of workers' exposure to EMFs. The level of high-frequency EMFs detailed here and used in both daily life and industrial applications are much lower than the ones required to cause significant heating within biological tissues. In the case of LF to intermediate frequency fields, where the common industrial applications are inductive power transfer (IPT) systems, welding processes, MRI medical equipment or industrial magnetizers/demagnetizers, the workers are exposed to EMFs which may harm human bodies if not properly assessed (Possibly High-Level of risk). Therefore, our studies have been focused on low to mid frequencies, where a proper assessment of human exposure to EMFs is more crucially needed nowadays.

2.2 Human exposure to low-frequency electromagnetic fields

In the case of LF EMF exposure, the physical effects observed within the human body are circulating currents due to Faraday's law. The corresponding dosimetric quantity is the current density \vec{J} within a tissue (conductivity σ) linked to the induced electric field \vec{E} by Ohm's law: $\vec{J} = \sigma \vec{E}$.

Historically, the use of $||\vec{J}||$ as the dosimetric quantity for the characterization of such human exposure cases was dominant in the literature as in standards. But due to recent studies (see [13]) showing the great uncertainties on the variation of tissue conductivity against the frequency, most guidelines are defining tissue exposure limits based on the magnitude of the induced electric fields $||\vec{E}||$. The considered dosimetric quantity differs for other EMF cases, for example the specific absorption rate (SAR) for radio frequencies like mobile phones exposure.

2.2.1 Guidelines and standards

Although the potential dangers of EMFs have been known for other a century (Thompson in 1910 [14]), some proper studies quantifying these dangers only started during the 60' leading to the first definition of standards on the levels of exposure for human bodies (see an early review [15] in 1972 by Michaelson). For example, the "Radiation Control for Health and Safety Act of 1968" [16] and the "Occupational Safety and Health Act of 1970" [17] in the USA.

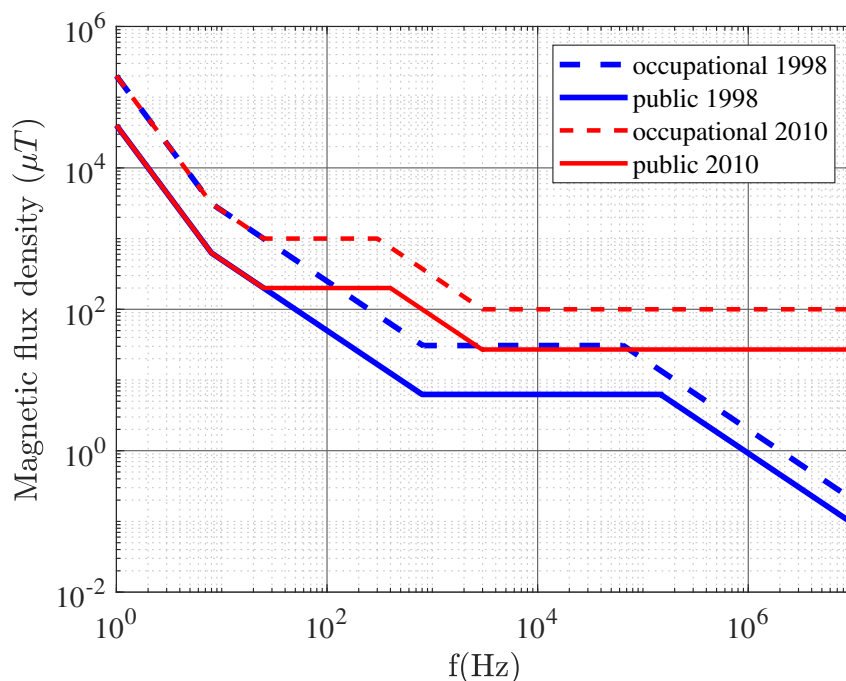


Fig. 2.3 Comparison between the exposure limits for the magnetic flux density of ICNIRP guidelines 1998 [18] and 2010 [19] for both public and occupational exposure in the frequency range (1 Hz – 10MHz)

Each country can define its own standards regarding the human exposure to non-ionizing radiations. Some huge differences could exist 50 years ago, especially between former Soviet Union countries and Western countries (a factor more than 100). But now most of national standards are following the guidelines provided by the International Commission on Non-Ionizing Radiation Protection (ICNIRP). This non-governmental organization, recognized by the world health organization (WHO), is draw-

ing exposure limits based on the existing scientific literature. The WHO is currently launching a program in order to unify existing standards for human exposure to EMFs: The International EMF Project [20] (0 – 300GHz), on which future standards will be based on.

The two main standards are the ICNIRP guidelines [18][19] for most European countries and the IEEE standards [21] in the USA. Each of these standards are defining exposure limits as thresholds for the magnetic flux density at a given frequency. Based on existing limits in the literature, the thresholds have been defined by adding a reduction factor to insure the safety of such human exposure. Both standards are defining different limits for general population exposure and workers exposure for people more aware of the dangers of EMFs. On figure 2.3, the differences between general public exposure (general population) and occupational exposure (workers exposure) have been displayed for both versions of the ICNIRP guidelines (1998 and 2010) for the frequency range (1 Hz – 10MHz). The limits have been increased and are more accurate in 2010 thanks to the progress in scientific studies on the subject between 1998 and 2010. Recently, in 2020, the ICNIRP provided new guidelines but only for the RF range (100 kHz – 300GHz) [22]. Our studies have been focusing on the ICNIRP standards and guidelines because we are using them in Europe, but all the analysis could have been performed similarly considering IEEE exposure limits or other similar standards.

The various guidelines are defining two different exposure limits to ensure the safety of human body in an EMF: a body-local quantity called the basic restriction and a derived global quantity on the outside of the body called the reference level. For every tissue type, standards are defining a basic restriction as a threshold for the considered dosimetric quantity at the given frequency. Therefore, a basic restriction is set a for every part of the human body separately. While the reference level is considering only the field outside the human body and is defining a limit which considers the smallest basic restriction in the body. Thus, if the outside field is below the reference level, the safety of every tissue type within the human body is insured. Whereas if it is over the limit, a dosimetric analysis has to be performed on every tissue type to find if the field levels are over the corresponding basic restriction.

2.2.2 Human models

Whenever an electromagnetic device is generating an EMF which is exceeding the reference levels for human exposure, the system could still be safe. Indeed, one has to compute the induced E-field within every tissue of the human body (or some part only depending on the exposure problem) and compare them to their corresponding reference level. The ICNIRP is providing reference levels for two tissue type inside the human body: Central Nervous System (CNS) tissues in the head, and all the other tissues in the head and body. Thus, in order to compute these dosimetric quantities in the whole body, some proper anatomical model of the human body had to be developed (see some detailed review in [23] by Siauve et al.).

The first human model, developed prior to the 90', were considering the human body as simple homogeneous geometries (disc, ellipsoid, cubes) with constant permittivity and conductivity (Livesay and Chen in [8] for example). Afterwards, thanks to the huge growth in computation power, some proper anthropomorphic 3D models started to be developed: Bossavit in 1993 [24], Bottauscio and Conti in 1997 [25], Dawson and Stuchly in 1998 [26].

Most 3D anatomical models available nowadays are reproducing the internal structure of the human body by discretizing it in small cubes (voxels). Usually by using tomography results and/or MRI results from patients or corpses, every voxel is assigned a tissue type with defined physical properties (permittivity, conductivity). The voxel-based anatomical models are now reproducing the human body with voxel as small as $0.5 \text{ mm} \times 0.5 \text{ mm} \times 0.5 \text{ mm}$ cubes, see the Virtual Population models from the IT'IS Foundation [27] for example. With such a high level of accuracy for the discretization, the computation can be extremely long (more than 10^{10} cells). While $1 \text{ mm} \times 1 \text{ mm} \times 1 \text{ mm}$ discretization is mostly adopted, a good compromise, suggested by the ICNIRP, is to consider it with averaging to $2 \text{ mm} \times 2 \text{ mm} \times 2 \text{ mm}$.

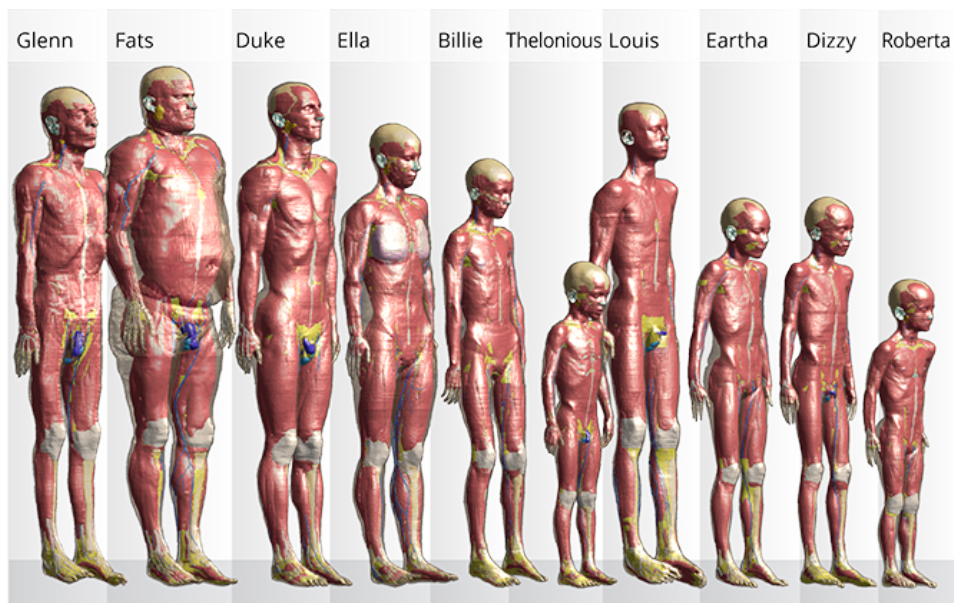


Fig. 2.4 Overview of some Virtual Population (ViP) models developed at the IT'IS Foundation [27]

Various voxelized anatomical models have been developed for different age, gender, morphology, height (see figure 2.4) but also for other species like pigs, rats and monkeys. Moreover, even if the data used to build these voxelized models are coming from standing or lying human bodies, using advanced topographical techniques these models can now be successfully manipulated to fit any possible position. This enables the study of positional human exposure around electromagnetic devices.

The human model considered in our studies is the Duke model (34 years old man) from the ViP models by the IT'IS Foundation built with the IT'IS tissue database [28]. This model can be moved into different postures using the available poser tool from the Sim4Life software developed by Zurich MedTech. Some other notable voxel-based anatomical model are the Virtual Human Project [29] and the Japanese human models by the National Institute of Information and Communications Technology (NICT) [30].

2.3 Development of sensitivity analysis

As already developed earlier, uncertainty analysis and especially sensitivity analysis (SA) are essential when analyzing the dependency of the outputs of a given model or system. Such analysis can help to solve optimisation problems, perform model simplification, develop mitigation solutions... But to do so, if the considered system is a numerical model, some classical SA needs to compute a lot of time the provided model which leads to heavy computation time. A brief review of some classical SA methods is detailed here. Then, some of the existing solutions to reduce the heavy computation time in this case will be presented.

2.3.1 Classical sensitivity analysis computations

Historically, SA have been used only as local methods to study the uncertainty of an output given local variations of its inputs. These local methods were only relying on computing the partial derivatives of the output around a given value. Thanks to the development of adjoint-based methods, the cases of high-dimension input space have been successfully treated such as non-linear programming in 1976 [31] or hydrologic modeling in [32].

As opposed to these "local sensitivity analysis", with the rapid growth of numerical technologies during the 90s, some "global sensitivity analysis", which took into account the complete variation ranges of the inputs, started to be developed. These more powerful SA started to be used widely for industrial applications [33], for example in [34] for performance assessment of radioactive waste disposal.

Nowadays, various global SA methods are available depending on the possible objectives of the study (see section 2.1.1). This may include Monte Carlo techniques, statistical learning methods, graphical tools ect. Some more detailed reviews of existing techniques have been developed (Kleijnen [35], Christopher Frey and Patil [36] and Iooss and Lemaître [37]).

2.3.2 Global sensitivity analysis for complex models

For our electromagnetic problems, we are mainly focusing on global variations of the model inputs. Thus, some global SA methods for complex models will be presented with their various advantages and disadvantages regarding the complexity of the model (non-linearities, high-dimensions...). This methods can be separated in two categories: qualitative methods mainly used for factor prioritization and/or model simplification not relying on observables, unlike quantitative SA methods using measures (most are variance-based methods) to quantify the dependency of inputs regarding one another.

Qualitative methods

Mostly used on models with many input dimensions, or prior to a quantitative SA, qualitative SA aims at reducing the number of inputs by evaluating only a few times the input model (usually by an order equals to the input dimension). This techniques are called "screening methods" in which the input space is explored randomly and some sensitivity indices are computed for each input in order to classify them by order of importance. Most of this methods are using "One At a Time" (OAT) processes, where one input is explored while the others are fixed at some defined values.

For example, the Morris method [6] classifies the inputs into three categories: inputs with negligible effects on the output, inputs with significant and linear effects on the output, inputs with significant but non linear effects on the output. By computing the elementary effects of each OAT computations (rate of change along one input), two indices can be obtained for each input i : μ_i the estimated mean measuring the direct influence of the input i on the output and σ_i the standard deviation accounting for the non-linearity of the output response to a small variation of input i .

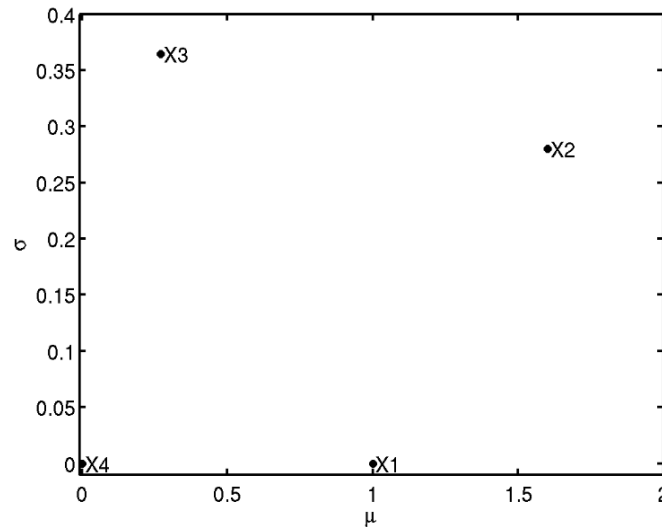


Fig. 2.5 Example of the Morris method on the analytical function $f(X) = x_1 + x_2^2 + x_2 \sin(x_3) + 0.x_4$ taken from <https://mogp-emulator.readthedocs.io/en/latest/methods/exam/ExamScreeningMorris.html> using four levels of a given OAT design (20 total samples)

A comprehensive example for the analytical function $f(X) = x_1 + x_2^2 + x_2 \sin(x_3) + 0.x_4$ is displayed on figure 2.5. While x_4 has obviously no effect on the output ($\mu_4 = \sigma_4 = 0$), the other three parameters have non-negligible values for μ and thus non-negligible effects on the output. x_1 has a linear effect on the output as $\sigma_1 \ll \mu_1$ while x_2 and x_3 have non-linear effects. After this qualitative analysis, the non-important parameters can be fixed at their nominal values and a quantitative SA can be performed on the remaining parameters to properly assess their influence on the output model.

Quantitative methods

Using a prior qualitative analysis, many different quantitative indices exist to measure the influence of a given input or several inputs at once on the output model. A common analysis is to fit the output to a linear model using three importance measures [38], the Pearson correlation coefficient measuring the linearity of the system against all inputs at once ρ , the Standard Regression Coefficient (SRC) representing the share of each input in the total output variance (providing the linearity hypothesis is confirmed)

and the Partial Correlation Coefficient (PCC) quantifying the sensitivity of the output against each input separately. The linearity of the system is assessed using the classical coefficient of determination R^2 (fit to a linear model) and the predictivity coefficient Q^2 measuring the percentage of the total variance due to the linear part of the model. If the linear-dependency of the output is refuted, one can perform a rank-transformation on the the input sample [39], and similar importance indices are defined: the Spearman correlation coefficient ρ^S , the Standardized Rank Regression Coefficient (SRRC) and the Partial Rank Correlation Coefficient (PRCC). Similarly, the monotony of the system has to be assessed by determination coefficient of the ranks (R_*^2) and the predictivity coefficient of the ranks (Q_*^2).

The most common sensitivity trackers are the Sobol' indices [40], which will be developed later (see section 3.1.5) as they are the ones we mainly used to quantify the sensitivity of our systems based on the output variance. The FAST method (first detailed by Cukier, Schaibly, and Shuler in 1975 [41]), also variance-based, aims at reducing the computation cost by a multi-dimensional Fourier transform of the output. Unfortunately, the computation cost is only low for the first-order sensitivity indices but spikes quickly for higher interaction orders.

But the dependency of the output variance cannot sometimes account for the total behavior of the system. Thus, other importance measures, which are variance independent, also exists. In [42], Auder and Iooss define sensitivity indices based on Shannon's entropy [43] and also on Kullback–Leibler entropy [44] that can provide additional information on the sensitivity of the model output (on the top of a classical Sobol' analysis). Another method is the use of distribution based-sensitivity indices [45], which compare the output distribution with the conditional output distribution regarding one or several inputs.

Discussion

For most computational models, only a handle of all the considered inputs are influentials. Therefore, the model is first simplified before going deeper

into its SA analysis. But doing so using screening techniques for example, might lead to a higher computation cost (for a model with a lot of input variables) due to this pre-analysis step.

As for Sobol' SA and other importance measures, the number of model evaluations is also high. For Sobol' analysis, as the input samples are usually generated by Monte Carlo sequences, even if some improvement have been made, like using quasi-Monte Carlo sequences [46], the complexity remains huge and the total computation cost is extremely high, which makes it almost impossible to use for complex simulation models.

A possible solution could be to have more information than just a simple quantitative information on the output but rather an estimation of its value using a predictor at a low-computation cost. Various methods have been used to approximate output models, with the most commons being the smoothing methods that can be used afterwards to perform various variance-based global SA: local polynomial interpolators, moving averages, smoothing splines ect. (see a detailed review in [47]). This surrogate model along with its building process is called a "metamodel".

2.4 A possible solution: metamodeling

An example, taken from [37], displayed on table 2.1, shows the main interest of using metamodels for sensitivity analysis: in the case of a flood model, a Kriging metamodel has been built with $n'_{samples} = 100$ model evaluations and then used as a predictor for the computation of Sobol' indices. The same Sobol' analysis has been performed on the direct model and needed $n_{samples} = 7.10^7$ model evaluations. It can be seen that for all five input parameters, the metamodel is able to quantify similarly the first-order and total effects of each input on the flood model (relative errors $< 15\%$). But to do so, such metamodel required 700000 times less input samples than the regular model.

Table 2.1 Comparison of the Sobol' indices estimated by Monte Carlo sampling of a real flood model ($n_{samples} = 7.10^7$ model evaluations) with the same SA performed on a Kriging metamodel built with $n'_{samples} = 100$ model evaluations, taken from [37]

parameters	x_1	x_2	x_3	x_4	x_5
S_i model	0.355	0.159	0.183	0.125	0.380
S_i metamodel	0.389	0.168	0.188	0.139	0.370
S_i^T model	0.482	0.253	0.229	0.181	0.380
S_i^T metamodel	0.455	0.210	0.213	0.168	0.430

Hence why, the development of surrogate models has been intensified recently. Given a certain number of samples, the resulting predictor can be used in lieu and place of the existing simulation model (or experimental model). This metamodel is an analytical function which can be computed fastly a great number of times. Thus, the global SA, like Sobol' indices computed with Monte-Carlo methods, is performed on the predictor at a low computation cost easily. This enables fast and easy computation of global sensitivity indices on the complex output model, providing an accurate metamodel has been built.

2.4.1 Surrogate models

The goal of a metamodelling process is to build a "black box" analytical function that can be used in a lieu and place of the expensive computational model to compute an output for any input within the considered training distribution. The basic principles of building a metamodel are summarized on figure 2.6 with the case of a 2D input and a 1D output. Approximating a computational model $\mathcal{M}(\mathbf{X})$ using a metamodelling process consists in three steps:

- An experimental design consisting of n different samples is chosen within the parameter space: $\mathbf{X} = (\mathbf{X}_1, \dots, \mathbf{X}_n)$.
- Then, their corresponding responses are computed using the simulation model $\mathbf{Y} = (\mathbf{Y}_1, \dots, \mathbf{Y}_n)$.

- Finally, a surrogate model $\widehat{\mathcal{M}}$ is trained on the input dataset $\{\mathbf{X}, \mathbf{Y}\}$ with its different parameters (called meta-parameters) optimized for minimizing a defined validation criteria (for example the mean square error)

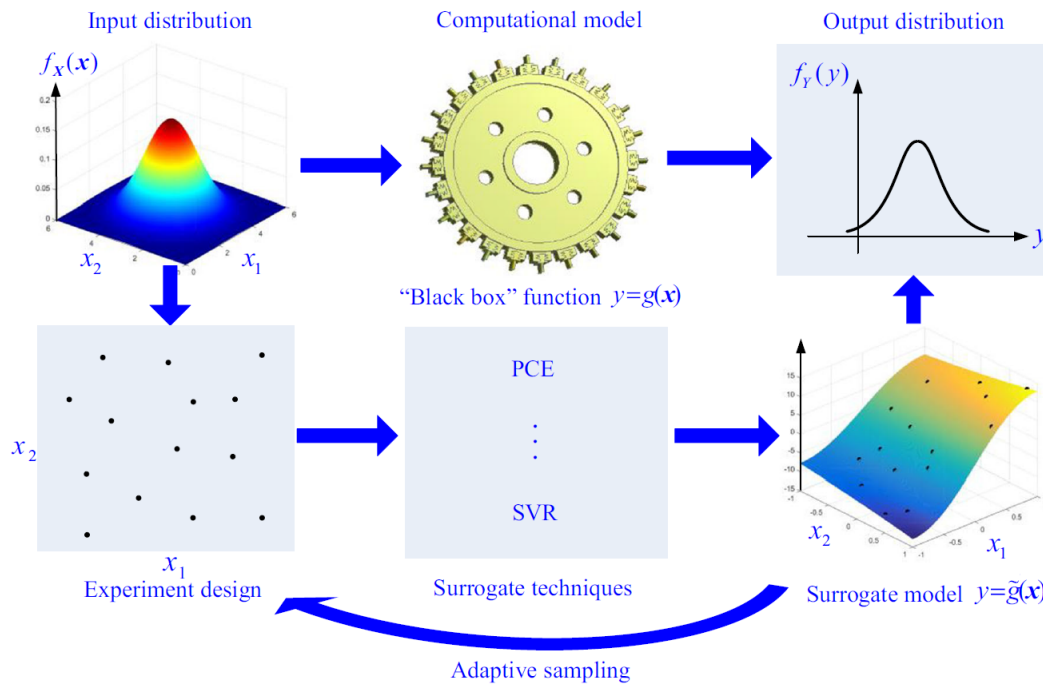


Fig. 2.6 Basic principles of a metamodeling process, Cheng et al. [48]

The resulting metamodel $\widehat{\mathcal{M}}$ can be used for performing sensitivity analysis, uncertainty quantification or optimizations fastly within the input distribution. As, the main goal of this processes are to save computation time, it is crucial to select a triplet (sampling strategy, metamodeling technique, validation metric) fitted to the considered problem. A summary of the common techniques for metamodeling processes is displayed on table 2.2.

Various sampling strategies have been historically develop and are widely used for metamodeling processes. Most of them are "static" sampling strategies which consists in fixing the sample size prior to the meta-model computation. The classic methods include regular grids to stochastic samplings such as Monte-Carlo based samplings but also space filling-methods such as Latin hypercube sampling [49] or orthogonal arrays [50].

Most of the time, such static sampling techniques can lead to under or over-sampling issues and need some calibration time. Hence why, a common way to decrease the number of calls of the computational model is to develop active learning strategies. The base principle is to compute more points in the neediest areas of the input space and build a metamodel sequentially, computing more points at every step if needed. But, these adaptive sampling strategies could also lead to smaller sample sizes and a huge number of computed datapoints in the end if wrongly calibrated. This will be discussed more thoroughly in chapter 4.

In order to perform an accurate global SA, the reliability of the metamodel predictor needs to be properly assessed. For global consistency most methods are historically based on the mean square error or the fitting coefficient of determination R^2 . While the local consistency was mostly measured with the relative maximum absolute error. These methods are all considering the metamodel on the whole input dataset without any additional computations. But for metamodels, cross-validation methods (CV) have been found extremely useful for estimating the consistency of the predictors [51]. For example with an input dataset of n datapoints, Leave-p-out CV consists of using p samples for the validation of the metamodel and the remaining $n - p$ for the training set. This is repeated until all possible $\binom{n}{p}$ samples have been chosen and the resulting estimation error is usually an average of the mean square error. Thus, CV insures a better global consistency while also being a potential validation metric for adaptive sampling strategy earlier discussed. For small sample sizes, the special cases at $p = 1$ (LOO) and $p = 2$ of the Leave-p-out CV error are usually taken as consistency tracker. But for bigger samples, the k-fold CV is preferred where k subsets are randomly generated from the input dataset and used both as training and validation set [52].

Table 2.2 Commonly used metamodeling processes: sampling methods, surrogate techniques and fitting criteria (based on an early review in 2006 by Wang and Shan [53])

Sampling techniques	Surrogate model	Validation metric
<p>Classic methods:</p> <ul style="list-style-type: none"> • Fractional • Central composite • Box-Behnken • I_order, K_order, D_order... • Plackett-Burman • Monte-Carlo Sampling (MCS) <p>Space - filling methods:</p> <ul style="list-style-type: none"> • Latin Hypercube • Orthogonal Array • Hammersley sequence • Uniform design <p>Hybrid methods</p> <p>Random selection</p> <p>Handpicked</p> <p>Importance sampling</p> <p>Adaptative sampling</p>	<ul style="list-style-type: none"> • Polynomial (polynomial regression model, PCE...) • Radial Basis Functions (RBF) • Gaussian Process (Kriging) • Artificial Neural Network (ANN) • Low-rank tensor approximation (LRA) • Support-vector regression (SVR) • High-dimensional model representation (HDMR) • Hybrid methods (PCK, polynomial response surface...) 	<p>Global:</p> <ul style="list-style-type: none"> • Relative root mean square error • Relative average absolute error • Coefficient of determination R^2 • Mean square error <p>Local:</p> <ul style="list-style-type: none"> • Relative maximum absolute error • Mean absolute error <p>Cross-Validation (CV):</p> <ul style="list-style-type: none"> • Leave-p-out Error (LpO, LOO...) • k-fold CV

2.4.2 Metamodelling for sensitivity analysis

Most of the metamodelling processes can be split into two groups: the ones based on polynomials (Response Surface Methodology (RSM), PCE, ANOVA-HDMR, PCK...) and the others based on other types of functions, usually Gaussian functions (Kriging, SVR, RBF, LRA...). In this section, various

surrogate techniques will be discussed with a focus on computations of global SA.

Response Surface Methodology

One of the polynomial-based surrogate model is the Response Surface Methodology (RSM), which is a simple polynomial regression model and thus one of the earliest developed for global SA (Bucher and Bourgund in [54]). Usually a second-order polynomial approximation is used and the SA indices can be computed directly from the unknown coefficients. For an unidimensional output, the metamodel is formulated as:

$$\widehat{\mathcal{M}}(\mathbf{x}) = \alpha_0 + \sum_{i=1}^n \alpha_i x_i + \sum_{i=1}^n \alpha_{ii} x_i^2 + \sum_{(i,j), i < j}^n \alpha_{ij} x_i x_j \quad (2.1)$$

with α_0 , α_i , α_{ii} and α_{ij} being the $\frac{(n+1)(n+2)}{2}$ unknown coefficients. Even if the RSM is easily applicable for simple models at low dimensions, the accuracy of the resulting predictor is usually bad for non-linear problems and the curse of dimensionality appears for high-dimensional input space as the number of unknowns blows up.

High-dimensional model representation

High-dimensional model representation (HDMR) has been developed particularly to tackle the non-linearity of the input models by improving the accuracy of the predictor regarding a simple RSM. Its general formulation consists of independent functions representing the output response to different interaction orders of the input:

$$\widehat{\mathcal{M}}(\mathbf{x}) = \mathcal{M}_0 + \sum_{i=1}^n \mathcal{M}_i(x_i) + \sum_{(i,j), i < j}^n \mathcal{M}_{ij}(x_i, x_j) + \dots + \mathcal{M}_{1,2,\dots,n}(x_1, x_2, \dots, x_n) \quad (2.2)$$

where \mathcal{M}_0 , \mathcal{M}_i , \mathcal{M}_{ij} ... are functions representing the finite expansion of the input model \mathcal{M} among all interaction order for the input parameters. The high-order interactions have been proven numerically negligible [55] and if

the sum in equation 2.2 is truncated to the second-order for example, the number of summands is $1 + n + \frac{n(n-1)}{2}$ which is slightly less than in RSM (equation 2.1). The common HDMR techniques are the Cut-HDMR and the ANOVA-HDMR [56]. The Cut-HDMR is based on lines/hyperplanes passing through defined cut points. Although such interaction functions realize an exact interpolation of the input model, the Cut-HDMR is highly sensitive to the choice of the cut points and thus, could lead to long computations if the convergence of the meta-parameters optimization is slow. The ANOVA-HDMR is assuming its decomposition (equation 2.2) is similar to the Sobol' decomposition (see equation 3.21) but using an orthonormal polynomial basis for the interaction functions (as the PCE). The global SA indices can be derived directly from the metamodel decomposition for both Cut-HDMR and ANOVA-HDMR techniques. Although this methods do not tackle the curse of dimensionality, they have been proven quite useful for approximating high-dimensional models for global SA [57].

Support-vector regression

Support-vector regression (SVR) has been only recently developed in the spark of research for machine learning [58]. The data is projected onto a high-dimensional feature space using a kernel prediction function, this brings the global optimisation problem to a convex problem, where the uniqueness of a solution is assured. Various kernel functions are possibles (Polynomial, Gaussian, Fourier...), with the Gaussian kernel function being the most common: the SA indices can be again computed directly from the decomposition. But SVR has only been used in the last few years to perform sensitivity analysis [59]. For unknown trend responses and especially for non-linear problems, SVR is providing an excellent trade-off solution. But it remains extremely sensitive to the selection of the projection function (the meta-parameters) is not to be favored if the global behaviour of the model is well known.

Radial basis functions

Radial basis function regression (RBF) has been early developed in 1971 for fitting topographical data [60]. With an input dataset $\mathbf{X} = (\mathbf{x}_1, \dots, \mathbf{x}_N)$ of N samples, the standard RBF model is formulated as:

$$\widehat{\mathcal{M}}(\mathbf{x}) = \sum_{i=1}^N w_i \varphi(\|\mathbf{x} - \mathbf{x}_i\|) \quad (2.3)$$

For each sampled datapoint \mathbf{x}_i , an RBF φ is paired with a weighted coefficient w_i . The RBF value is only depending on the distance between the considered input point \mathbf{x} and the sampled datapoints \mathbf{x}_i . The RBF φ is usually a gaussian function with a given bandwidth, this reduces the number of meta-parameters to $2N$ only. Although it is widely used for solving partial differential equations or computing easily surface integrals, RBF has also been used for global SA (see [61] for its application on a train design optimization). Unfortunately, RBF is highly sensitive to the choice of the input dataset, and without a proper pre-processing, the resulting predictor would be highly inaccurate.

Gaussian process (Kriging)

Initially developed for geostatistics, gaussian process or the Kriging model named after Krige [62], is an interpolation process assuming the output is the realization of a zero-mean gaussian process (for local variations) with a given unknown trend (global tendency of the model):

$$\widehat{\mathcal{M}}(\mathbf{x}) = \beta^T f(\mathbf{x}) + \sigma^2 Z(\mathbf{x}, \omega) \quad (2.4)$$

where $\beta^T f(\mathbf{x})$, is the mean value of the Gaussian process which consists in the regression coefficients $(\beta_0, \dots, \beta_P)$ and the corresponding P basis functions (f_0, \dots, f_P) , and σ^2 , the variance of the stationary Gaussian process $Z(\mathbf{x}, \omega)$. Kriging in its ordinary form (constant trend) performs an exact interpolation of the input model [63]. Many forms of Kriging have already been used for global SA (see [64] for example) and the SA indices can be derived from the regression coefficients. Kriging has already been used

successfully at the GeePs as an interpolator of a complex scintillation model [65]. Although quite easy to setup and accurate at approximating non-linear models, such metamodel is not suited for noisy data where additional trend computations need to be performed thus decreasing its efficiency.

Polynomial Chaos Expansion

Among polynomial-based surrogate techniques, Polynomial Chaos Expansion (PCE), initially proposed by Wiener in 1938 [66], is one of the most common method for approximating complex models. The model is projected onto an orthonormal polynomial basis and its expression can be formulated as:

$$\widehat{\mathcal{M}}(\mathbf{x}) = \sum_{\alpha \in \mathcal{A}} y_{\alpha} \psi_{\alpha}(\mathbf{x}) \quad (2.5)$$

with the y_{α} being the coefficients of the finite decomposition on the polynomial basis $\{\psi_{\alpha}, \alpha \in \mathcal{A}\}$. Recently, the method has been enhanced and proven reliable for tackling the curse of dimensionality problem in the case of SA for complex problems [67]. Moreover, the global SA indices can be obtained by a direct post-processing of the PCE coefficients. This surrogate can be combined with Kriging in order to gain most benefits of the two metamodels. This produces a Polynomial Chaos Kriging (PCK) metamodel: a Kriging metamodel with a specific PCE trend [68].

2.4.3 Metamodels for computational electromagnetics

As described before, metamodels have been proven extremely useful for global SA of complex models thanks to their flexibility: easy to implement, great efficiency with stochastic models, high accuracy for high-order interaction and non-linearities. Moreover, the resulting predictor can be used for additional information on the model behavior but also to perform other analysis (like the solving of an optimisation problem) on the parameter space. Thus, metamodeling processes have been chosen as our tool for performing global SA on complex models.

Regarding electromagnetic problems in general, two surrogate models (PCE and Kriging) along with their combination (PCK) have been proven quite efficient for building accurate predictors and performing various global SA on a wide range of complex models. For example in the case of electromagnetic device optimization [69], Kriging has been compared to RBFs and RSM in term of the accuracy of the resulting predictor and provided better results while being easier to implement. Approximating magnetic flux densities from measurement data in the case of a WPT system has been achieved in [70] with RBFs and stacking of azimuthal planes. PCE has been proven successful at approximating magnetic flux density at a lower computation cost than regular simulations [71]. As for PCK metamodelling, it has been recently used for example in the case of computational dosimetry for estimating SAR values [72]. Hence why the research is currently spiking on this topic in the field of electromagnetic computation ([73],[74],[75]).

Due to their versatility, their robustness against non-linearities, their easy implementation and the great number of available libraries and documentations on their use, PCE, Kriging and PCK are the metamodelling processes on which we will be focusing. The metamodels described in this work will be computed using the open source UQLab framework available on MATLAB and developed at the Chair of Risk, Safety and Uncertainty Quantification of ETH Zurich [76]. All of these surrogate techniques and their application to simple cases will be discussed in details in the next chapter.

Chapter 3

Metamodelling for electromagnetic systems

As already described in the literature (see chapter 2), the use of surrogate metamodels has been proven quite useful for predicting computational values and thus performing various operations at a low computation cost. This chapter develops here the functioning and use of different metamodelling processes: Kriging, Polynomial Chaos expansion and PCK (a combination of both), in terms of consistency and Sobol-based sensitivity analysis. An analysis on a simple WPT system COMSOL model has been conducted and the results have been extended to a more complex full car model where the need of saving computation time is greater.

3.1 Surrogate models

Let's consider an electromagnetic quantity, expressed by a vector \mathbf{y} , either unidimensional or multi-dimensional. For example, it can be a scalar like the coupling factor of a WPT system k (see section 4.4.3) or even a bigger vector of 100 B-field values along a vertical line which embodies a human standing position (see section 3.3.1). These vectors are computed by FEM or FDTD models with COMSOL, OPERA or Sim4Life but can also be taken from experimental results (see section 5.3). The goal of using surrogate models

is to estimate the influence of various parameters on this electromagnetic quantity \mathbf{y} at a low computation cost.

Let d be the number of studied parameters the electromagnetic system is depending on, the parameters are named (P_1, \dots, P_d) . Each parameter P_i is studied along a given interval of variation $\mathcal{X}_i \subset \mathbb{R}$. An input $\mathbf{x} = (x_1, \dots, x_d)$ is a valid set of parameter values such that $\forall i \in \llbracket 1, d \rrbracket, x_i \in \mathcal{X}_i$. It can be expressed as $\mathbf{x} \in \mathcal{X}$, where $\mathcal{X} = \bigotimes_{i=1}^d \mathcal{X}_i \subset \mathbb{R}^d$ is the input parameter space. Seemingly the vector \mathbf{y} is named output and is considered within a certain output space, $\mathbf{y} \in \mathcal{Y}$.

For a given input \mathbf{x} , the input model \mathcal{M} (experimental or computational) used to compute the vector \mathbf{y} is considered as the realisation of a function such that $\mathbf{y} = \mathcal{M}(\mathbf{x})$. A couple (\mathbf{x}, \mathbf{y}) is named input datapoint or input sample. A set $\{(\mathbf{x}_1, \mathbf{y}_1), \dots, (\mathbf{x}_n, \mathbf{y}_n)\}$ of n various input parameters and their corresponding outputs is named input dataset or experimental design.

This input dataset can be used to compute a surrogate model $\widehat{\mathcal{M}}$ such that $\forall (\mathbf{x}, \mathbf{y}) \in \mathcal{X} \otimes \mathcal{Y}, \mathbf{y} = \mathcal{M}(\mathbf{x}) \approx \widehat{\mathcal{M}}(\mathbf{x})$. The resulting surrogate model $\widehat{\mathcal{M}}$ is an available predictor for the input model \mathcal{M} . As it is an analytical function, this predictor can be used instead of the real model to compute many datapoints at a low computation cost and perform various operations such as sensitivity analysis or solve optimisation problems.

3.1.1 Kriging: a Gaussian process

Kriging (a.k.a. Gaussian process modelling) is a stochastic interpolation algorithm which assumes that the model output $\mathcal{M}(\mathbf{x})$ is a realization of a Gaussian process with $\mathbf{x} \in \mathcal{X} \subset \mathbb{R}^d$. A Kriging metamodel is described by the following equation [77]:

$$\widehat{\mathcal{M}}(\mathbf{x}) = \boldsymbol{\beta}^T \mathbf{f}(\mathbf{x}) + \sigma^2 Z(\mathbf{x}, \omega) \quad (3.1)$$

The first term in equation 3.1, $\boldsymbol{\beta}^T \mathbf{f}(\mathbf{x})$, is the mean value of the Gaussian process (a.k.a. trend) and it consists of the regression coefficients $(\beta_0, \dots, \beta_P)$ and the corresponding P basis functions (f_0, \dots, f_P) . The second term in

equation 3.1 consists of σ^2 , the (constant) variance of the Gaussian process and $Z(\mathbf{x}, \omega)$, a zero mean, unit variance, stationary Gaussian process. The underlying probability space is represented by ω and is defined in terms of a correlation function R (a.k.a. correlation family) and its hyperparameters θ . The correlation function $R(\mathbf{x}, \mathbf{x}', \theta)$ describes the correlation between two samples of the input space.

Before computing the unknown parameters of the kriging metamodel, the following needs to be define:

- the basis functions (f_0, \dots, f_P) that defines the trend type are needed
- a correlation function $R = R(\mathbf{x}, \mathbf{x}', \theta)$ is needed

Using the available training dataset, the hyperparameters θ can be computed through an optimization process. With such hyperparameters, the remaining kriging parameters can be obtained: the trend regression coefficients $(\beta_0, \dots, \beta_P)$ and the variance of the gaussian process. An example of interpolation by kriging can be seen on figure 3.1.

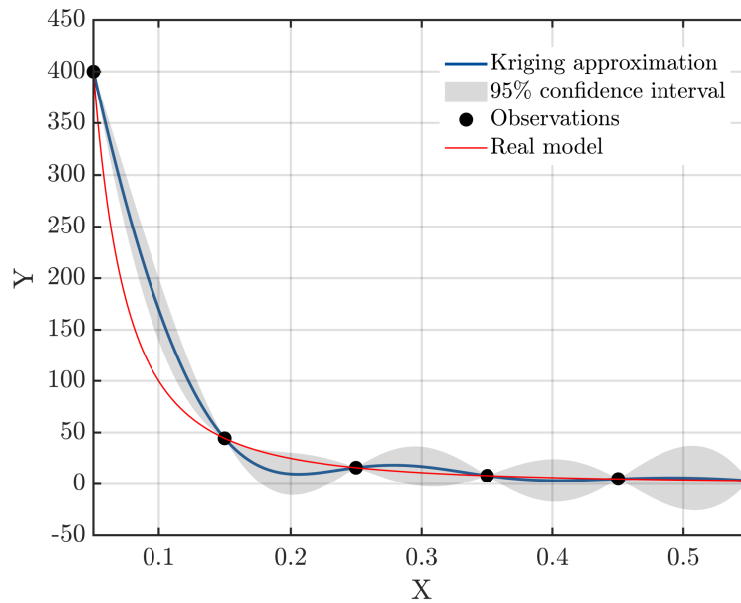


Fig. 3.1 Example of a kriging metamodel for predicting the function $f: x \rightarrow \frac{1}{x^2}$

Trend types

Various functions can be chosen for the basis functions (f_0, \dots, f_P) , thus defining various types for the kriging process [78]:

- The trend for **Universal Kriging** can be defined as:

$$\beta^T f(\mathbf{x}) = \sum_{i=1}^P \beta_i f_i(\mathbf{x}) \quad (3.2)$$

Apart from this general form of kriging, two specific types of kriging can also be defined.

- **Ordinary Kriging** has an unknown but constant trend:

$$\beta^T f(\mathbf{x}) = \beta_1 \quad (3.3)$$

- The trend for **Simple Kriging** is a known linear combination of user-defined functions:

$$\beta^T f(\mathbf{x}) = \sum_{i=1}^P f_i(\mathbf{x}) \quad (3.4)$$

The basis functions (f_0, \dots, f_P) are totally arbitrary and user-defined. Most of the time, the basis is composed of linear combination of polynomials and constants. The values of the regression coefficients $(\beta_0, \dots, \beta_P)$ are computed using the hyperparameters values θ found by the optimization process. The computation is fairly easy to perform for **Ordinary Kriging** as only one value needs to be computed (see equation 3.3) and for **Simple Kriging** none is needed as $(\beta_0 = \beta_1 \dots = \beta_P = 1)$ (see equation 3.4). The most commonly used trends are summarized in table 3.1.

Table 3.1 Commonly used trends

Trend	Formula	Number of unknowns
constant	β_0	1
linear	$\beta_0 + \sum_{i=1}^d \beta_i x_i$	$d + 1$
quadratic	$\beta_0 + \sum_{i=1}^d \beta_i x_i + \sum_{i=1}^d \sum_{j=1}^d \beta_{ij} x_i x_j$	$d^2 + d + 1$

Correlation function types

Assuming \mathcal{X} the input parameter space, the correlation function (or kernel) $R(x, x')$ for two inputs $(x, x') \in \mathcal{X} \times \mathcal{X}$ reflects the effect of the distance between the two input points on the distance of the corresponding outputs. It describes if (x, x') are close within the input space \mathcal{X} , how close their corresponding inputs (y, y') are in the output space \mathcal{Y} .

Let $(x, x') \in \mathbb{R}^2$ be two one-dimensional inputs, a tunable scale parameter $\theta \in \mathbb{R}_+^*$ can be defined for the correlation function $R(x, x', \theta)$. As for the various available trends, various correlation families can be chosen:

- **Linear** correlation:

$$R(x, x', \theta) = \max \left(0, 1 - \frac{|x - x'|}{\theta} \right) \quad (3.5)$$

- **Exponential** correlation:

$$R(x, x', \theta) = \exp \left(-\frac{|x - x'|}{\theta} \right) \quad (3.6)$$

- **Gaussian** correlation:

$$R(x, x', \theta) = \exp \left[-\frac{1}{2} \left(\frac{|x - x'|}{\theta} \right)^2 \right] \quad (3.7)$$

- **Matérn-3/2** and **Matérn-5/2** correlations [79]:

$$R(x, x', \theta, v = 3/2) = \left(1 + \sqrt{3} \frac{|x - x'|}{\theta}\right) \exp\left(-\sqrt{3} \frac{|x - x'|}{\theta}\right) \quad (3.8)$$

$$R(x, x', \theta, v = 5/2) = \left[1 + \sqrt{5} \frac{|x - x'|}{\theta} + \frac{5}{3} \left(\frac{|x - x'|}{\theta}\right)^2\right] \exp\left(-\sqrt{5} \frac{|x - x'|}{\theta}\right) \quad (3.9)$$

For multidimensional inputs $(\mathbf{x}, \mathbf{x}') \in (\mathcal{X} \times \mathcal{X}) \subset (\mathbb{R}^d \times \mathbb{R}^d)$, the one-dimensional correlation families can be extended using a one **ellipsoidal** variable:

$$R(\mathbf{x}, \mathbf{x}', \boldsymbol{\theta}) = R(h), h = \left[\sum_{i=1}^d \left(\frac{x_i - x'_i}{\theta_i}\right)^2\right]^{\frac{1}{2}} \quad (3.10)$$

For an isotropic correlation family ($\forall i \in \llbracket 1, d \rrbracket, \theta_i = \theta$), the kernel is simply a one dimensional kernel with the norm as input:

$$R(\mathbf{x}, \mathbf{x}', \theta) = R(h), h = \frac{1}{\theta} \left[\sum_{i=1}^d (x_i - x'_i)^2\right]^{\frac{1}{2}} = \frac{\|\mathbf{x} - \mathbf{x}'\|}{\theta} \quad (3.11)$$

3.1.2 Polynomial Chaos expansion

The Polynomial chaos expansion (PCE) is another stochastic interpolation algorithm which assumes that the model output $\mathcal{M}(x)$ is a projection on an orthonormal polynomial basis [80]. The model can be interpolated as the following equation:

$$\mathcal{M}(\mathbf{x}) = \sum_{\alpha \in \mathbb{N}^d} y_{\alpha} \psi_{\alpha}(\mathbf{x}) \quad (3.12)$$

where the ψ_{α} are the orthonormal basis with the α being the multi-indices identifying the multidimensional inputs and the various polynomial degrees and y_{α} their corresponding coordinates on the basis. In practical applications, the projection needs to be truncated for a finite sum:

$$\mathcal{M}(\mathbf{x}) \approx \widehat{\mathcal{M}}(\mathbf{x}) = \sum_{\alpha \in \mathcal{A}} y_{\alpha} \psi_{\alpha}(\mathbf{x}) \quad (3.13)$$

where $\mathcal{A} \subset \mathbb{N}^d$ is a subset of the available multi-indices.

The results of a PCE metamodel are displayed in figure 3.2. A notable difference compared to Kriging is that PCE metamodelling is not an exact interpolator, indeed the predicted value is different from the observation. This can be useful to avoid huge peak values in the output model but might also be an issue as it could greatly diminish the predicting accuracy.

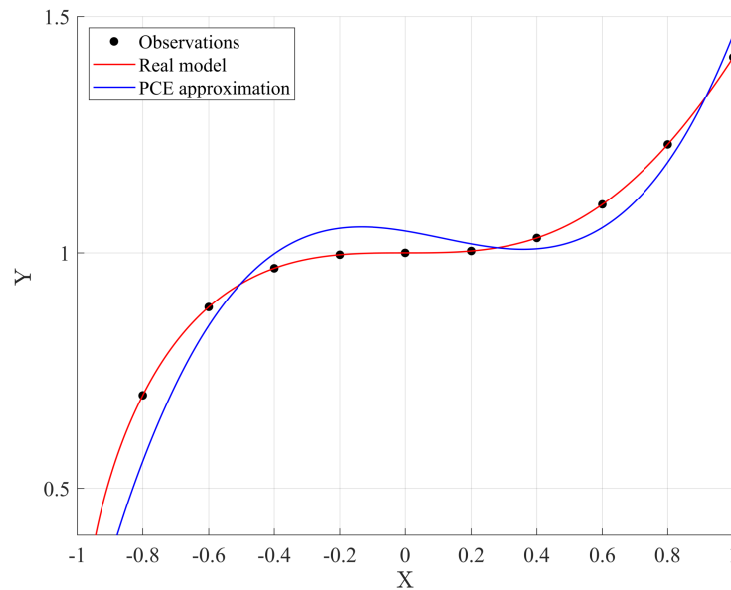


Fig. 3.2 Example of a PCE metamodel for predicting the function $f: x \rightarrow \sqrt{x^3 + 1}$

Polynomial basis

When designing a PCE interpolation, an adequate orthonormal polynomial basis ψ_α is needed. The classical polynomial families and their corresponding distribution are given in table 3.2.

Table 3.2 Classical univariate polynomial families [81]

Distribution	Orthogonal polynomials
Uniform	Legendre
Gaussian	Hermite
Gamma	Laguerre
Beta	Jacobi
Log-normal	Hermite

From these unidimensional polynomial families, a set of d -dimensional orthonormal polynomials can be built. In equations 3.13 and 3.12, the multivariate polynomial basis $\psi_\alpha(\mathbf{x})$ is usually built from the tensor product of d unidimensional orthonormal polynomials each corresponding to the various input parameters:

$$\psi_\alpha(\mathbf{x}) = \bigotimes_{i=1}^d \phi_{\alpha_i}^i(x_i) \quad (3.14)$$

where α_i is the polynomial degree for a given input variable i . The polynomial families for each input can be different depending on the type of marginal distribution. The set of unidimensional orthonormal polynomials verifies:

$$\langle \phi_j^i, \phi_k^i \rangle = \int_{\mathcal{D}_{X_i}} \phi_j^i(x_i) \phi_k^i(x_i) dx_i = \delta_{jk} \quad (3.15)$$

with j and k two polynomial degrees and δ_{jk} the Kronecker symbol. The orthonormality from equation 3.15 can be extended for two given sets of indices $(\alpha, \beta) \in \mathcal{A}^2$ using equation 3.14:

$$\langle \psi_\alpha, \psi_\beta \rangle = \delta_{\alpha\beta} \quad (3.16)$$

with $\delta_{\alpha\beta}$ the extension of Kronecker symbol for multi-dimensional cases.

3.1.3 Polynomial Chaos-Kriging metamodel

With these two interpolation techniques (Kriging and PCE), an exact interpolator can be built: Polynomial Chaos-Kriging (PCK) metamodelling combines both PCE and Kriging to predict the variations of $\mathcal{M}(\mathbf{x})$ in a single metamodel. Kriging is used to interpolate the local variations of the output model while PCE is useful for the global approximation. A PCK metamodel is defined by [68], [82],[72]:

$$\widehat{\mathcal{M}}(\mathbf{x}) = \sum_{\alpha \in \mathcal{A}} y_{\alpha} \psi_{\alpha}(\mathbf{x}) + \sigma^2 Z(\mathbf{x}, \omega) \quad (3.17)$$

where $\sum_{\alpha \in \mathcal{A}} y_{\alpha} \psi_{\alpha}(\mathbf{x})$ is a weighted sum of orthonormal polynomials describing the trend of the PCK model, σ^2 and $Z(\mathbf{x}, \omega)$ denote the variance and the zero mean, unit variance, stationary Gaussian process, respectively. When looking at equation 3.1 PCK can be interpreted as a Kriging metamodel with a polynomial trend, whose characteristics are unknown. Therefore the PCK metamodel is built in two parts: the computation of the polynomial coefficients (y_{α}) on one side and the kriging hyperparameters (θ, σ^2) on the other side.

3.1.4 A posteriori error estimation

Consistency of the metamodel

Let's consider a set $\{(\mathbf{x}_1, \mathbf{y}_1), \dots, (\mathbf{x}_n, \mathbf{y}_n)\}$ of n various input parameters and their corresponding outputs. Using this set, one can build a metamodel $\widehat{\mathcal{M}}$ using either Kriging, PCE or PCK. The consistency of the metamodel is calculated using the mean LOO (Leave-One-Out error):

$$LOO = \frac{1}{n} \sum_{i=1}^n \left(\frac{\|\widehat{\mathcal{M}}_{/i}(\mathbf{x}_i) - \mathbf{y}_i\|}{\|\mathbf{y}_i\|} \right)^2 \quad (3.18)$$

where $\widehat{\mathcal{M}}_{/i}$ is the mean predictor that was trained using all (\mathbf{x}, \mathbf{y}) but $(\mathbf{x}_i, \mathbf{y}_i)$. The LOO enables us to evaluate the consistency of the metamodel consider-

ing its build. If the LOO is close to 1, the metamodel is highly modified if one datapoint is erased, whereas the smallest it is, the least it will be modified.

Throughout this work, the quality of the metamodels will be described using the consistency provided by the LOO. As already detailed in chapter 2, many other metrics can be used such as the k-fold or RMSE. But given the dimensionality and the size of the training datasets used for the systems considered here, the LOO represents a good compromise as it is extremely fast to compute for a low number of input samples ($n < 50$) while being an excellent quality tracker for low dimensionalities ($d < 10$) [83]. Moreover it does not require additional calls of the input model. Although, for higher dimensionalities and bigger number of samples, the aforementioned assumptions on the LOO could not be verified and the developments made here would require a proper analysis and a new definition of an adapted quality tracker.

Accuracy of the metamodel

In order to measure the accuracy of the output model with fewer points than the available experimental design, an estimate of the accuracy can be defined, the OSE (Out-Of-Sample error):

$$OSE = \frac{1}{n-k} \sum_{i=1}^{n-k} \left(\frac{\|\widehat{\mathcal{M}}_k(\mathbf{x}_i) - \mathbf{y}_i\|}{\|\mathbf{y}_i\|} \right)^2 \quad (3.19)$$

where $\widehat{\mathcal{M}}_k$ is the predictor of the metamodel that was trained using k datapoints among the n available. The analysis of the OSE emphasizes something different than the LOO analysis does: if the OSE for k datapoints is extremely small, it means that at the non-training points there is almost no difference between the predictor and the real value. Hence, if the OSE for k datapoints is small, there was no need to compute n datapoints for this given experimental design but k could have been enough.

Validation error

Once a metamodel $\widehat{\mathcal{M}}$ has been computed with a given input dataset. A validation set $\{(\mathbf{x}_i, \mathbf{y}_i = \mathcal{M}(\mathbf{x}_i)), \forall i \in \llbracket 1, n \rrbracket\}$ can be used to compute a validation error for the metamodel with the well-known coefficient of determination R^2 :

$$R^2 = 1 - \frac{\sum_{i=1}^n \|\widehat{\mathcal{M}}(\mathbf{x}_i) - \mathbf{y}_i\|^2}{\sum_{i=1}^n \|\bar{\mathbf{y}} - \mathbf{y}_i\|^2} \quad (3.20)$$

where $\bar{\mathbf{y}}$ is the mean value of the validation set output. The closest R^2 is to one, the better the predictor is at computing non-sampled datapoints. This coefficient is useful for comparing different metamodels on the same validation set, in order to determine which one gives us the best predictor.

3.1.5 Sobol' indices

For these various metamodelling processes and our input models, the well-know Sobol' indices (first introduced here [40]) have been chosen as our sensitivity trackers. The first order Sobol index for a parameter P is a simple quantity varying from 0 (almost independent) to 1 (the more dependent) quantifying the dependency of the output model on a given parameter P regarding a variation of several parameters simultaneously. When using PCE-based metamodels, the computation of the Sobol' indices of the surrogate model can be easily extracted from the polynomial decomposition (see section 3.1.6). The computation of both first order and total Sobol' indices (higher orders) is shortly developed here.

Sobol decomposition

Let us consider a model output $\mathbf{Y} = \mathcal{M}(\mathbf{X})$ with d input parameters (X_1, \dots, X_d) . The input parameter spaces are all considered transformed onto the unit hypercube with independent and uniform distribution such that a realization of \mathbf{X} is $\mathbf{x} \in [0, 1]^d$. According to the unique Sobol' decomposition [40], $\forall \mathbf{x} = (x_1, \dots, x_d) \in [0, 1]^d$, $\mathcal{M}(\mathbf{x})$ can be written as:

$$\begin{aligned}
\mathcal{M}(\mathbf{x}) &= \sum_{s=1}^d \sum_{i_1 < \dots < i_s}^d \mathcal{M}_{i_1 \dots i_s}(x_{i_1}, \dots, x_{i_s}) \\
\mathcal{M}(\mathbf{x}) &= \mathcal{M}_0 + \sum_{i=1}^d \mathcal{M}_i(x_i) + \sum_{(i,j), i < j}^d \mathcal{M}_{ij}(x_i, x_j) + \dots + \mathcal{M}_{1,2,\dots,d}(x_1, x_2, \dots, x_d)
\end{aligned} \tag{3.21}$$

with \mathcal{M}_0 a constant and the following condition:

$$\int_0^1 \mathcal{M}_{i_1 i_2 \dots i_s}(X_{i_1}, X_{i_2}, \dots, X_{i_s}) dX_k = 0, \forall k \in \llbracket i_1, i_s \rrbracket \tag{3.22}$$

Thus, the terms of the functional decomposition are orthogonal, and by various integrating of equation 3.21 (with similar definitions for the higher-order interactions):

$$\begin{aligned}
\mathcal{M}_0 &= \int_0^1 \dots \int_0^1 \mathcal{M}(\mathbf{X}) d\mathbf{X} \\
\mathcal{M}_i(x_i) &= \int_0^1 \dots \int_0^1 \mathcal{M}(\mathbf{X}) d\mathbf{X}_{/i} - \mathcal{M}_0 \\
\mathcal{M}_{ij}(x_i, x_j) &= \int_0^1 \dots \int_0^1 \mathcal{M}(\mathbf{X}) d\mathbf{X}_{/(i,j)} - \mathcal{M}_0 - \mathcal{M}_i(x_i) - \mathcal{M}_j(x_j)
\end{aligned} \tag{3.23}$$

where $\mathbf{X}_{/i} = (X_1, \dots, X_{i-1}, X_{i+1}, \dots, X_d)$, all input parameters except X_i , with the same type of definition for $\mathbf{X}_{/(i,j)}$ and all the higher-order variables.

By using the definition of the expected value, this enables a definition of the various terms using the first moments of \mathbf{Y} :

$$\begin{aligned}
\mathcal{M}_0 &= \mathbb{E}(\mathbf{Y}) \\
\mathcal{M}_i(x_i) &= \mathbb{E}(\mathbf{Y} | X_i = x_i) - \mathcal{M}_0 \\
\mathcal{M}_{ij}(x_i, x_j) &= \mathbb{E}(\mathbf{Y} | X_i = x_i, X_j = x_j) - \mathcal{M}_0 - \mathcal{M}_i(x_i) - \mathcal{M}_j(x_j)
\end{aligned} \tag{3.24}$$

with again similar definition for higher-order terms. The first-order interaction \mathcal{M}_i is only dependent on the variation of X_i . While the second-order

interaction \mathcal{M}_{ij} is dependent on both the respective individual interaction of X_i and X_j but also their simultaneous variation.

Variance decomposition

The squared integration of the functional decomposition in equation 3.21 gives us:

$$\int_{[0,1]^d} \mathcal{M}^2(\mathbf{X}) d\mathbf{X} - \mathcal{M}_0^2 = \sum_{s=1}^d \sum_{i_1 < \dots < i_s}^d \int_{[0,1]^s} \mathcal{M}_{i_1 \dots i_s}^2(X_{i_1}, \dots, X_{i_s}) dX_{i_1} \dots dX_{i_s} \quad (3.25)$$

The left term of equation 3.25 is equal to $\mathbb{E}(\mathbf{Y})$ the variance of \mathbf{Y} , while the right terms can be expressed as variance with conditional values using equation 3.24. Thus, a decomposition of the variance expression can be expressed as:

$$\begin{aligned} \text{Var}(\mathbf{Y}) &= \sum_{s=1}^d \sum_{i_1 < \dots < i_s}^d V_{i_1, \dots, i_s} \\ \text{Var}(\mathbf{Y}) &= \sum_{i=1}^d V_i + \sum_{(i,j), i < j}^d V_{ij} + \dots + V_{12 \dots d} \end{aligned} \quad (3.26)$$

with the following definitions for the partial variance terms:

$$\begin{aligned} V_i &= \text{Var}_{X_i}(\mathbb{E}_{\mathbf{X}/i}(\mathbf{Y}|X_i)) \\ V_{ij} &= \text{Var}_{X_i X_j}(\mathbb{E}_{\mathbf{X}/ij}(\mathbf{Y}|X_i, X_j)) \\ V_{i_1, \dots, i_s} &= \text{Var}_{X_{i_1} \dots X_{i_s}}(\mathbb{E}_{\mathbf{X}/i_1 \dots i_s}(\mathbf{Y}|X_{i_1}, \dots, X_{i_s})) \end{aligned} \quad (3.27)$$

The variance can be decomposed in a sum of variance-based terms showing the dependency on each input individually (the V_i in equation 3.26) but also the second-order (V_{ij}) and higher-order interactions between the various input parameters.

Sobol' indices

Using the variance decomposition in equation 3.26, a sensitivity tracker S_u can be defined for any combination of any order of input parameters, $\forall \mathbf{u} = (i_1, \dots, i_s) \in \llbracket 1, d \rrbracket^s, i_1 < \dots < i_s$:

$$S_{i_1, \dots, i_s} = \frac{V_{i_1, \dots, i_s}}{\text{Var}(\mathbf{Y})} \quad (3.28)$$

The most commonly used Sobol' indices is the first order Sobol' index, $\forall i \in \llbracket 1, d \rrbracket$:

$$S_i = \frac{V_i}{\text{Var}(\mathbf{Y})} = \frac{\text{Var}_{X_i}(\mathbb{E}_{\mathbf{X}_{/i}}(\mathbf{Y}|X_i))}{\text{Var}(\mathbf{Y})} \quad (3.29)$$

which emphasizes the impact of the parameter P_i alone on the output model compared to other parameters. The closest it is to one, the biggest impact it produces on the model. Higher-order Sobol' indices can be interpreted in the same way, as the sensitivity of the output model is observed regarding the variations of several input parameters simultaneously, the effect each input cannot be separated from the others. The total sum of all orders Sobol' indices verifies:

$$\sum_{i=1}^d S_i + \sum_{(i,j), i < j}^d S_{ij} + \dots + S_{12\dots d} = \sum_{\{\mathbf{u}, \mathbf{u} \subseteq \llbracket 1, d \rrbracket\}} S_{\mathbf{u}} = 1 \quad (3.30)$$

Total indices

For high dimensional output models, the observation of all orders Sobol' indices can be difficult due to the high number of combination. Therefore, for an input variable X_i , a total-effect index (or total Sobol' index) S_i^T is defined by summing all the Sobol' indices using this variable:

$$S_i^T = \sum_{\{\mathbf{u}, \mathbf{u} \subseteq \llbracket 1, d \rrbracket \text{ and } i \in \mathbf{u}\}} S_{\mathbf{u}} \quad (3.31)$$

Unlike S_i where according to equation 3.30: $\sum_{i=1}^d S_i \leq 1$, this time the sum of all the total Sobol' indices is greater than one:

$$\sum_{i=1}^d S_i^T \geq 1 \quad (3.32)$$

Indeed, for example for a given couple (X_i, X_j) of input parameters, S_{ij} is counted for both S_i^T and S_j^T . The equality case for inequality 3.32 is for an output model purely additive. The information given by S_i^T is different from the one given by S_i , for example $S_i \ll 1$ does not imply necessarily $S_i^T \ll 1$. A total Sobol' index close to zero means that the input parameter is almost not affecting the output model, which can be useful for further simulations and experimental designs.

3.1.6 PCE-based sensitivity analysis

Usually the Sobol' indices (see equation 3.28) are computed with Monte Carlo simulation which leads to a numerous amount of evaluation for the output model \mathcal{M} to perform the sensitivity analysis. Thanks to metamodelling, a predictor $\widehat{\mathcal{M}}$ can be used instead to greatly reduce the computation time.

If the metamodel is PCE, even more computation time can be saved as the various Sobol' indices can be extracted directly from the PCE decomposition [84].

Let us consider a truncated PCE metamodel (see equation 3.13) with the finite truncation multi-indices $\mathcal{A} \subset \mathbb{N}^d$ for d input parameters, the sum can be reordered in increasing orders:

$$\widehat{\mathcal{M}}(\mathbf{x}) = y_0 + \sum_{\{\mathbf{u}, \mathbf{u} \subseteq \llbracket 1, d \rrbracket\}} \sum_{\alpha \in \mathcal{A}_{\mathbf{u}}} y_{\alpha} \psi_{\alpha}(\mathbf{x}) \quad (3.33)$$

with $\mathcal{A}_{\mathbf{u}}$ a subset of \mathcal{A} with only non-zero components. Thus, containing all the α_k such as $k \in \mathbf{u}$.

The terms of the Sobol' decomposition (see equation 3.21) can also be written using the generic index $\mathbf{u} = \{i_1, \dots, i_k\} \subseteq \llbracket 1, d \rrbracket$:

$$\widehat{\mathcal{M}}(\mathbf{x}) = \mathcal{M}_0 + \sum_{\{\mathbf{u}, \mathbf{u} \subseteq \llbracket 1, d \rrbracket\}} \mathcal{M}_{\mathbf{u}}(\mathbf{x}_{\mathbf{u}}) \quad (3.34)$$

with $\mathbf{x}_{\mathbf{u}}$ the subvector of \mathbf{x} obtained by extracting only the components from the inputs indexed inside \mathbf{u} .

Due to the uniqueness of the Sobol' decomposition, the terms in $\mathcal{M}_{\mathbf{u}}(\mathbf{x}_{\mathbf{u}})$ can be computed directly from equations 3.33 and 3.34:

$$\mathcal{M}_{\mathbf{u}}(\mathbf{x}_{\mathbf{u}}) = \sum_{\alpha \in \mathcal{A}_{\mathbf{u}}} y_{\alpha} \psi_{\alpha}(\mathbf{x}) \quad (3.35)$$

As developed in Section 3.1.5, the variance-based terms can be computed from this decomposition with the corresponding Sobol' indices:

$$\begin{aligned} \text{Var}(\mathbf{Y}) &= \sum_{\alpha \in \mathcal{A}} y_{\alpha}^2 \\ \text{Var}_{\mathbf{X}_{\mathbf{u}}}(\mathbb{E}_{\mathbf{X}_{/\mathbf{u}}}(\mathbf{Y}|\mathbf{X}_{\mathbf{u}})) &= \sum_{\alpha \in \mathcal{A}_{\mathbf{u}}} y_{\alpha}^2 \\ S_{\mathbf{u}} &= \frac{\sum_{\alpha \in \mathcal{A}_{\mathbf{u}}} y_{\alpha}^2}{\sum_{\alpha \in \mathcal{A}} y_{\alpha}^2} \end{aligned} \quad (3.36)$$

3.2 Analysis of a simplified WPT model

The use of these surrogate techniques has first been achieved on a simplified model, thus easier to tune. The goal was to observe the usefulness of using metamodelling for reducing the computation time in order to perform an accurate sensitivity analysis.

3.2.1 Description of the first input model

I build a first model on COMSOL Multiphysics® (figure 3.3) of a dynamic WPT system studied by Vincenzo Ciremele during his PhD in our research

unit [85]. The system consists in a transmitting coil (in the ground), a smaller receiving coil (in the car). The receiving coil is topped by two ferrites which aims at focusing the Magnetic Flux. Finally only on top of the receiving coil, I modelled a portion of the shield on the car body as most of the magnetic field intensity is focusing in that area. This prevents us from doing useless computations by reducing the size of the mesh on COMSOL. Indeed as COMSOL uses a finite element approximation method, considering our problem ($f = 85 \text{ kHz}$), the thickness of the mesh elements in the frame must take into account the skin depth.

With such dimensions (table 3.3), I managed to design a COMSOL model with a mesh of ~ 8000 elements (see figure 3.4) running in less that two minutes on our computation units. This enabled us to compute several sets of input parameters in a few hours, which is enough to build consistent metamodels.

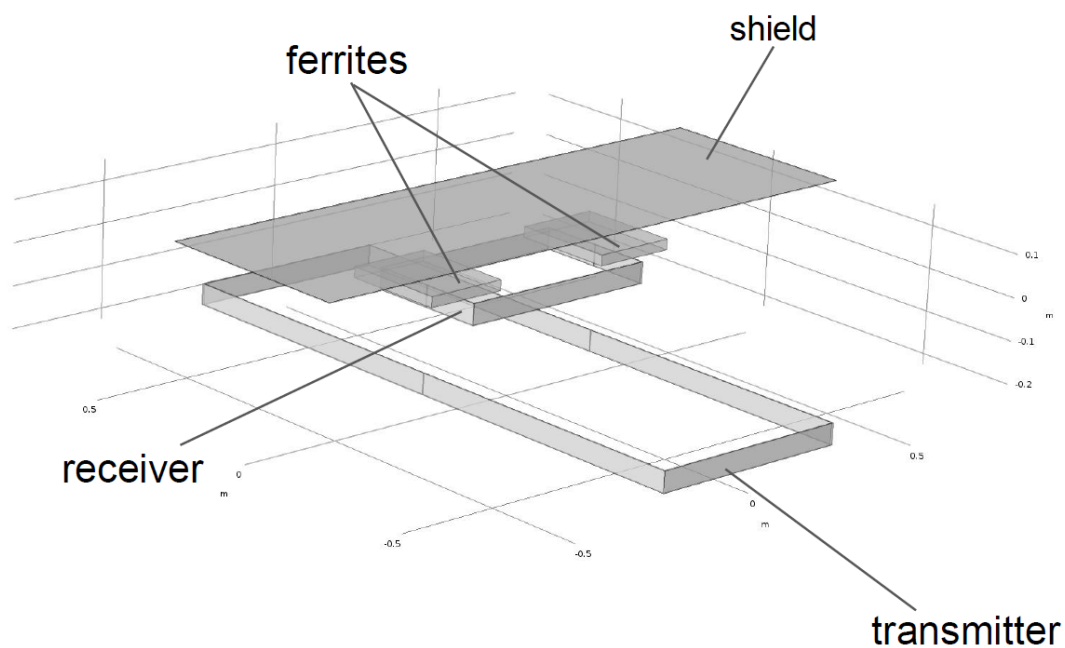


Fig. 3.3 Our COMSOL model based on the WPT system studied in Vincenzo Ciremele's PhD [85]

Table 3.3 Dimensions of our first COMSOL model (see figure 3.3)

dimensions	value	unit
transmitting coil length	1.5	m
transmitting coil width	0.5	m
receiving coil length	0.3	m
receiving coil width	0.5	m
distance between the coils	0.2	m
shield portion length	0.5	m
shield portion width	1.5	m
shield thickness	1	mm

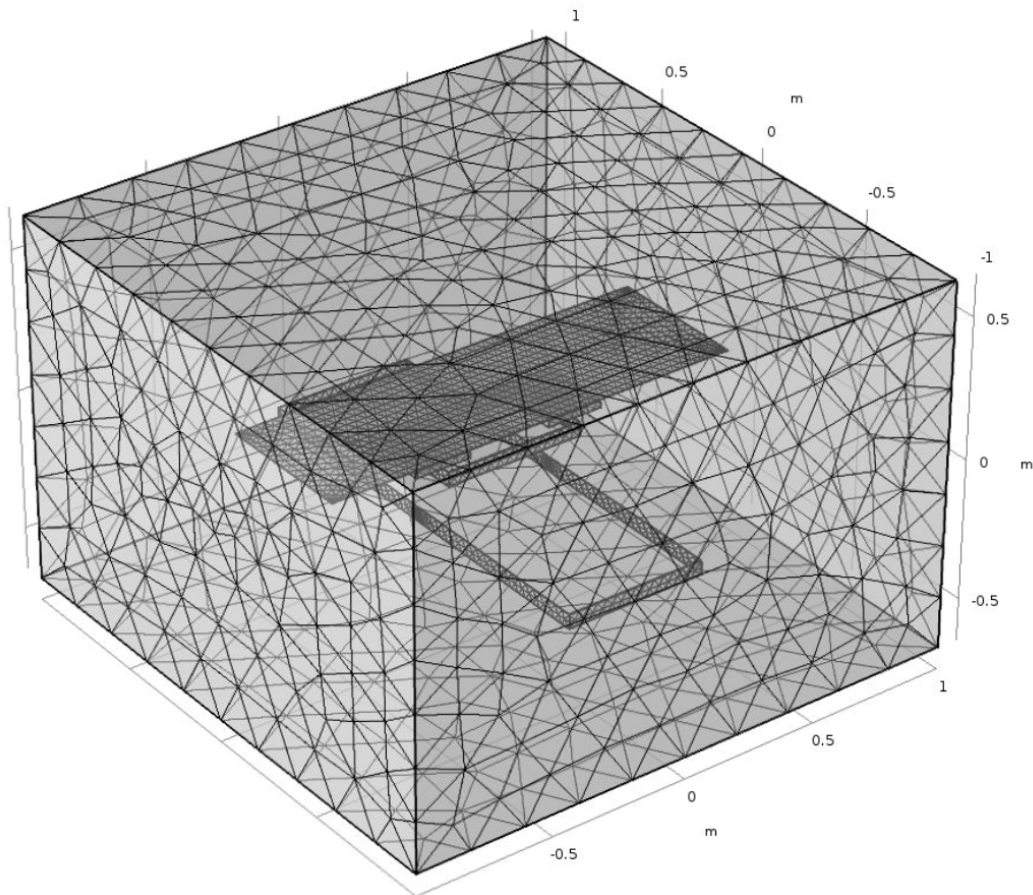


Fig. 3.4 Mesh of our COMSOL model

3.2.2 Kriging: trends and correlation functions tuning

Unidimensional metamodelling: first dataset

For the first try at building a metamodel, I decided to perform a sweep on the shield conductivity (see table 3.4):

- 10 values for σ_{frame} ranging from 10^4 to 10^7 S/m
- the 10 corresponding B-field values measured at a bystander position (see figure 3.5)

Table 3.4 Input dataset for our first metamodel (rounded to two digits)

X	Y
σ_{frame} (S/m)	B-field value (T)
$1.0 \cdot 10^4$	$7.3 \cdot 10^{-8}$
$2.2 \cdot 10^4$	$7.3 \cdot 10^{-8}$
$4.6 \cdot 10^4$	$7.3 \cdot 10^{-8}$
$1.0 \cdot 10^5$	$7.3 \cdot 10^{-8}$
$2.2 \cdot 10^5$	$7.3 \cdot 10^{-8}$
$4.6 \cdot 10^5$	$7.2 \cdot 10^{-8}$
$1.0 \cdot 10^6$	$6.7 \cdot 10^{-8}$
$2.2 \cdot 10^6$	$5.4 \cdot 10^{-8}$
$4.6 \cdot 10^6$	$3.5 \cdot 10^{-8}$
$1.0 \cdot 10^7$	$2.2 \cdot 10^{-8}$

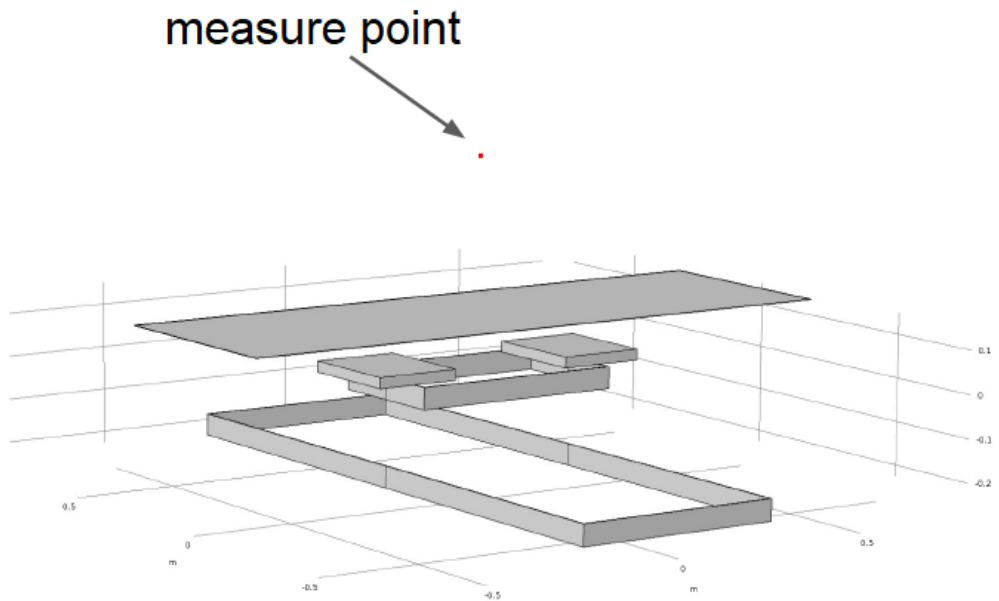
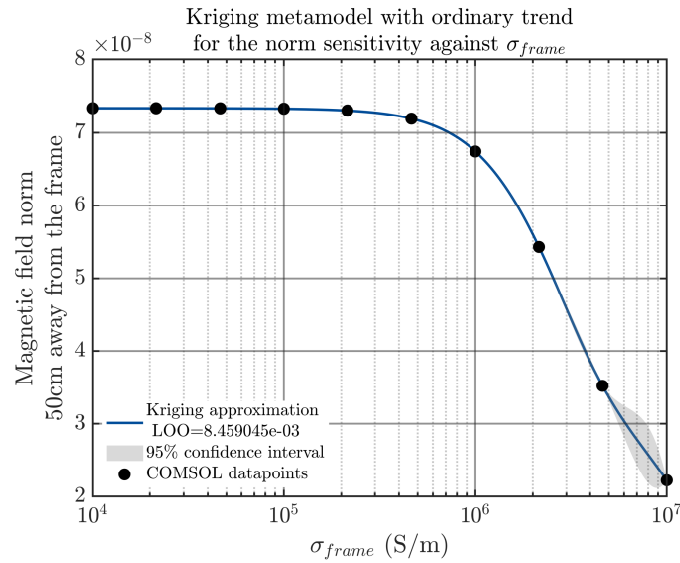


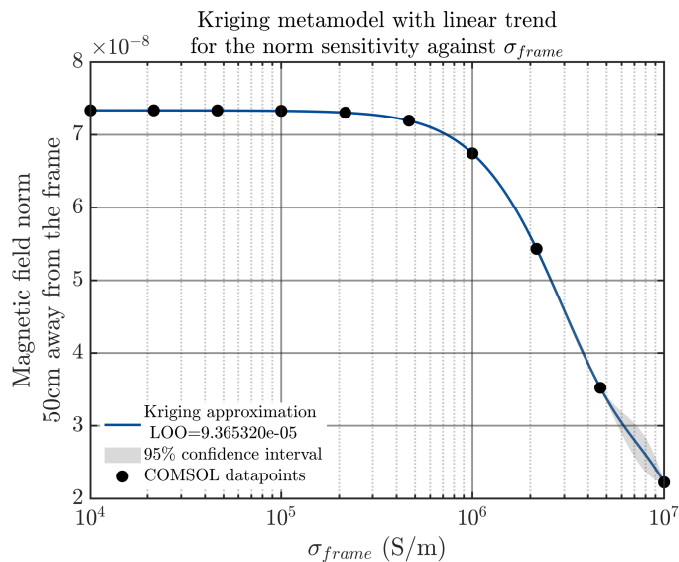
Fig. 3.5 Position of the COMSOL probe to measure the magnetic field ($x = 50\text{cm}$, $y = 50\text{cm}$ and $z = 1\text{m}$)

Metamodelling with various trends

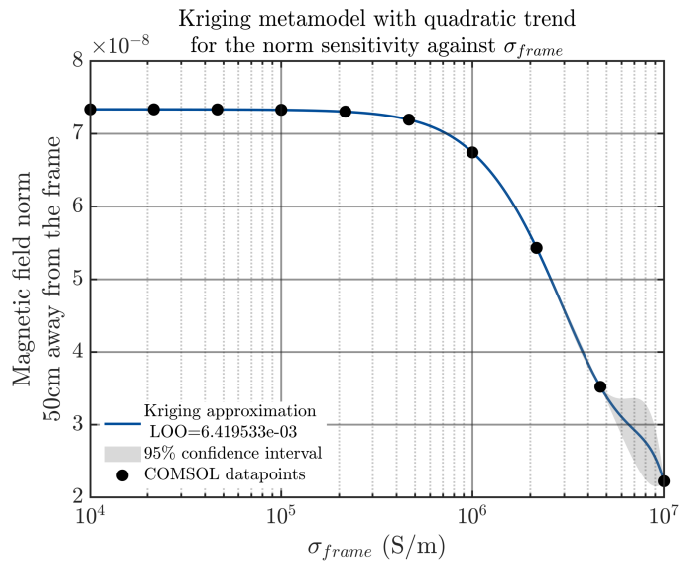
Using our input dataset (table 3.4), I compared the effects of the three most classical trends: linear, ordinary and quadratic trends (see table 3.1) in order to see which one fits our problem the most. When looking at the results for the building of our first metamodelling (figure 3.6), one can see that the metamodelling perfectly interpolate the datapoints. Moreover, apart from the last points around $\sigma_{frame} = 10^7 \text{S m}^{-1}$, the 95% confidence interval perfectly fits the curve considering the variations of the magnetic field intensity. It is also worth noticing that the intensity of the magnetic field does not exceed the levels for human exposure standards ($B < 27 \mu\text{T}$ at 85kHz). Even if all metamodelling seem extremely consistent, the LOO with the linear trend is a hundred times smaller than the ordinary one and the quadratic one. The same type of analysis has been conducted on PCK metamodelling with various trends, which showed the same result with the linear trend producing more consistent metamodelling for our magnetic field datasets. Therefore, the linear trend has been chosen for the kriging and PCK simulations onward.



(a) ordinary trend



(b) linear trend



(c) quadratic trend

Fig. 3.6 Kriging metamodel on the COMSOL model for a sweep on the shield conductivity for various trends

Correlation families tuning

Using a linear trend for the kriging metamodel with our first dataset, the various correlation families (see section 3.1.1) have been tested, the default kernel Matérn-5/2 has been compared to the other available kernels (see figure 3.7). The linear and exponential kernel are not consistent enough to be used for metamodeling this dataset due to high values for the LOO ($LOO > 10\%$). Even if the gaussian kernel produces a metamodel consistent enough ($LOO \approx 0.02\%$), the accuracy (observed in this case by the 95% confidence interval) is decreasing close to the domain limits. The last investigated kernels Matérn-3/2 and Matérn-5/2 as expected [86] are the more accurate ones. Again, the same type of analysis has been conducted on PCK metamodels to observe the same result. Due to an even better consistency, the most advanced kernel Matérn-5/2 has been chosen for future computations.

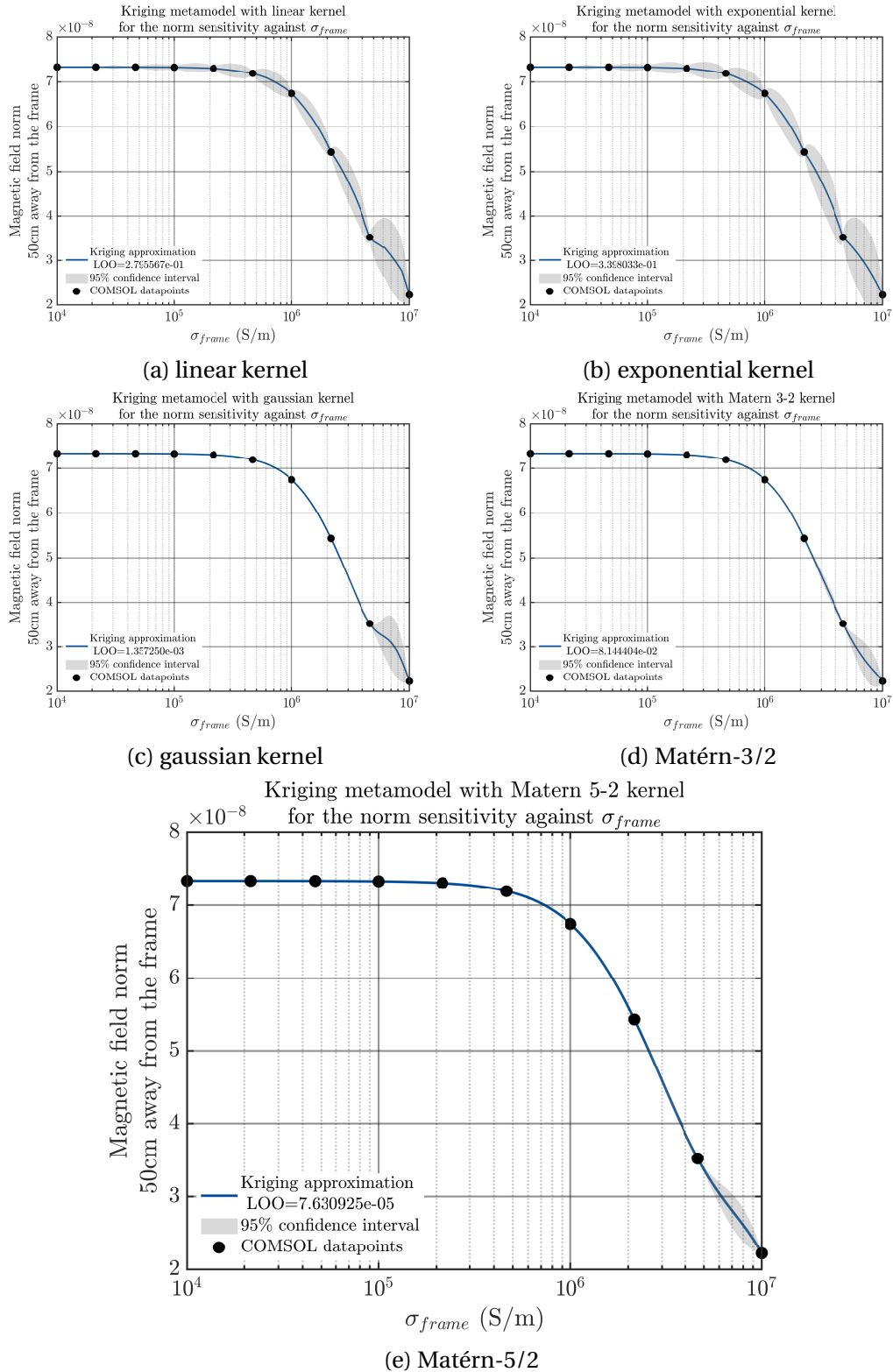


Fig. 3.7 Kriging metamodel on the COMSOL model for a sweep on the shield conductivity for various correlation families

3.2.3 Truncation schemes and computation of Polynomial Chaos-based metamodels

Bidimensional input dataset

In order to progress further in the use of metamodelling for complex models, a new dataset to try PCE on has been designed. This new sweep adds the variation of another parameter: the position of the receiving coil. The variation of this geometrical parameter (see figure 3.8) enables us to simulate the entrance and exit of the car close to a transmitter in the ground during its motion.

I decided to run the bidimensional sweep with the following ranges:

- the receiver position from 0 to 0.5m
- the shield conductivity from 10^4 to 10^7 S/m

Two bidimensional datasets of 25 (5×5) and 100 (10×10) datapoints have been produced, both with a uniform distribution for the receiver position and a log-uniform distribution for the shield conductivity. The two corresponding metamodels computed are displayed on figures 3.9 and 3.10.

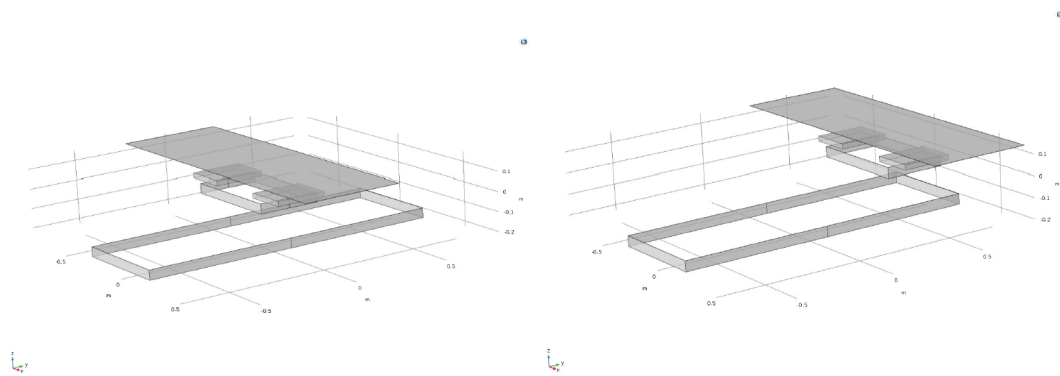


Fig. 3.8 Extreme values (0 to 0.5m) for the receiver position on the COMSOL model

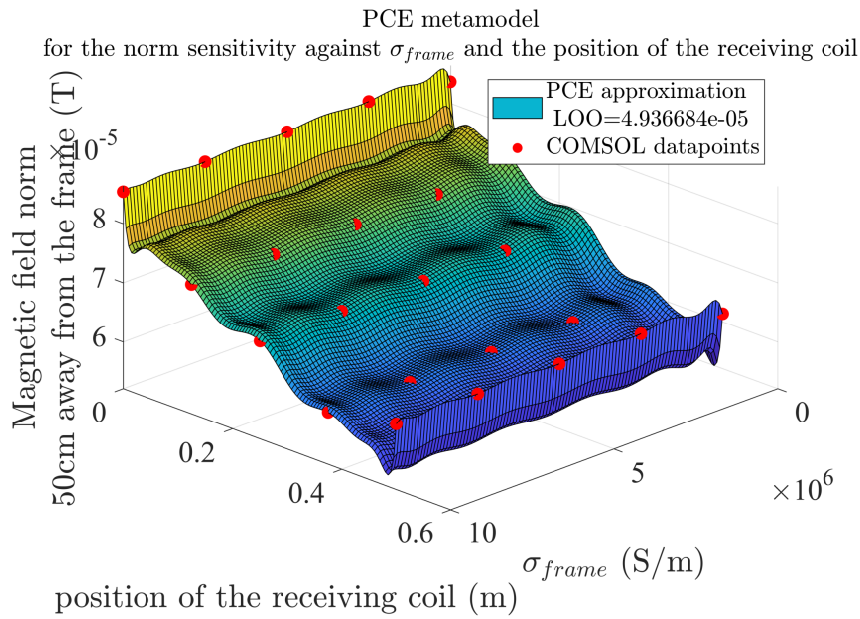


Fig. 3.9 PCE metamodel on the COMSOL model for a 2-D sweep (25 datapoints) on the shield conductivity and the receiver position

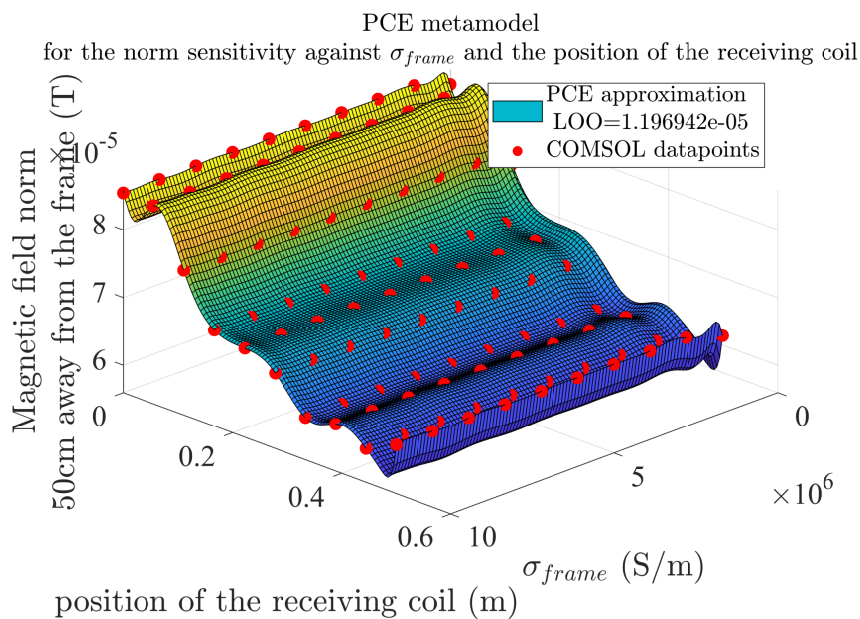


Fig. 3.10 PCE metamodel on the COMSOL model for a 2-D sweep (100 datapoints) on the shield conductivity and the receiver position with the maximum allowed degree $p = 14$

Truncation scheme for the polynomial expansion

When computing the PCE in practical the infinite sum of polynomials (see equation 3.12) has to be truncated. Usually the criteria of the truncature in equation 3.13 is degree-based, all polynomials exceeding a certain degrees are not computed when building the PCE metamodel. The goal here has been to investigate the various degrees possible to begin the truncature from.

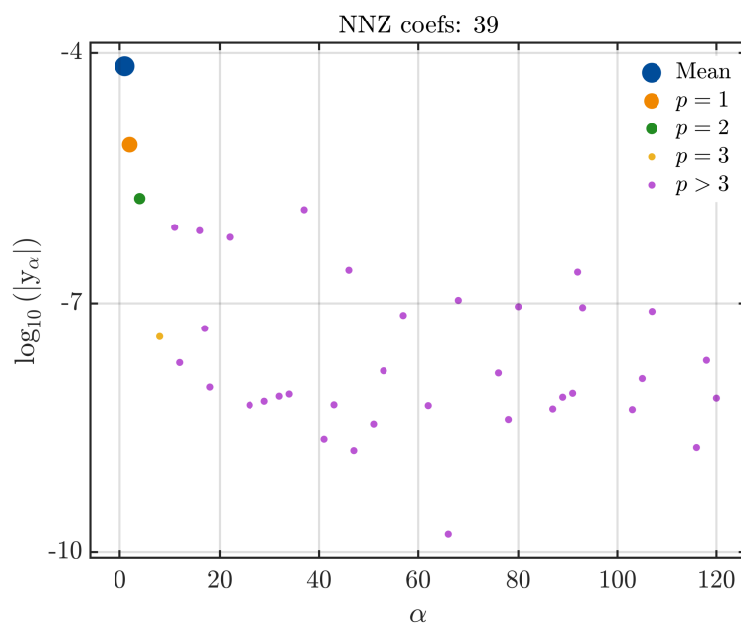


Fig. 3.11 Magnitude of the coefficients in the PCE metamodel of a 2-D sweep against the polynomial degree p

Using the dataset with 100 points, an overly accurate PCE metamodel has been built (see figure 3.10) with the maximum allowed degree $p = 14$. On figure 3.11, the values of the magnitude of the polynomial coefficients against their corresponding degree are plotted. It can be seen with the logarithmic scale that the magnitude of the polynomial expansion is extremely small as soon as the polynomial degree exceeds 3. Similar analysis with the maximum polynomial degree $p = 30, 70, 100$ have been performed showing the same type of results. Therefore for future simulations with polynomial expansion, the maximum degree of the polynomials has been set to $p_{max} = 10$ in order to avoid useless time-consuming computations.

Choice of a polynomial family

For the previously computed PCE metamodels (see section 3.2.3), the distribution of the receiver position within the parameter space has been taken uniform while the conductivity has been chosen log-uniformly. This choice is purely arbitrary and could have made differently. The usual shield materials are close to metals with conductivities ranging from, 10^6 S m^{-1} to 10^7 S m^{-1} , thus, fewer composite materials have been considered. Seemingly, no prior analysis has been conducted on this model regarding the variability of the receiver position, a Monte Carlo or LHS sampling could have been chosen but a uniform distribution has been easier to observe.

As both input variables have uniform or log-uniform distribution, the chosen polynomial family for both is *Legendre* (see 3.2). Usually the Legendre polynomials will be chosen as most of our samples distribution are either uniform or can be scaled to a uniform distribution. For further computations of either PCE or PCK metamodels the polynomial is always *Legendre* unless stated otherwise. Indeed, some polynomial families (*Laguerre* or *Jacobi*) should be avoided as their recurrence computation is not always stable [87].

3.2.4 Polynomial Chaos-Kriging metamodel parameters

As observed with both PCE metamodels (figures 3.9 and 3.10), the PCE seems adequate to estimate the global variations of our output model on this bidimensional input sweep. But even if adding more points increases the consistency (the *LOO* is approximately 5 times smaller with the 100 samples instead of 25), the irregularities on the domain borders are still present when increasing the input dataset. Using a PCK metamodel could solve this issue: the PCE is for estimating the trend (the global variation) of a kriging metamodel (the local variation).

Comparing PCE and PCK metamodels

In order to compare the gains in accuracy when using a PCK metamodel instead of a simple PCE, the PCK metamodels with both datasets from the bidimensional sweep have been computed. The results are shown on figures 3.12 (for 25 datapoints) and 3.13 (for 100 datapoints).

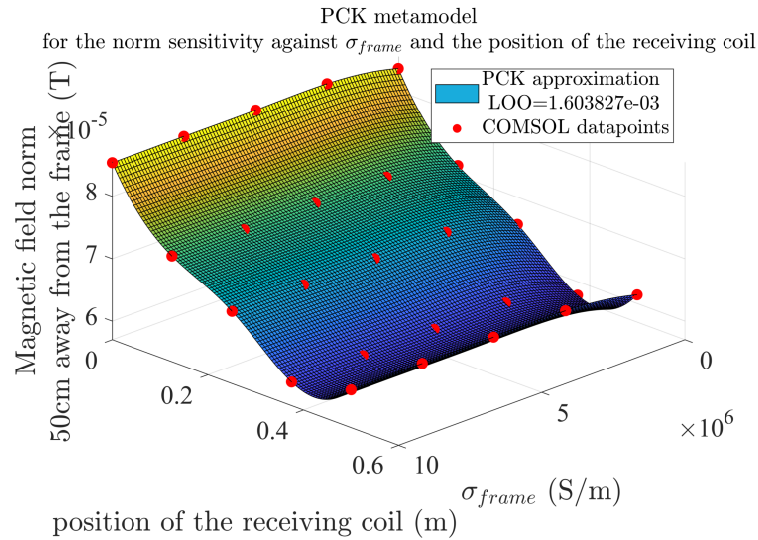


Fig. 3.12 PCK metamodel on the COMSOL model for a 2-D sweep (25 datapoints) on the shield conductivity and the receiver position

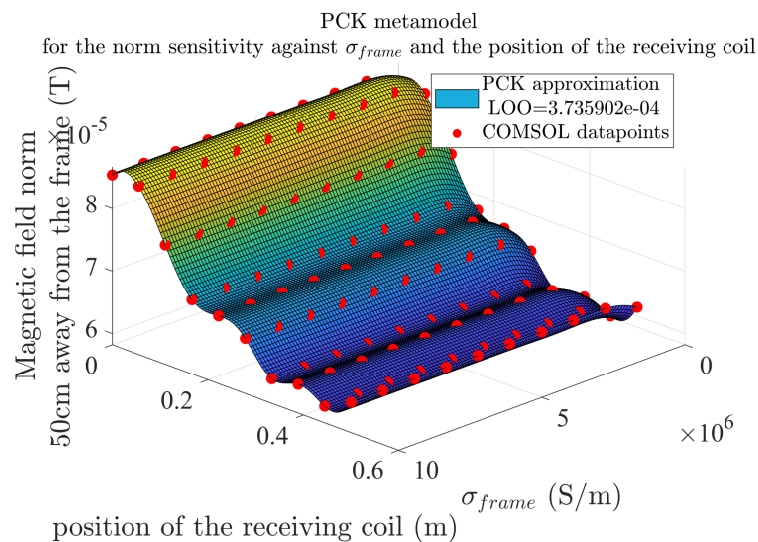


Fig. 3.13 PCK metamodel on the COMSOL model for a 2-D sweep (100 datapoints) on the shield conductivity and the receiver position

Thanks to the combination of both kriging and PCE, most of the irregularities on the domain limits have been smoothed, even if the global consistency for both datasets is smaller.

As for the PCE metamodels, the first thing that appears when comparing the *LOO* between the two metamodels is that adding more points increases the consistency. But for the PCE metamodel, the *LOO* is 5 times smaller, while it is not even twice smaller for the PCK. In the end, 100 datapoints had to be computed (~ 5 hours) instead of 25 (~ 1 hour) for producing metamodels just a bit more consistent. Moreover, such levels of consistency are not needed, as in any case the *LOO* is less than 1%, which is more than enough to compute an accurate sensitivity analysis.

Even if the PCK metamodels are less consistent than the PCE, again such consistencies are not needed and the output predictors are smoother. Using the input datasets, the PCK metamodels fit the physical problem the most, but in the way they were built, such models are longer to create. Fortunately even with 100 datapoints, all of our models have been created in less than a minute. That is why PCK has been chosen for further simulations for sensitivity analysis as it seems to be the most versatile metamodelling process.

Using fewer datapoints to build accurate metamodels

Based on the previous analysis, further investigations were needed to prove that fewer datapoints could be used to build consistent metamodels with sweeps of bigger dimensions. Therefore a sweep with 10 values for each of these 3 parameters has been ran:

- the receiver position from 0 to 0.5 m
- the shield conductivity from 10^4 to 10^7 S m⁻¹
- the relative magnetic permeability of the frame from 1 to 10^4

But to push the limits of our metamodels, this time the model output is 10 B-field values along a vertical line (a typical bystander position: $x = 50$ cm, $y = 50$ cm and $z = 0$ to 2 m) as shown in red on figure 3.14.

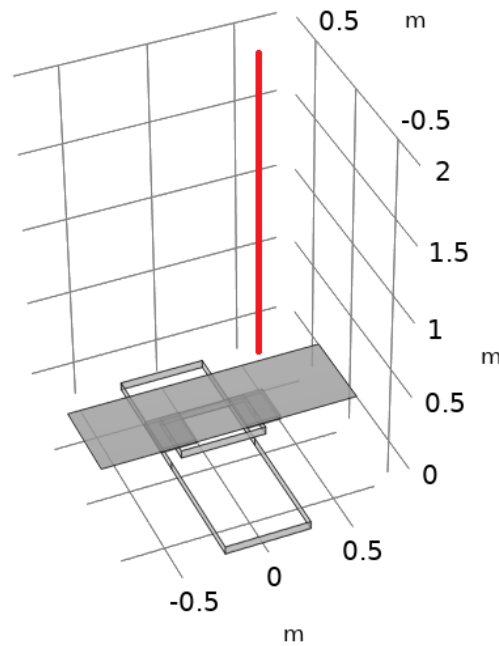


Fig. 3.14 Investigation line (in red) on COMSOL for a typical bystander position, 10 values along $x = 50$ cm, $y = 50$ cm and $z = 0$ to 2 m

I built 3 different PCK metamodels, one using the full set of 1000 datapoints, one with 125 datapoints and the last one with only 27 points. The chosen samples are uniformly distributed within the parameter space (figure 3.15).

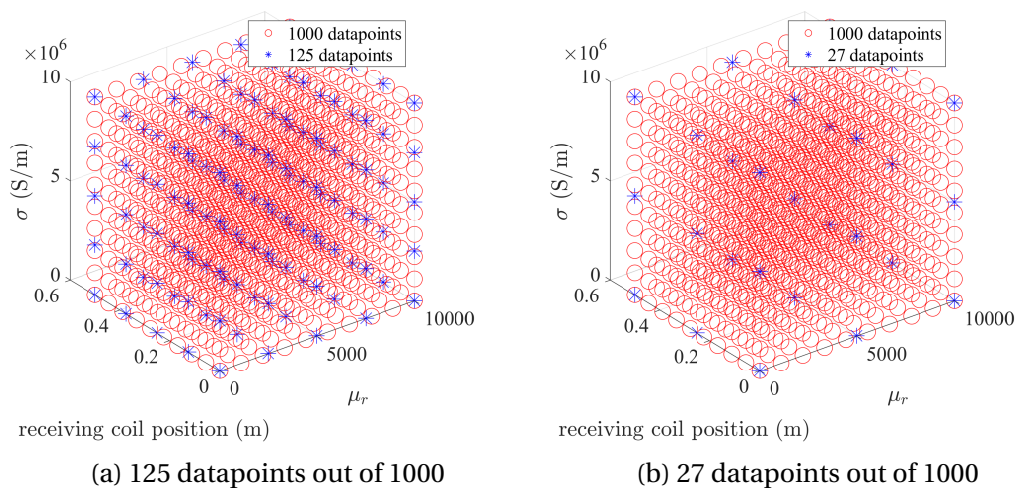


Fig. 3.15 Chosen samples in the parameter space for the accuracy comparison of PCK metamodels on a 3-D sweep: 27 (on the right) and 127 datapoints (on the left)

The three metamodels have been faced against each other to compare their performance at computing sensitivity analysis using the Sobol' indices (see section 3.1.5). The results are displayed in table 3.5. It can be seen again that increasing the number of input datapoints provides indeed a better consistency, which is still unnecessary as the model with 27 datapoints is consistent at $\sim 0.0003\%$. Moreover the Sobol' indices, which are almost not affected by the number of datapoints, highlight logically the receiver position (the only geometrical parameter) as the most significant parameter, while the permeability of the frame has no effect compared to its conductivity. All in all, computing 1000 datapoints (~ 2 days of computation) is more than unnecessary to perform a simple sensitivity analysis. A few hours would have been enough using either 125 or 27 datapoints.

Table 3.5 Properties of the output metamodels on the 3-D sweep ($S_{\mu_r} = 0$ at 3 significant figures)

Subset size (k samples)	LOO	S_{μ_r}	S_{rcpos}	S_{σ}
1000	$2.854 \cdot 10^{-11}$	0	0.997	0.0027
125	$3.782 \cdot 10^{-8}$	0	0.995	0.0044
27	$3.217 \cdot 10^{-6}$	0	0.975	0.024

But here the samples have been chosen uniformly inside the parameters space and, by doing so the build of a smaller dataset enabled us to perform an accurate sensitivity analysis at a small computation cost. The choice of using a uniform distribution has purely been arbitrary and could be different when using another dataset or another output model. Even if the built-in output model is a fairly simple FEM model and therefore no generalization nor general computation method can be drawn from these computations, yet the analysis and the chosen outputs made our model complex. That is why we decided to expand our analysis to even more complex models where the gain of computing less datapoints to perform sensitivity analysis could be even easier to observe.

3.3 A realistic car model

3.3.1 The INRiM model

In the framework of the MICEV project [2], Oriano Bottauscio and Mauro Zucca provided us some results using a complex WPT car model (see figure 3.16). This model has been created with the OPERA software and the frame is based on a Volvo car model. The model output is a 100 by 1 vector: 100 B-field values along a vertical line (a bystander position). Several positions for both the bystander and the coils can be considered as shown on figure 3.17. The IPT system has been built with the following properties:

- Power: 7.5 kW, frequency: 85 kHz
- Transmitter coil m.m.f.: 208 A r.m.s.
- Receiving coil m.m.f.: 208 A r.m.s. ($\varphi = 90^\circ$)
- 3 positions: Front/Central/Rear

In our simulations the charging pads have been considered in a central position and the bystander aside the car in position B2 as shown on figure 3.18.

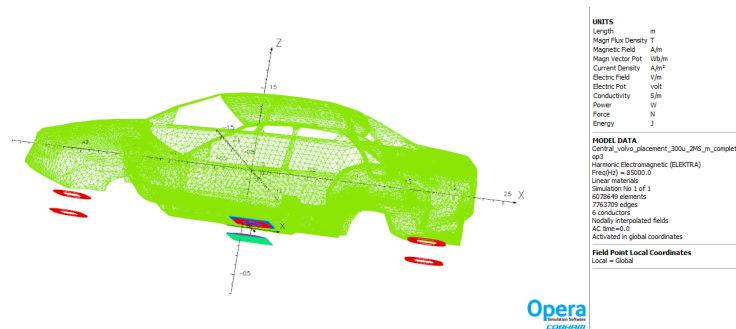


Fig. 3.16 INRiM WPT car model (credits to Oriano Bottauscio and Mauro Zucca)

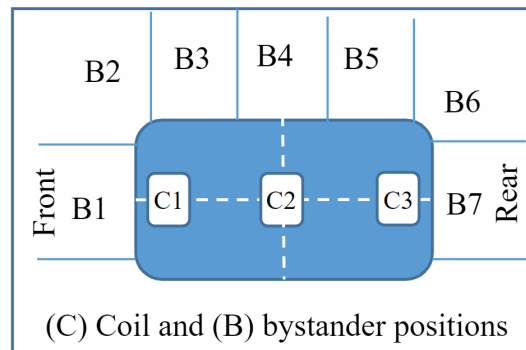


Fig. 3.17 Different coil and measure positions available in the INRiM model

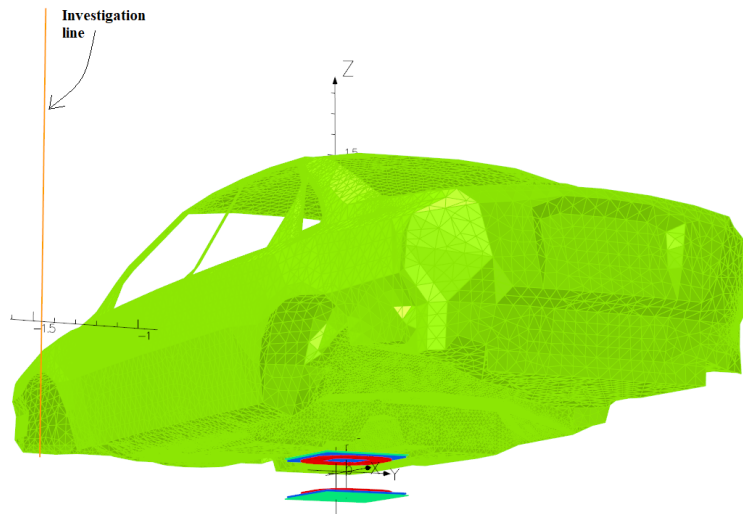


Fig. 3.18 FEM mesh model of the INRiM model with the central position and the investigation line

3.3.2 Sub-sampled metamodels

Randomly chosen samples on a bidimensional sweep

The INRiM provided us some pre-existing datasets with the conductivity of the chassis σ and the relative permeability of both the chassis μ_r and the charging pad μ_f (see table 3.6).

The first goal has been to perform a sensitivity analysis on this new complex model for different sub-samples sizes. For the previous FEM model the sub-sampling was uniformly distributed in the parameter space. Us-

ally uniform sampling is not the most suitable method, random sampling, Monte Carlo sampling or LHS is preferred [49]. Hence why for this model the sub-samples have been chosen randomly. Because our metamodel takes only a few seconds to compute, a lot of simulations for different random sub-samples can be performed in order to find a suitable one in terms of consistency and accuracy.

Unfortunately the first dataset provided by the INRiM is not fully exploring the parameter space as shown on figure 3.19, and by building metamodels randomly sub-sampled, some area could be completely avoided and thus the metamodel completely inaccurate. Therefore our metamodels considered only the bidimensional sweep with the frame conductivity σ and the relative permeability of the chassis μ_r , giving us 16 available datapoints.

Table 3.6 First dataset from the INRiM model: 24 datapoints with the conductivity of the chassis σ , the relative permeability of the chassis μ_r and the relative permeability of the ferrites μ_f

μ_r	σ (S m ⁻¹)	μ_f	μ_r	σ (S m ⁻¹)	μ_f
1	0	2000	300	0	100
1	10 ⁶	2000	300	0	200
1	5 · 10 ⁶	2000	300	0	500
1	10 ⁷	2000	300	0	1000
100	0	2000	300	0	2000
100	10 ⁶	2000	300	10 ⁶	2000
100	5 · 10 ⁶	2000	300	5 · 10 ⁶	100
100	10 ⁷	2000	300	5 · 10 ⁶	200
200	0	2000	300	5 · 10 ⁶	500
200	10 ⁶	2000	300	5 · 10 ⁶	1000
200	5 · 10 ⁶	2000	300	5 · 10 ⁶	2000
200	10 ⁷	2000	300	10 ⁷	2000

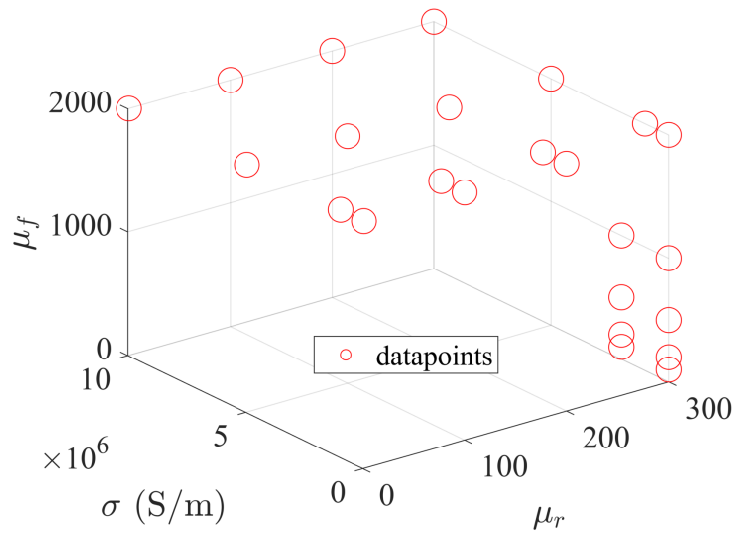


Fig. 3.19 Distribution of the different samples in the parameter space for our first dataset

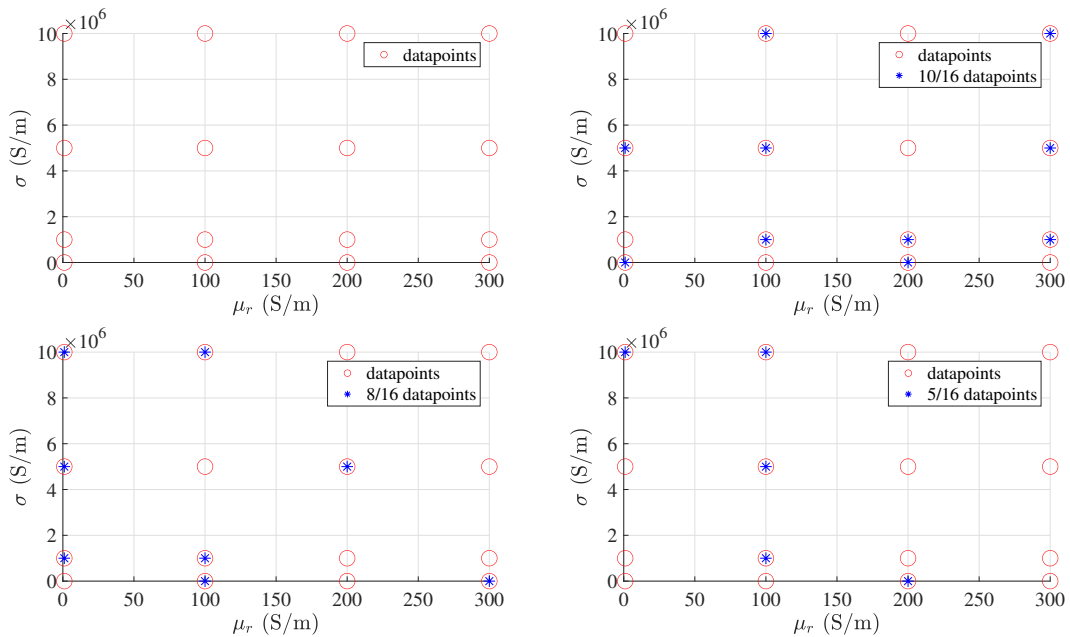


Fig. 3.20 Distribution of the different random sub-samples in the parameter space for the considered bidimensional sweep

As the INRiM model is taking a few hours to compute a single datapoint (CPU time), using fewer samples for accurate results would save a lot of time. In order to prove 16 datapoints are useless, I decided to build PCK

metamodels with 5, 8 and 10 randomly chosen datapoints (sub-samples shown on figure 3.20). The results are displayed on table 3.7.

Table 3.7 Properties of the output PCK metamodels on the bidimensional sweep from the INRiM (OSE=NaN for the full experimental design, see equation 3.19)

Subset size (k samples)	LOO	OSE	S_{μ_r}	S_{σ}
16	$1.742 \cdot 10^{-4}$	NaN	0	0.9996
10	0.02291	0.01251	0	0.9996
8	$6.219 \cdot 10^{-3}$	0.01166	$2.133 \cdot 10^{-4}$	0.9995
5	1.091	10.97	0.9996	$2.091 \cdot 10^{-4}$

These results shows us that the INRiM could have computed less datapoints when analysing the LOO and OSE (see section 3.1.4). Indeed, the full metamodel and the metamodel with 10 points (resp. 8 points) are only different by $\sim 0.34\%$ (resp. $\sim 1.2\%$) while every metamodel apart from the metamodel with 5 points are really consistent with some extremely low LOO. Of course when looking at the random sub-samples for the metamodel with 5 datapoints (figure 3.20), one can see that some area are completely ignored thus an accurate metamodel is impossible to build. The important part is that the Sobol' indices computed with the metamodels both accurate and consistent ($k = 8, 10, 16$) are similar at 3 significant figures: the frame conductivity σ is the significant parameter compared to the relative permeability μ_r of the frame. Therefore, from the point of view of a sensitivity analysis, 8 datapoints could have been enough for this input space. It is also worth noticing that these points were chosen randomly so even better metamodels could have been created using different sub-samples, and even a sub-sample with 5 points could perform an accurate sensitivity analysis.

The previous analysis has been performed on the pre-existing 3-D sweep giving decent but yet unsatisfying results due to the non-uniformity of the available samples within the input parameter space. The results are presented on table 3.8.

Table 3.8 LOO, OSE and Sobol sensitivity analysis for the sub-samples metamodels on the INRiM 3-D sweep

Subset size (k samples)	LOO	OSE	S_{μ_r}	S_{σ}	S_{μ_f}
24	$2.29 \cdot 10^{-3}$	NaN	0	0.842	$4.34 \cdot 10^{-3}$
18	$1.97 \cdot 10^{-3}$	$6.50 \cdot 10^{-4}$	0	0.918	0
12	$3.26 \cdot 10^{-2}$	$5.67 \cdot 10^{-2}$	0	0.941	0
6	0.180	1.78	0	0.609	0

Again, 12 out of the 24 available datapoints could have been enough to perform an accurate sensitivity analysis.

Extension to a five parameters analysis

We decided with the INRiM to push further our investigations and perform an analysis with five parameters but with the whole parameter space explored. For this second dataset the samples are uniformly distributed in the chosen parameter space: $\mathcal{X} = (\mu_r, \sigma, \Delta x, \Delta y, \Delta z)$ with Δx , Δy and Δz being the misalignment between the receiving and transmitting coil from the nominal position along the x, y and z axis. The following sweep has been computed on the WPT model:

- $\sigma \in \{0, 10^6\} \text{S m}^{-1}$
- $\mu_r \in \{1, 100, 300\}$
- $\Delta x \in \{-75, 75\} \text{mm}$
- $\Delta y \in \{-100, 0, 100\} \text{mm}$
- $\Delta z \in \{-50, 0, 50\} \text{mm}$

The same analysis as previous has been performed on this dataset of $n = 78$ points resulting in the LOO, OSE and sensitivity analysis displayed in table 3.9. These 78 datapoints with 5 parameters took approximately ~ 50 days in CPU time to compute.

Table 3.9 LOO, OSE and Sobol sensitivity analysis for our second metamodels

Subset size (k samples)	LOO	OSE	S_{μ_r}
78	$2.76 \cdot 10^{-4}$	NaN	$1.79 \cdot 10^{-3}$
58	$1.11 \cdot 10^{-3}$	$4.62 \cdot 10^{-4}$	$1.67 \cdot 10^{-3}$
39	$1.53 \cdot 10^{-2}$	$5.61 \cdot 10^{-3}$	$2.45 \cdot 10^{-3}$
19	$4.02 \cdot 10^{-2}$	0.248	$2.28 \cdot 10^{-3}$
S_σ	$S_{\Delta x}$	$S_{\Delta y}$	$S_{\Delta z}$
0.690	$2.09 \cdot 10^{-4}$	$9.67 \cdot 10^{-2}$	0.123
0.656	$2.55 \cdot 10^{-3}$	0.120	0.141
0.581	$1.72 \cdot 10^{-4}$	0.127	0.231
0.584	$4.43 \cdot 10^{-4}$	$9.70 \cdot 10^{-2}$	0.253

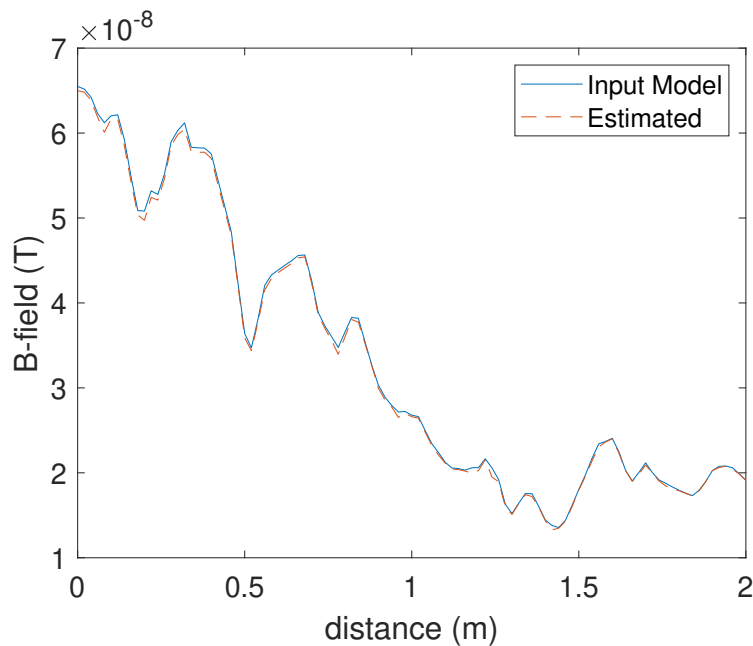


Fig. 3.21 B-field along the investigation line for the model with 39/78 datapoints (estimated) against the one with the full dataset (input model) for a given datapoint

This new metamodels are all consistent: indeed, there is less than 5% of leave-one-out error even when sampling only a quarter ($k = 19$) of the dataset. But for this metamodel the OSE is too high ($> 20\%$) thus it cannot be used as an accurate predictor for the WPT system. The predictor with

half the points ($k = 39$) is sufficiently accurate ($OSE \simeq 6\%$) regarding the full metamodel. A comparison for a single datapoint between the full PCK metamodel and the one with half the datapoints is displayed on figure 3.21. It can be observed that a sub-sample of 39 could have been enough to almost perfectly estimate the output model, thus saving ~ 25 days in CPU time. Therefore, using a more uniform parameter space enabled us to build a more consistent and more accurate metamodel with fewer points.

3.4 Conclusions

In this chapter, our first investigations on metamodels have been developed. First, by using a simple but still realistic FEM model on COMSOL for a WPT system: the meta-parameters for computing kriging, PCE and PCK surrogate models have been explored. The results from both unidimensional and bidimensional parameters sweep allowed us to choose PCK metamodels for future computations of sensitivity analysis and predictors. Then, on a much more complex model provided by the INRiM, PCK metamodels have also been proven efficient at performing accurate sensitivity analysis and building consistent predictors.

The efficiency of PCK metamodelling has been explored up to five parameters sweep. The sensitivity of the simple WPT model has been computed for bidimensional variations of both physical and geometrical parameters. The same analysis has been performed on the complex model. Even with more parameters as the previous analysis, the metamodels computed on a 5-D sweep allowed an equally accurate sensitivity analysis with the car-body conductivity still being the significant parameter against new geometrical parameters as for the COMSOL model. The Sobol indices of the five parameters are here really useful for future computations. First, the influence of the relative permeability and the coils misalignment along the axis of motion is negligible against the misalignment along the y-axis and the z-axis and the car-body lamination conductivity. Thus, future sensitivity analysis on this five parameters can be reduced to three parameters, or less samples can be taken from the non-significant parameters and more samples can be given to the significant ones. Then, such an analysis can

help with the design of real WPT systems where a greater care should be given to the uncertainties on dimensioning the chassis conductivity and the system along the y and z-axis.

An interesting part of this investigation has been to compute metamod-els using fewer datapoints from a given dataset. On the simple COMSOL model, uniform sub-samples of 27 datapoints and 125 datapoints out of 1000 available could have been enough to compute an accurate sensitivity analysis. By expanding this analysis to the INRiM model, some random sub-samples have been drawn from available datasets (2-D, 3-D and even 5-D sweeps). And again, computing less datapoints (39 out of 78 on the five pa-rameters sweep) is enough. Therefore on both models, a lot of computation time could have been saved (~ 25 days on the INRiM model for example) by avoiding the computation of some datapoints. This observation makes us realize the importance of the sample design for our WPT analysis. Thus emerged the idea of developing an adaptive algorithm to build a consistent predictor for a given WPT output model using the combination of PCK and a sub-sampling technique. The development and investigations of this method are developed in the next chapter.

The use of random sub-samples could also prove the use of metamod-els to build predictors for experimental results. The difficulty at performing accurately a uniform (or any particular) sweep at an experimental level could be avoided by using metamodelling. The variations of the output experimental model could be computed using the available predictor and less time could be spent at both calibrating and measuring data to perfectly fit the targeted dataset: the uncertainties could be greatly reduced. This aspect will be developed in section 5.3.

Chapter 4

Active learning metamodelling

The use of metamodels has been proven extremely useful at building consistent predictors but also at performing accurate sensitivity analysis on both complex and simple WPT models (see chapter 3). But more importantly it has been observed that computing less datapoints than the existing datasets for these models could be possible to perform analysis with similar accuracy. Based on this observation, this section describes the development of our adaptive algorithm that tries to compute as less samples as possible from a given model output in order to compute a consistent PCK metamodel. Our sampling strategy will be compared to some classical "static" sampling strategies in terms of input model computations to show the use for saving computation time. The metamodel will then be used along with its consistent predictor to compute a sensitivity analysis on the output model.

4.1 Subgridding technique

Sampling strategies can be classified in two categories: static ("one-shot") sampling and sequential sampling (see figure 4.1 from [88]). In static sampling, the sample size and the input dataset are chosen prior to the model evaluation. But in the case of our metamodelling processes, the input model is rather costly and its response is unknown. Thus, it is hard to determine an a priori sample which would result in a consistent surrogate model. Hence why, sequential sampling methods have been developed,

where the input dataset is modified based on previous computations along the build of the metamodel.

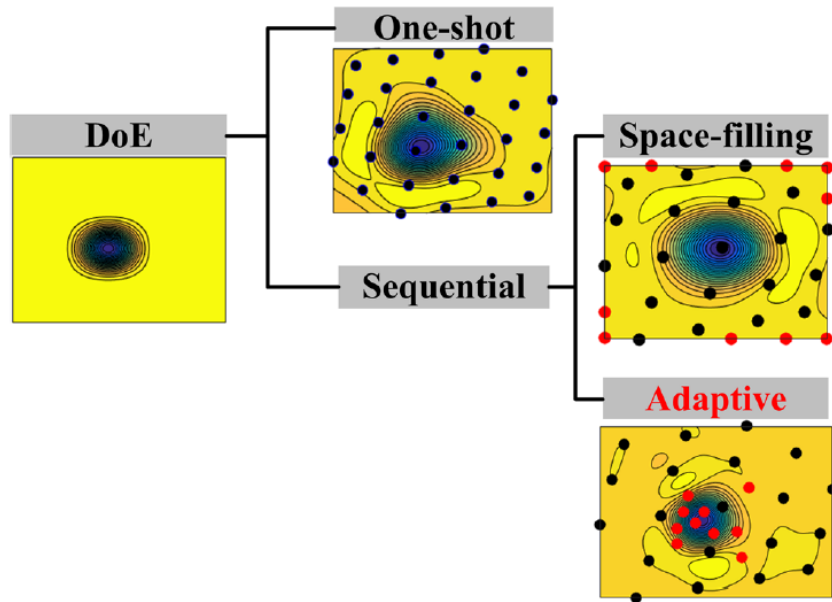


Fig. 4.1 Visual representation of different sampling strategies, taken from [88]

Sequential sampling strategies can be classified under two approaches: space-filling sampling and adaptive sampling. Space-filling strategies aim at exploring the whole input parameter space and are usually derived from static sampling strategies but the datapoints are chosen sequentially. While, the goal of an adaptive sampling strategy (also called active learning) is to start from a rather low number of samples and expand it in the regions of interest of the model response (red samples on figure 4.1). This results with a relatively low number of calls of the input model compared to space-filling strategies for the same level of metamodel consistency.

4.1.1 Adaptive sampling strategy

Active learning algorithm

The general flowchart of an adaptive sampling strategy for surrogate modeling is displayed on figure 4.2. Given an input parameter space \mathcal{X} for an

expensive computational model \mathcal{M} , N samples are drawn from it $\mathbf{X} = (X_1, \dots, X_N)$. Their corresponding model responses are computed $\mathbf{Y} = (Y_1, \dots, Y_N)$ and a first metamodel $\widehat{\mathcal{M}}$ is computed using this dataset. If such a metamodel is not accurate, new samples (along with their responses) are drawn in the regions of interest and the input dataset is enriched. The algorithm stops when the metamodel is accurate enough.

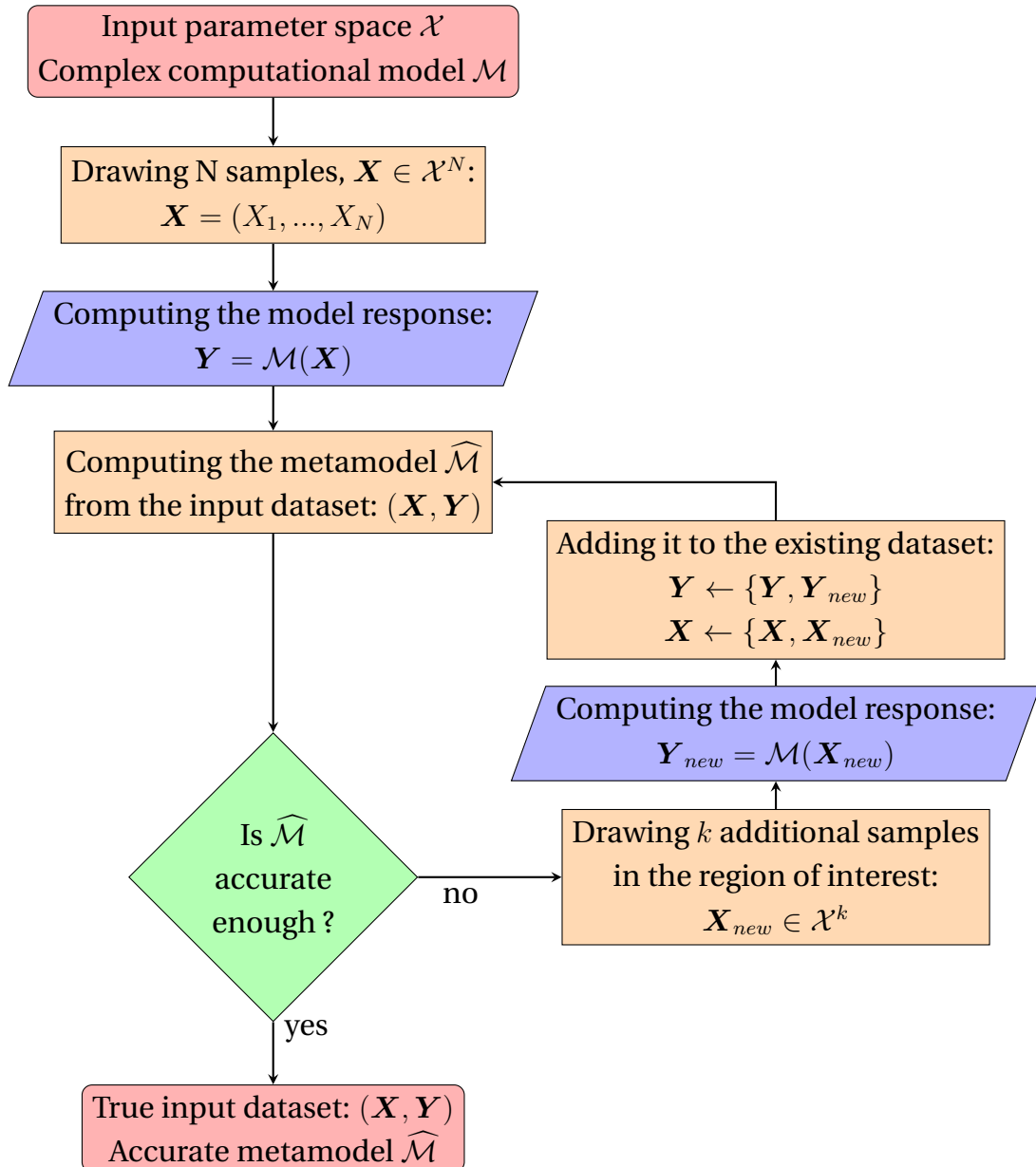


Fig. 4.2 Flowchart of an active learning metamodeling process, with the blue processes being the computationally expensive steps

Therefore, for the design of such an active learning metamodelling process, three parameters need to be explored: a local criterion to expand or not the dataset, a global stopping criterion, and obviously the sampling method for both the initial dataset and the area of interests. The general goal is to minimize the calls of the expensive model function (blue processes in the flowchart).

A local metric: the LOO

The choice of sampling strategies are important for both global (initial sample) and local (sampling of the area of interest) exploration. Most adaptive sampling strategy starts with a space-filling sampling method to explore the input parameter space as much as possible. Then, the expansion of the dataset in a local area is ruled by the observation of certain local metric. The metric can be model-dependent (variance-based, gradient-based...) which often leads to additional model calls and thus longer computation time, or independent (usually cross-validation errors) only using the existing dataset and metamodel, which can almost be computed at instant speed. Therefore, the classical Leave-one-out error (LOO) (see section 3.1.4) has been chosen for the local accuracy of our metamodel in order to minimize the call of the computational model. If the local LOO is too high in an area, more samples are needed in this part of the input parameter space. This bring the difficult choice of defining a proper threshold for the LOO as a local stopping criterion (see a discussion in [89]).

The choice of the LOO as a local stopping criteria is highly motivated by its crucial use for existing learning algorithms. For example in [90], Elisseeff, Pontil, et al. are showing the sufficient conditions for the LOO to tend to the generalization error in the case of SVM metamodels. Overall, the LOO CV-error is successful at estimating the stability of any metamodel while not being the best in every case. Moreover, within a region of interest, the use of LOO instead of other k-fold CV-error is obvious due to the low number of datapoints considered. Choosing the LOO as a local metric ensures that, in every area of interest considered within the input parameter space, the resulting metamodel is locally consistent. Therefore, the metamodel is globally consistent regarding the entire input parameter space.

The quad-tree algorithm

The choice of a CV-based adaptive sampling leads to an obvious partition design for the area of interests. In [91], Devabhaktuni and Zhang present an algorithm subdividing the regions where the test error of a Neural Network metamodel is too low. Each inaccurate region is split into 2^n sub-regions with n being the dimension of the input space. This has been notably extended to other sampling designs such as the Voronoi diagrams [92] in [93] where the most sensitive cell is subdivided based on a CV-error evaluation. Similarly, such adaptive sequential sampling has been used along with a quad-tree algorithm design [94] for computing Navier–Stokes equations in aeronautic design [95]. Although this subgridding technique is quite easy to set up, the main drawback of using it is the aforementioned curse of dimensionality, where the number of computed datapoints would explode for high-dimensional models. Luckily, most of the computational models studied here have responses only depending on a small number of parameters (which rarely exceeds 5). Performing global sensitivity analysis prior to a complete active learning algorithm can greatly reduced the number of relevant parameters for a single analysis, thus preventing us from computing too many useless datapoints.

Subdivision limitation

A local stopping criterion has been chosen with the CV LOO, along with a partitioning subgridding technique for the generation of sub-spaces within area of interests where the new samples will be drawn from. Usually a trade-off between the local and global criteria needs to be defined, with proper weights given to each metric in order to subdivide or not the current domain. But in order to tackle the curse of dimensionality which appears due to these two choices, an obvious choice for the global criterion is to set the maximum allowed number of subdivisions for the partitioning to limit the total number of computations to a fixed value. This stopping criterion could also be defined with a CV error, a relative absolute error or the jackknifing variance for example [96]. The choice of the LOO threshold ε and the maximum number of divisions m is crucial to the cheap computational

cost of the active learning algorithm and is only depending on the model behaviour and its dimensionality (see section 4.2.5).

4.1.2 Base algorithm

Let \mathcal{M} be the model output which needs to be meta-modelled, with $\widehat{\mathcal{M}}$ the corresponding metamodel. Let d be the dimension of our input parameters space \mathcal{X} . Starting from a given sample of \mathcal{X} , if the metamodel on the starting domain is not consistent enough the current domain is split into 2^d subdomains. Then, new samples are computed within each of these domains and sub-metamodels are computed on each one of them. Again, if the LOO is too high, the considered domain is subdivided and new samples are computed. The stopping criteria is either the maximum subdivision allowed m (based on the starting domain) or the LOO threshold ε . When the stopping criteria is met on all subdomains, all samples are put together to compute a metamodel on the full domain. The algorithm is creating a metamodel consistent on every subgrid of the parameter space. Thus, the metamodel built with all the samples is extremely consistent.

Algorithm 1: Subgridding algorithm

```

input :  $\mathcal{M}, \mathcal{X}$ 
output:  $\widehat{\mathcal{M}}$ 

1 define maximum division  $m$ 
2 define LOO threshold  $\varepsilon$ 
3 define number of samples on each domain  $n$ 
4  $\mathcal{D} = [\mathcal{X}]$  ▷ list of inaccurate domains
5  $\mathcal{S} = []$  ▷ list of accurate samples
6 while  $\mathcal{D} \neq \emptyset$  do
7   for  $\forall \mathcal{A} \in \mathcal{D}$  do
8     choose  $n$  samples  $X_{\mathcal{A}} = (\mathbf{x}_1, \dots, \mathbf{x}_n), \forall i \in \llbracket 1, n \rrbracket, x_i \in \mathcal{A}$ 
9     compute a PCK metamodel  $\widehat{\mathcal{M}}_{\mathcal{A}}$  with  $X_{\mathcal{A}}$  as inputs
10    if  $LOO_{\widehat{\mathcal{M}}_{\mathcal{A}}} < \varepsilon$  or  $\forall j \in \llbracket 1, d \rrbracket, \text{length}(\mathcal{A}_j) \leq \text{length}(\mathcal{X}_j)/m$ 
11      then
12         $\mathcal{S} \leftarrow \{\mathcal{S}, X_{\mathcal{A}}\}$ 
13         $\mathcal{D} \leftarrow \mathcal{D} / \mathcal{A}$ 
14      else
15         $\forall j \in \llbracket 1, d \rrbracket, \mathcal{A}_j = \{\mathcal{A}_{j,1}, \mathcal{A}_{j,2}\}, \text{length}(\mathcal{A}_{j,1}) =$ 
16           $\text{length}(\mathcal{A}_{j,2}) = \text{length}(\mathcal{A}_j)/2, |\mathcal{A}_{j,1} \cap \mathcal{A}_{j,2}| = 1$ 
17          ▷  $\mathcal{A}$  is split into two parts along every dimension
18           $\forall k \in \llbracket 1, 2^d \rrbracket, \tilde{\mathcal{A}}_k = \bigotimes_{j=1}^d \mathcal{A}_{j,k_j}, k_j \in \{1, 2\}$ 
19          ▷  $2^d$  new inaccurate domains are created
20           $\mathcal{D} \leftarrow \{\mathcal{D}, \tilde{\mathcal{A}}_1, \dots, \tilde{\mathcal{A}}_{2^d}\}$ 
21      end
22    end
23  end
24 end
25 compute a PCK metamodel  $\widehat{\mathcal{M}}$  with  $\mathcal{S}$  as inputs

```

4.1.3 Comparison of sampling methods

As already shown by our first analysis (see chapter 3), using random samples on our input parameters space could produce extremely accurate results for metamodelling with some lucky seeds. Thus the goal is to determine

the best way to draw samples from our domains using either stochastic or deterministic methods (line 8 in algorithm 1). The long term goal being to not compute a lot of datapoints due to the possible complexity of the considered output model (sometimes more than an hour to compute one datapoint), therefore a great care should be taken in saving as many datapoints as possible when drawing samples on the various domains. The methods used for generating the initial sample and all the following sub-samples have been considered identical. Thus, once a sub-domain is created with the partitioning, the samples are also exploring the whole sub-space .

This section will explore and compare the usefulness of various classical space-filling sampling methods for our subgridding algorithm. Five different sampling methods have been investigated, which all have already been proven useful in the case of adaptive sampling for surrogate modelling processes among the literature [88]. Three stochastic sampling methods have been studied:

- Latin hypercube sampling (LHS) [49]
- Sobol' sequence sampling (Sobol') [97]
- Monte Carlo sampling (MC)

Along with two deterministic methods:

- Halton sequence sampling (Halton) [98]
- Uniform sampling (quad-tree algorithm) [94]

Test functions

The algorithm with the 5 aforementioned sampling methods has been tested against several functions with bidimensional inputs that aims to cover a range of possible model output for electromagnetic device models. These test functions have been chosen purely arbitrary and this choice has only been made based on the type of output which had already been

studied and the corresponding variations observed. The four bidimensional test functions are displayed on figure 4.3.

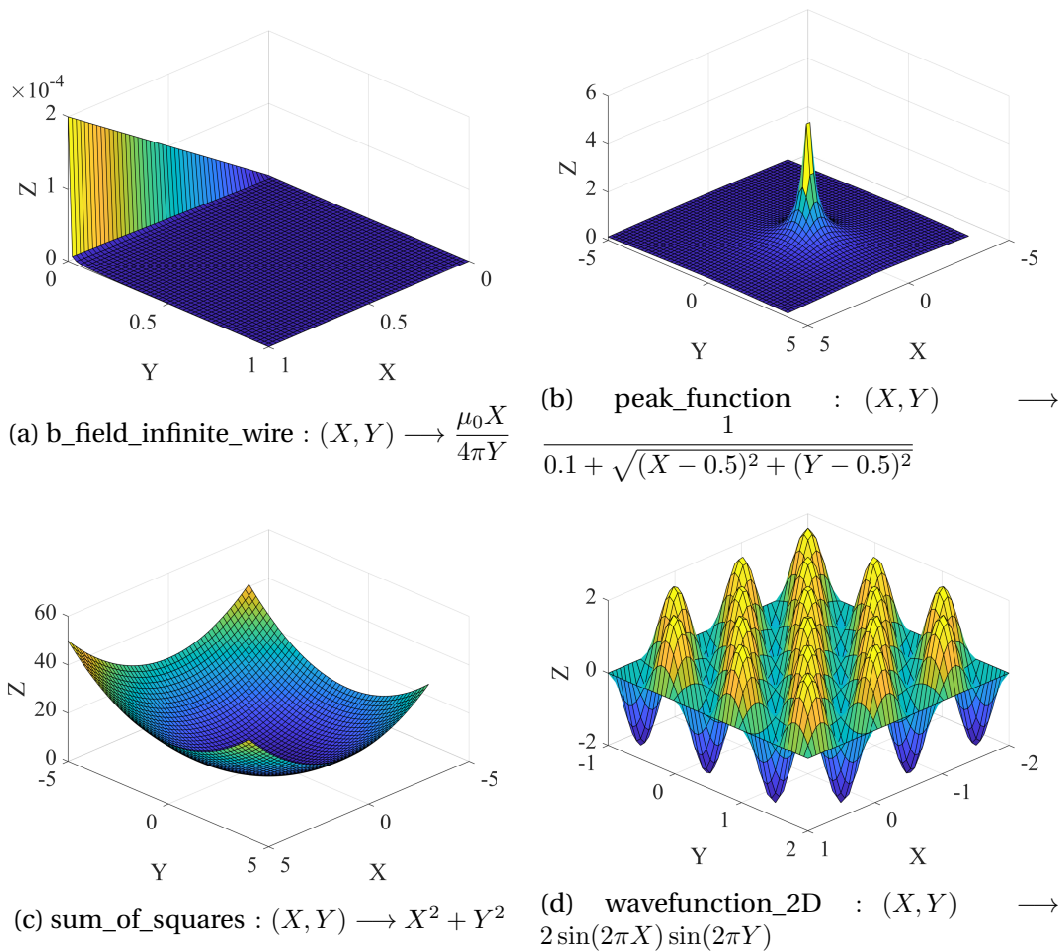


Fig. 4.3 Test functions for comparing sampling methods on our subgridding algorithm

Function `b_field_infinite_wire` is the simple function for the computation of the B-field by an infinite wire with the current X and the distance to the wire Y . The peak function is to represent a possible resonance where the whole bidimensional space is giving low values apart from the peak where the output is 10. The bidimensional wave function is exploring periodically the parameter space with a lot of extrema all locals and global at the same time.

Consistency of the metamodels

Along testing the various sampling methods on these five functions, three different values for both the LOO threshold $\varepsilon = [0.1, 10^{-2}, 10^{-3}]$ and the maximum number of division $m = [2, 3, 4]$ have been tried. Therefore 180 metamodels have been computed with our algorithm for all possible combination with $n = 5$ samples on each domain. On figure 4.4, the different number of samples $n_{samples}$ against their corresponding LOO are displayed for every functions and every sampling methods.

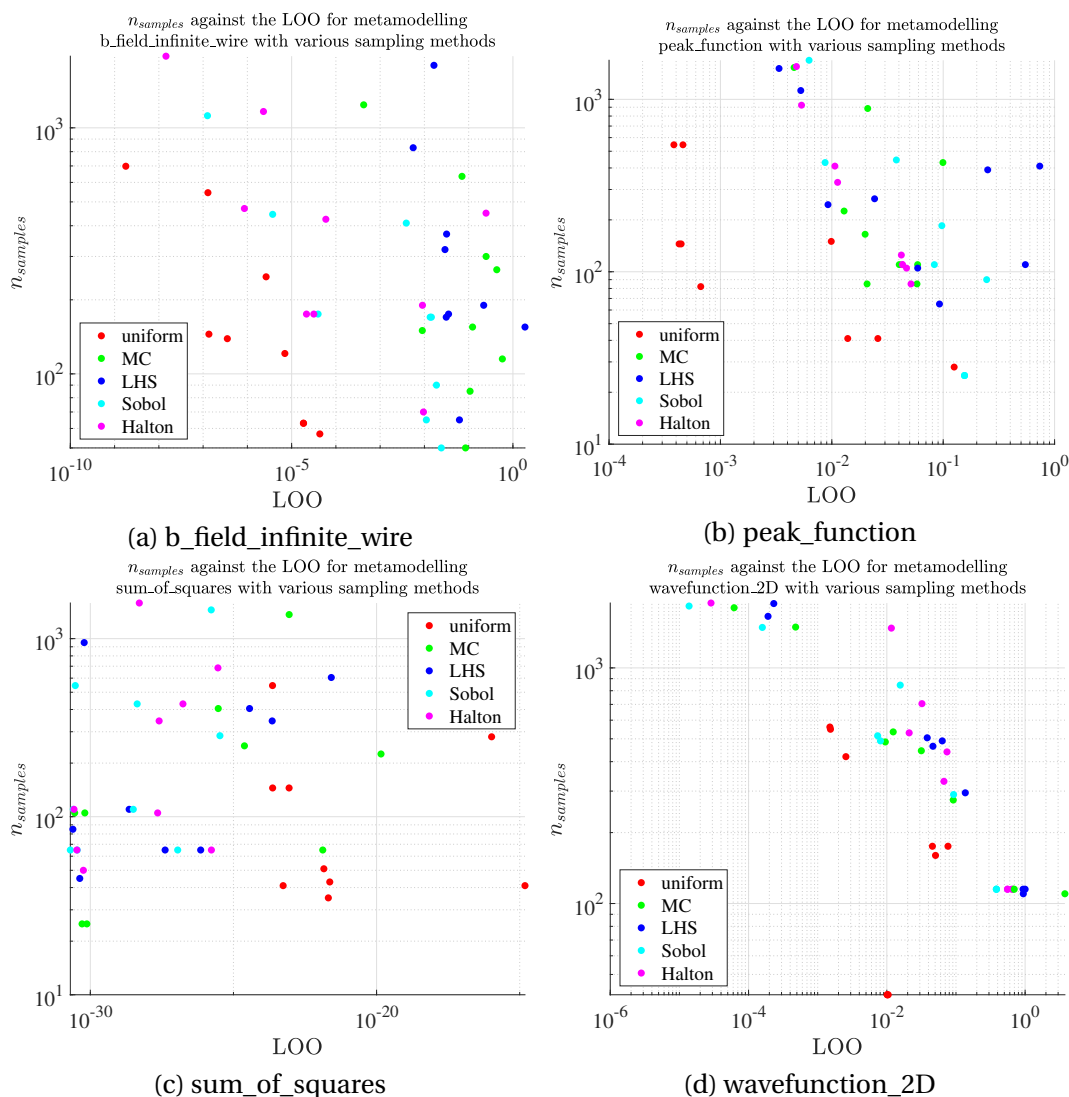


Fig. 4.4 Test functions for comparing sampling methods on our subgridding algorithm

The consistent metamodelling for performing accurate sensitivity analysis will be considered only for $LOO < 10^{-3}$. The uniform sampling is using the smallest number of samples for the smallest cross validation errors for all functions but `sum_of_squares` ((c) in figure 4.4). And for this one, some combination provided us low $n_{samples}$ values with uniform sampling but the LOO values are overly small ($< 10^{-20}$) even if not the best values which are mainly due to MC sampling. For the `peak_function` (b), the uniform sampling is the only one to produce consistent enough metamodelling with less than a thousand samples which is already too much.

Validation tests

But in order to properly assess the accuracy of the predictor at estimating the real model, four MC-generated validation sets of 100 datapoints have been created (one for every test function). On figure 4.5, the validation error R^2 (see equation 3.20) has been displayed for the 180 computed metamodelling. And again for `sum_of_squares` (c), $R^2 \sim 1$, shows us that all metamodelling perfectly estimate the real output model. For both `b_field_infinite_wire` (a) and `wavefunction_2D` (d), the uniform sampling is the best compromise for an accurate metamodelling without too many datapoints computed. But for the `peak_function` (b), the uniform sampling is not the most accurate at predicting the output metamodelling but as already shown by the previous analysis, some metamodelling with less than 10% validation error can be computed for $n_{samples} < 40$, which is enough to perform an accurate sensitivity analysis. From this second point of view, the uniform sampling is again the best sampling method to balance both the number of samples and an accurate enough predictor.

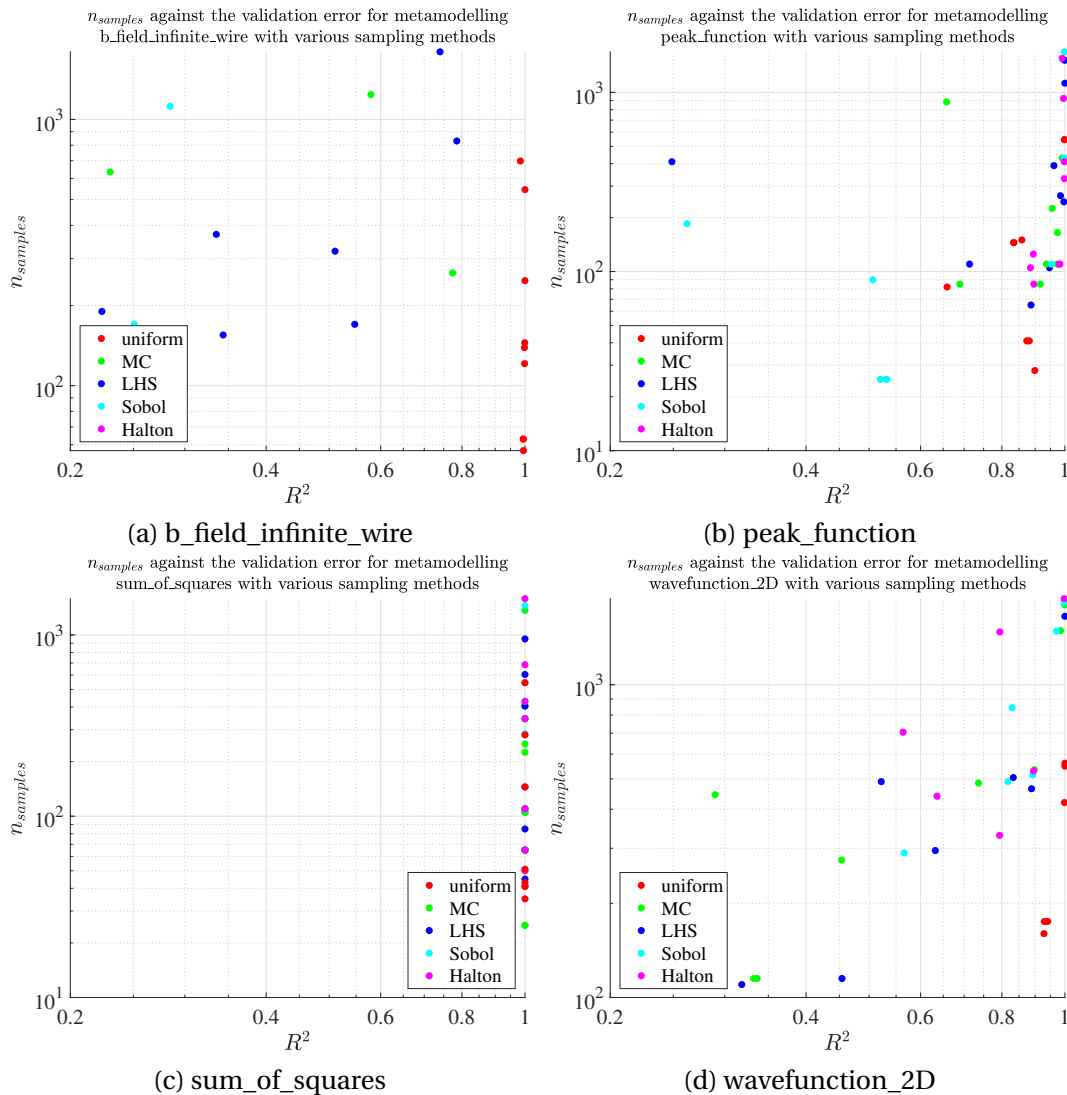


Fig. 4.5 Test functions for comparing sampling methods on our subgridding algorithm: $n_{samples}$ against the LOO of the computed PCK metamodel

Discussion

If another sampling were to be used for future computations, on these different test functions and for both analysis (see figures 4.4 and 4.5), Sobol' sequence sampling seems to provide the second best results. Using the quad-tree design, when computing new datapoints (line 8 of algorithm 1), for a given domain, some datapoints have already been previously computed. When a domain is subdivided into 2^d domains, during the next

loop of the while function, for the computation of the various metamodels, only 2^d corners needs to be added along with 2^d centers as many datapoints are already available due to previous computations. This is the main interest of using a uniform subgridding sampling instead of an LHS or MC sampling which would results on much more datapoints computed. The maximum number of datapoints computed is:

$$n_{max} = (2^m + 1)^d + 2^{dm} \quad (4.1)$$

with the number of input parameters d and the maximum subdivision allowed m .

4.2 Accurate sensitivity analysis for a dynamic WPT system

The analysis of coil pairs mutual inductance is of great interest in the characterization and the design of dynamic WPT systems for automotive applications. The objective of this section is to show the use of our algorithm to build consistent predictors of the mutual inductance. This approach is here applied to study the most influential spatial parameters in a dynamic WPT system, given different trajectories of the vehicle during its motion. The test case studied here is to show the interest of using our active learning metamodel process on complex systems with various parameters to perform sensitivity analysis.

4.2.1 The input model

Based on the collaboration developed during the MICEV Project [2] for the metrology around WPT systems for automotive applications, the University of Salerno and the University of Cassino and Southern Lazio provided us an analytical behavioral model to describe the dependence of the mutual inductance on the real trajectory of an electrical vehicle in the case of dynamic WPT charging [99]. The mutual inductance is described as a function of Δy and Δz . The various trajectories are displayed on figure 4.6 with the

reference geometry in the plane (y, z) , where the vehicle trajectory lies. The nominal trajectory is given by the red arrow in figure 4.6, representing the RX coil moving along the y -axis, with no lateral displacement ($\Delta z = 0$). Any other trajectory can be represented by coordinates $(\Delta y, \Delta z)$. Because of the symmetry of the two TX coils, the mutual inductance for a single pair RX-TX is enough to describe the full system. The total mutual inductance of the system can be expressed as:

$$\begin{aligned} M_{tot} &= M_{RX-TX1} + M_{RX-TX2} \\ &= M_{tx1,bhv}(\Delta y, \Delta z) + M_{tx1,bhv}(\Delta y - 2\Delta y_{mid}, \Delta z) \end{aligned} \quad (4.2)$$

where $M_{tx1,bhv}$ is the analytical model for the $RX - TX1$ coil pair, and $2\Delta y_{mid} = 2.104$ m is the longitudinal displacement between the center of the two TX coils. The inductance $M_{tx1,bhv}$ of one pair RX-TX1, expressed in μH , is given by (4.3):

$$M_{tx1,bhv} = p_0 \tanh[p_1(\Delta y^2 + p_2)] + p_3 \operatorname{atan}(|p_4 \Delta y|^{p_5}) + p_6 \quad (4.3)$$

where the coefficients p_i (for $i = 0, \dots, 6$) are:

$$p_i = a_{i0} \operatorname{atan}[a_{i1}(|\Delta z| - a_{i2})] + a_{i3} \quad (4.4)$$

with values of the fitting coefficients listed in Table 4.1.

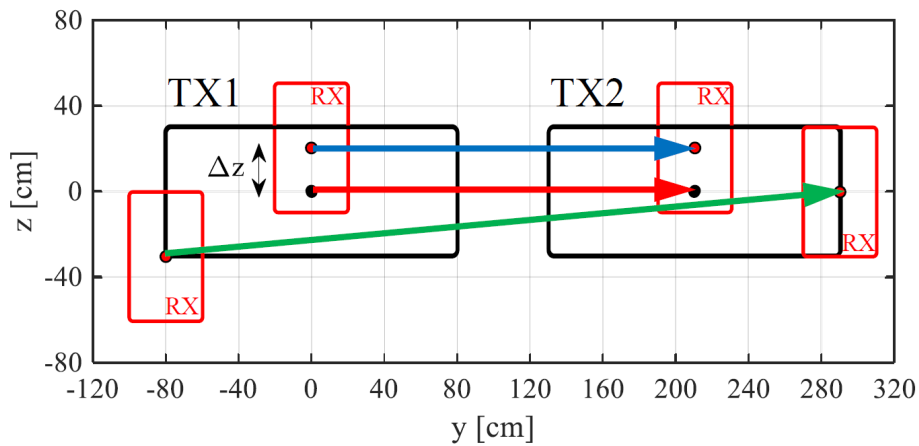


Fig. 4.6 Different trajectories of the RX coil moving along two TX coils. The nominal trajectory is represented by a red arrow.

Table 4.1 Coefficient values for the model given in equations 4.3 and 4.4

coefficient	a_{i0}	a_{i1}	a_{i2}	a_{i3}
p_0	13.3	7.35	0.190	-17.7
p_1	13.6	20.2	0.257	2.93
p_2	$-5.01 \cdot 10^{-2}$	8.40	0.234	-0.484
p_3	9.92	7.32	0.187	-14.0
p_4	0.120	8.46	0.263	-1.50
p_5	1.08	7.28	0.323	-2.73
p_6	-13.2	7.40	0.189	17.9

Training datasets

Two different datasets have been built using this input model, corresponding to various cases:

- the trajectory 1 (blue arrow on figure 4.6) corresponding to a trajectory parallel to the nominal one, with a lateral displacement with 70 datapoints
- the trajectory 2 (green arrow on figure 4.6) corresponding to a trajectory that moves diagonally with respect to the nominal one with 10 datapoints

These two trajectories with their corresponding mutual inductance values are validation sets which will be compared against the results of our algorithm who build a dataset consisting of any trajectory possible for any misalignment of the coils. Indeed, the algorithm sampled various datapoints in the $(\Delta y, \Delta z)$ space to build the metamodel with a *LOO* threshold $\varepsilon = 10^{-3}$ for the meta-domains and the maximum number of division $m = 4$.

4.2.2 Dynamic charging applications with one TX coil

The first goal has been to try out the active learning metamodel on a simpler case of dynamic charging with only one TX coil. The mutual inductance

values for the pair RX-TX1 against the longitudinal displacement Δy and the lateral misalignment Δz is shown in figure 4.7. It can be observed that the mutual inductance is also reaching its maximum in this area. The points sampled by our algorithm are shown in figure 4.8 with a total of $n_{samples} = 207$. The algorithm is showing us expected results for the choice of the sampling datapoints on this real model: a higher number of samples falls into the range $\Delta z \in [-40, 40]\text{cm}$ and $\Delta y \in [-80, 80]\text{cm}$, whereas less samples can be found outside these ranges where it is less needed as the output is almost constant.

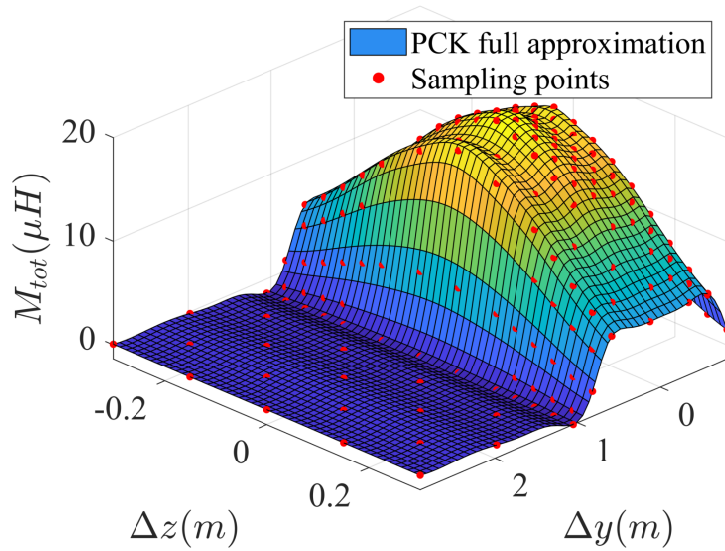


Fig. 4.7 Mutual inductance values for a single pair RX-TX against the longitudinal displacement Δy and the lateral misalignment Δz for any trajectory (with $m = 4$ and $\varepsilon = 10^{-3}$)

Two additional metamodels have been computed for the two validation sets available, all three metamodels have been used to perform a sensitivity analysis whose results are given in table 4.2. First, the three metamodels are extremely consistent with themselves ($LOO < 10^{-5}$), which ensures three independent but accurate sensitivity analysis indices. Then, the three indices are almost giving the same result for the trajectories: the longitudinal displacement Δy is the most relevant parameter. Indeed, the lateral displacement Δz realizes only a minor shift when the vehicle is moving along the charging lane. Therefore, it can be concluded that in all

cases, the longitudinal displacement Δy is the parameter which needs to be the most controllable to prevent any disruption to the dynamic charging device. It can also be observed that both metamodelling based on the validation sets are more consistent than the built-in dataset from our algorithm. It could be explained by the wide range our algorithm is covering in the $(\Delta y, \Delta z)$ plane which implies greater variations of the mutual inductance. This will be discussed later on the two TX coils system in section 4.2.4.

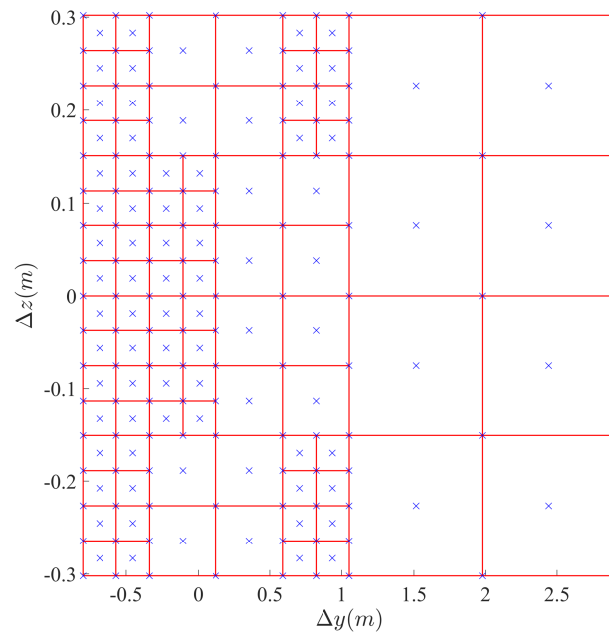


Fig. 4.8 Parameter domains and relevant samples used to build the metamodel for the mutual inductance for a single pair RX-TX against the longitudinal displacement Δy and the lateral misalignment Δz for any trajectory (with $m = 4$ and $\varepsilon = 10^{-3}$)

Table 4.2 Sobol index analysis of the mutual inductance for a single pair RX-TX, against Δy and Δz (with $m = 4$ and $\varepsilon = 10^{-3}$)

Trajectory	Total $S_{\Delta y}$	Total $S_{\Delta z}$	LOO
dataset 1 (parallel trajectory)	0.943	0.132	$7.69 \cdot 10^{-6}$
dataset 2 (diagonal trajectory)	0.935	0.133	$1.26 \cdot 10^{-6}$
dataset 3 (any trajectory)	0.935	0.135	$1.56 \cdot 10^{-5}$

4.2.3 Dynamic charging applications with two TX coils

With successful results on the system with only one TX coil, using the equation 4.2, our algorithm has been expanded to the full system. For two consecutive TX coils, as shown in figure 4.6, the area of interest ranges from the position where the RX coil is on the top of the TX1 coil to that where it is on the top of the TX2 coil, which corresponds to the relevant domain $\mathcal{D} = \{(\Delta z, \Delta y), \Delta z \in [-40, 40]\text{cm}, \Delta y \in [-80, 80] \cup [130, 290]\text{cm}\}$. The area out of interest is the gap between the two TX coils and the borders of the domain. The sampled datapoints ($n_{samples} = 365$) with the estimated total mutual inductance is displayed on figure 4.9.

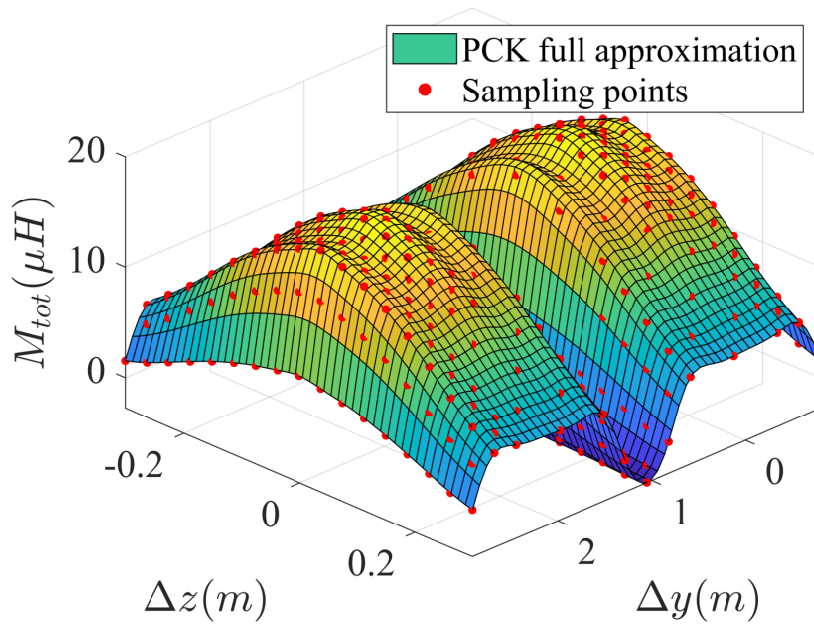


Fig. 4.9 Mutual inductance values for a single RX coil and two TX coils against the longitudinal displacement Δy and the lateral misalignment Δz for any trajectory (with $m = 4$ and $\varepsilon = 10^{-3}$)

As the spacing between the two TX coils is big enough, their areas of effect are not overlapped. As a consequence, the maximum value of the mutual inductance is the same one achieved for the model with only one TX coil in figure 4.7. Thus, as no area of a constant value for the total mutual inductance exists in this case, for any trajectory much more datapoints

are needed to compute a consistent metamodel for this case with two transmitting coils. The needed samples with their corresponding meta-domains are displayed on figure 4.10. As expected by the estimated total mutual inductance, the meta-domains from the system with one coil (figure 4.8) in the range $[-30, 30]\text{cm} \otimes [-80, 110]\text{cm}$ has been symmetrized in the range $[-30, 30]\text{cm} \otimes [110, 290]\text{cm}$ for the full system with two coils.

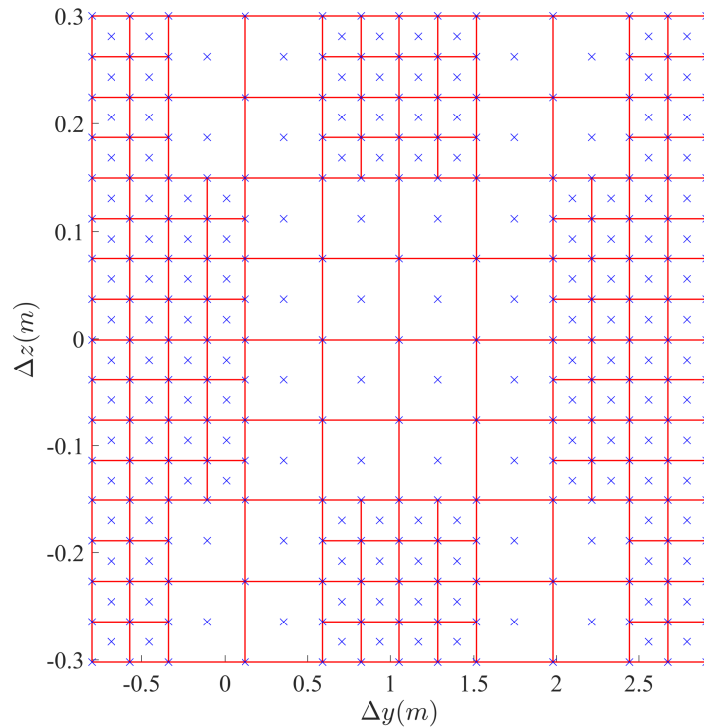


Fig. 4.10 Parameter domains and relevant samples used to build the metamodel for the mutual inductance for a single RX coil and two TX coils against the longitudinal displacement Δy and the lateral misalignment Δz for any trajectory (with $m = 4$ and $\varepsilon = 10^{-3}$)

The three computed metamodels (one for each dataset and one with our algorithm) have been used to perform a sensitivity analysis in the $(\Delta y, \Delta z)$ plane, whose results are given in table 4.3. The three metamodels are still consistent with themselves ($LOO < 10^{-5}$), but the three analysis indices are not giving the same results. For a parallel trajectory, the RX coil is only seeing the effect of the second coil at the end of the trajectory which is not modifying the observed mutual inductance compared to the previous

analysis. Conversely, for a diagonal trajectory and for any other trajectory, the RX coil cannot avoid the effect of the second TX coil. Therefore, the longitudinal displacement is not the most important parameter anymore. This means that a car, moving forward over a series of TX coils but not along a trajectory parallel to the nominal one, realizes a mutual inductance that is now much more dependent on its lateral misalignment. However, given the TX coil dimensions and the motion of the car along the y -axis, the longitudinal displacement remains the most influential parameter ($S_{\Delta y} > S_{\Delta z}$). Yet again, due to the number of samples the metamodel built with our algorithm seems less consistent when observing the LOO .

Table 4.3 Sobol index analysis of total mutual inductance over two TX coils, against Δy and Δz for various trajectories (with $m = 4$ and $\varepsilon = 10^{-3}$)

Trajectory	Total $S_{\Delta y}$	Total $S_{\Delta z}$	LOO
dataset 1 (parallel trajectory)	0.908	0.166	$1.60 \cdot 10^{-6}$
dataset 2 (diagonal trajectory)	0.656	0.375	$1.27 \cdot 10^{-6}$
dataset 3 (any trajectory)	0.684	0.349	$5.34 \cdot 10^{-6}$

4.2.4 Best sensitivity analysis

The active learning metamodeling algorithm built a consistent predictor for the total mutual inductance within the $(\Delta y, \Delta z)$ parameter space. To assess the usefulness of the algorithm, the results from this estimate has been compared to the two other metamodels generated with the two available datasets. The goal is to prove even if the consistency (measured with the LOO) of the metamodel for any trajectory is lower than the other two metamodels, the resulted sensitivity analysis is still more accurate to predict the complete dependency of the system. To find which metamodel is the best at predicting the behavior of the total mutual inductance, we tried to predict the values from the dataset 1 using the values of the dataset 2 and the other way around, while predicting both datasets with the metamodel build with any trajectory. The results from the validation error R^2 given by the different predictors are given in table 4.4.

Table 4.4 Validation errors R^2 on the values from datasets 1 and 2, against the metamodel predictors built with various trajectories.

Metamodel	dataset 1	dataset 2
dataset 1 (parallel trajectory)	1	0.514
dataset 2 (diagonal trajectory)	$6.27 \cdot 10^{-2}$	1
dataset 3 (any trajectory)	0.999	1.00

By evaluating the coefficient R^2 , it can be seen that the first two datasets are only able to predict the total mutual inductance behavior within their own validity range for the parameters values. On the contrary, the third metamodel ensures quite low R^2 values for both datasets, and can predict values of the mutual inductance in a wider range for the input parameters. Moreover, the R^2 given by our metamodel is better on both datasets, which means even on a restricted trajectory, the algorithm produces the best sensitivity analysis overall.

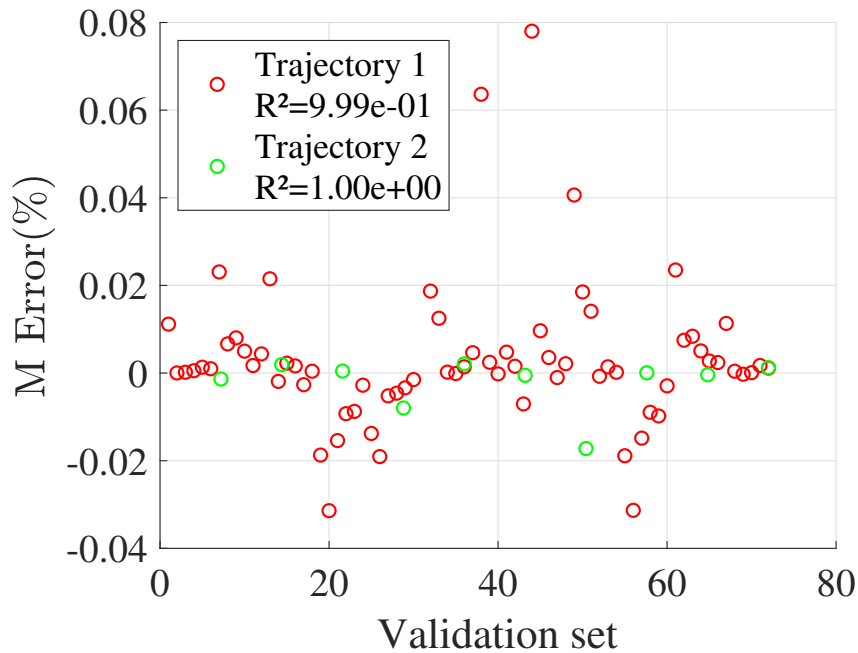


Fig. 4.11 Percentage error of the metamodel predictor build with any trajectory against the values from the dataset 1 and 2 (with $m = 4$ and $\varepsilon = 10^{-3}$)

But as the R^2 is an averaged value of the correlation between the real model and the estimated output model, locally some huge differences

might still subsist. Hence making the use of such a sensitivity analysis impossible. On figure 4.11, the percentage error between the predicted values and the real values given by both validation sets are displayed. Among all datapoints only 3 out of 70 datapoints give a percentage error greater than 4% (but still smaller than 8%) for the first dataset and most of the error values are close to zero. For the second dataset, all 10 percentage error are lower than 2% and again most are close to zero. As expected the metamodel for any trajectory is providing the best metamodel to work with, and its sensitivity analysis is the one to be taken into account.

4.2.5 Discussion on the parameters ε and m

For this first input model, our algorithm has been proven useful for building a consistent predictor for performing an accurate sensitivity analysis. But even if the input model is complex, the gain of computation time by saving a lot of samples could not be properly observed as the input being purely analytical it had been computed easily at almost instant-speed ($n_{samples} = 365$). Moreover, the *LOO* threshold on the meta-domains had been set to $\varepsilon = 10^{-3}$ and the maximum number of division $m = 4$. These two values made our algorithm overkill the sensitivity analysis problem as so many datapoints were computed, resulting in an overly consistent predictor. Thus making our estimate unable to perform an inaccurate sensitivity analysis.

In order to see if an accurate sensitivity analysis could be obtained with a lower number of samples, the active learning metamodeling has been computed again with with $m = 3$ and $\varepsilon = 0.5$. This resulted in a new metamodel for the total mutual inductance with only $n_{samples} = 99$ and $LOO \simeq 8.75 \cdot 10^{-4}$. The resulting estimated total mutual inductance (see figure 4.12) seems still accurate compared to the overly consistent previously computed metamodel (see section 4.2.3). As it can be observed with the corresponding meta-domains and datapoints shown on figure 4.13, the range $\Delta z \in [-15, 15]_{cm}$ needs lesser samples than other areas due to smaller variations of the output model. In the end, 365 datapoints were unnecessary to compute our consistent predictor as the *LOO* still has an excellent value ($\sim 0.09\%$) with this new metamodel, thus still overly consistent.

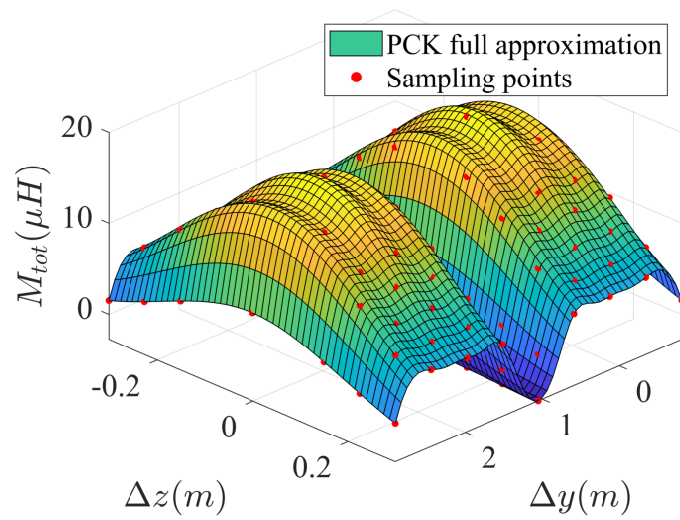


Fig. 4.12 Mutual inductance values for a single RX coil and two TX coils against the longitudinal displacement Δy and the lateral misalignment Δz for any trajectory (with $m = 3$ and $\varepsilon = 0.5$)

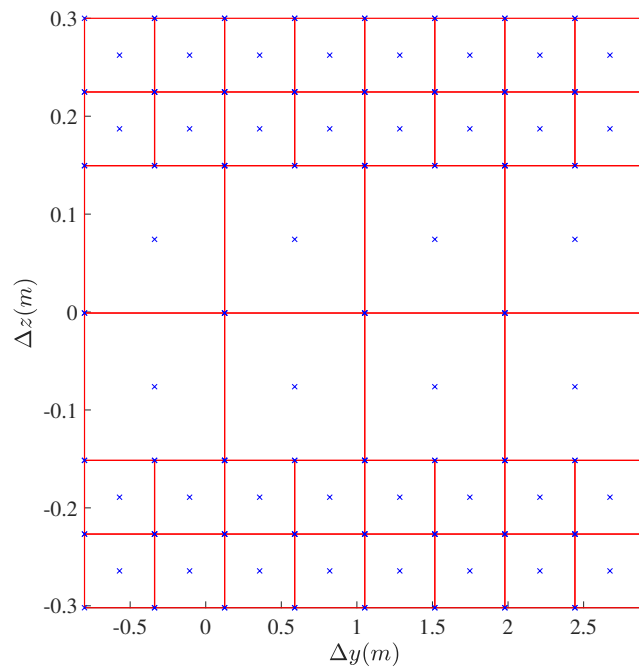


Fig. 4.13 Parameter domains and relevant samples used to build the metamodel for the mutual inductance for a single RX coil and two TX coils against the longitudinal displacement Δy and the lateral misalignment Δz for any trajectory (with $m = 3$ and $\varepsilon = 0.5$)

The sensitivity analysis on this new metamodel is giving us the following values for the total Sobol' indices: $S_{\Delta y} = 0.650$ and $S_{\Delta z} = 0.381$. The analysis is giving us the same trend for the dependency of the total mutual inductance. And by plotting the percentage error on the two validation sets on figure 4.14, it can be observed that again our metamodel is extremely accurate as only 6 datapoints have a percentage error greater than 1% (still lower than 5%) for the first trajectory and none for the second. Both R^2 are close to one by $\sim 0.2\%$ which is more than enough to insure the accuracy of our predictor. Finally, even with greater values for the LOO threshold and for the maximum number of divisions m , the algorithm managed to produce an accurate sensitivity analysis using a consistent predictor. Even if the effect of lateral misalignment between the coil pair on the resulting mutual inductance cannot be totally neglected for the design of WPT systems, the longitudinal displacement remains the most influential parameter in dynamic charging applications, which has to be taken into account in WPT systems analysis and design.

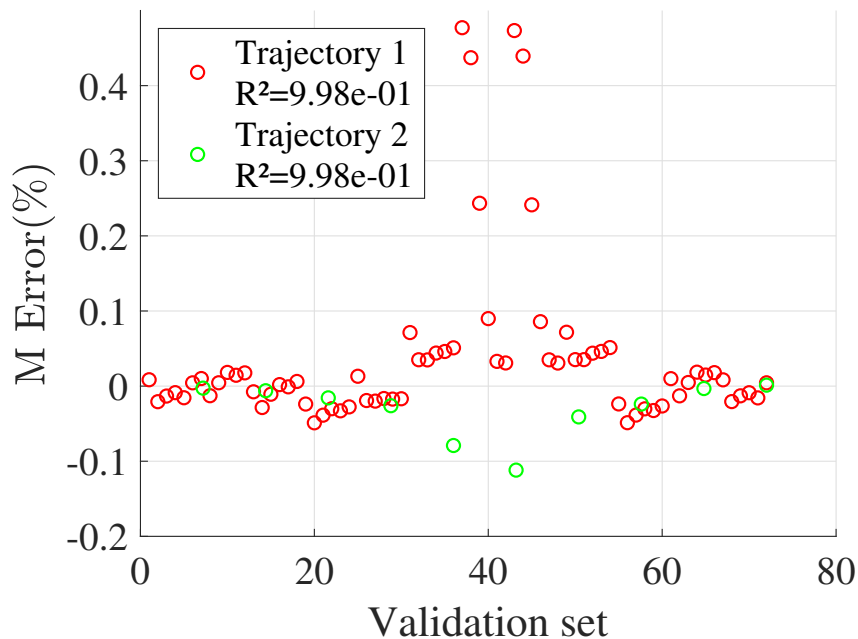


Fig. 4.14 Percentage error of the metamodel predictor build with any trajectory against the values from the dataset 1 and 2 (with $m = 3$ and $\varepsilon = 0.5$)

4.2.6 Higher input dimensions

One of the issues raised when building the algorithm with the quad-tree based uniform sampling has been the case of big dimensions for the input domain. So far the algorithm has only been tested on input domains with dimension $d = 2$. Using the available GP algorithm from [99], the WPT system has been explored on a static case with the transmitting and receiving coils centered and aligned for the nominal position. The three considered parameters are now: Δx the vertical gap between the two coils, Δz the radial displacement whose effect is similar to Δy (the longitudinal displacement) for the static case and α the rotation of the RX coil around the x-axis. The system with some relevant parameters is displayed on figure 4.15 in the (y, z) plane. The algorithm has been run with $\varepsilon = 0.3$ and $m = 3$ as already proven successful in section 4.2.5.

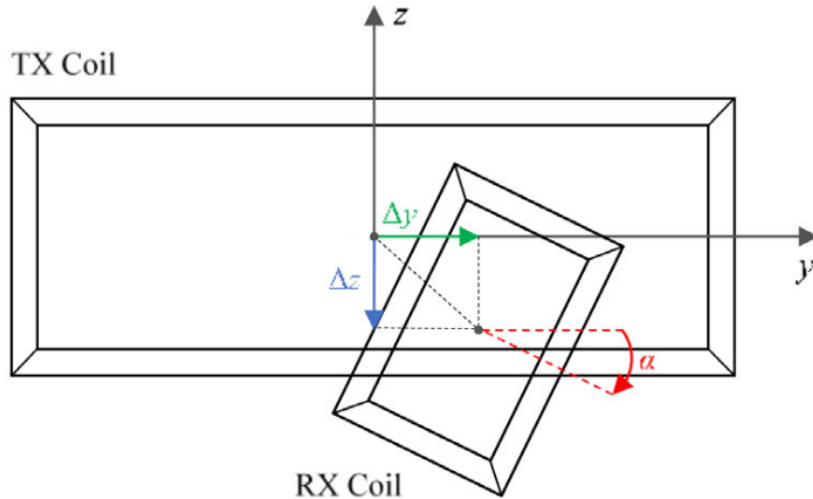


Fig. 4.15 Reciprocal position of the two coils given by the coordinates $(\Delta x, \Delta y, \Delta z)$ of the RX coil center with respect to the TX coil center point, and a by rotation angle α , taken from [100]

Table 4.5 80 coils misalignment conditions (validation dataset T)

parameter	values
Δx (cm)	{15, 20, 25, 30}
Δz (cm)	{0, 10, 15, 25}
α ($^\circ$)	{0, 10, 20, 30, 40}

In order to assess the accuracy of our predictor, the dataset displayed on table 4.5 has been used as a validation set for our predictor. Using the provided input GP model, the algorithm managed to build a consistent PCK metamodel predictor for the mutual inductance behavioral model in a static case with $n_{samples} = 86$. The considered metamodel has an excellent consistency $LOO = 2.55 \cdot 10^{-3}$ and is able to almost perfectly predict the input model. The correlation between the training dataset and the predictor from the resulting metamodel is $R^2 = 9.98 \cdot 10^{-2}$.

For observing the correlation in this three-dimensional input space, the validation set has been sorted first in the ascending order of α , then in the ascending order of Δx and, finally, of Δz , giving us 80 different samples displayed on figure 4.16. Out of the 80 datapoints, only 4 are remarkably different between the input model and the metamodel. But by looking at the percentage error (figure 4.17), the corresponding percentage errors are ranging no greater than 5% with most of the remaining 76 datapoints having an error smaller than 1%. Our predictor is indeed accurate enough to predict the behavior of the mutual inductance input model and can thus be used to perform a sensitivity analysis. The Sobol' analysis performed on the resulting metamodel is displayed in table 4.6. As expected the vertical gap between the two coils (along the x-axis) is the relevant parameter regarding the rotation around the x-axis and the lateral displacement along the z-axis. However these two parameters have greater enough Sobol' indices value for not being neglected regarding the gap.

Table 4.6 Sobol analysis of the mutual inductance of 2 coils against the vertical distance Δx , the lateral misalignment Δz and the rotation α of the RX coil around the x-axis

Total $S_{\Delta x}$	Total $S_{\Delta z}$	Total S_{α}	LOO
0.678	0.195	0.280	$2.155 \cdot 10^{-5}$

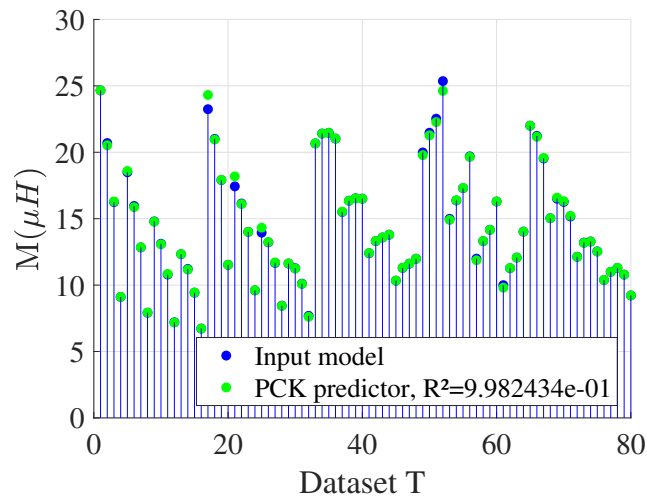


Fig. 4.16 Mutual inductance values from the GP input model (blue) and the predictor (green) for the Dataset T

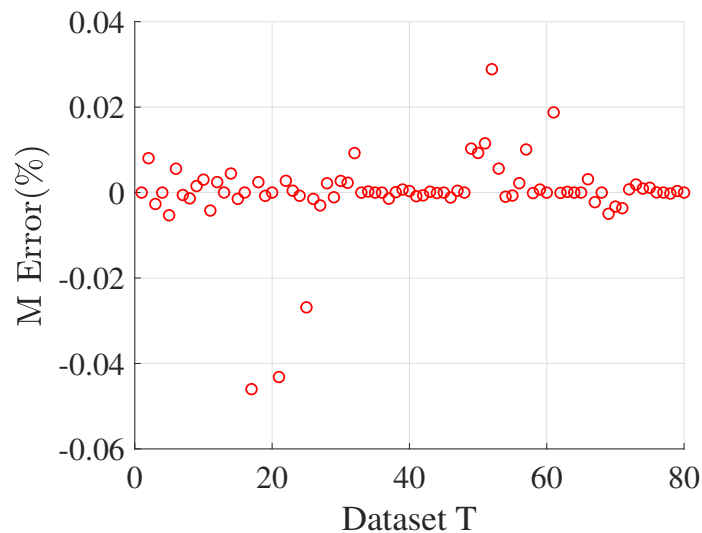


Fig. 4.17 Percentage error of the metamodel predictor against the GP model value

4.2.7 Performance

Finally, our algorithm managed to compute at a low computation cost a consistent predictor for an higher dimensional input model with even less datapoints as the bidimensional case. The resulting sensitivity analysis has been proven accurate using validation sets for both cases and can be useful for future designs of dynamic and static WPT systems.

Using equation 4.1, the maximum number of datapoints for the meta-model in section 4.2.5 ($m = 3, d = 2$) is $n_{max} = 145$ and only 99 were needed by the algorithm. While in the metamodel computed in section 4.2.6 ($m = 3, d = 3$), $n_{max} = 1241$ and only 86 were needed. The a priori limitations of the algorithm were that it would be useless for higher dimensions as the number of meta-domains explored and therefore the number of new samples would greatly increase. Based on the use of only one metamodel the a posteriori observation is the complete contrary. Thus, the algorithm needs to be tried out on more complex models with higher input dimensions to confirm or infirm its performance.

The GP behavioral model used here to experiment the performance of our active learning algorithm has been provided with no given accuracy or consistency. Thus, its only use for trying our metamodelling processes is as if it was the realization of a complex computational model or some experimental results. Moreover, the gain in using our algorithm here is negligible as the input model is already an analytical expression, thus easy to compute at instant speed, its use has been successfully demonstrated for various parameters. Hence why in the following section 4.3, our algorithm is applied to a complex FEM model (much longer to compute) with many input parameters possible to try it out.

4.3 Multi-parameter predictor for a complex WPT charger model

An algorithm combining subgridding techniques and metamodelling has been successfully developed and tested on both simple functions and complex analytical models (bidimensional and three-dimensional cases). As our first observations for metamodelling had been made on a simplified FEM model (see section 3.2) issued from the available system at Politecnico di Torino developed in Vincenzo Ciremele PhD's thesis [85]. The goal here has been to apply our algorithm on the complete WPT system from Politecnico di Torino reproduced with COMSOL. Based on this much more complex model our algorithm tries to build a consistent predictor that can

be used for both sensitivity analysis but also for other processes (see section 4.4) in lieu and place of the real model to save computation time.

4.3.1 Modelling a realistic WPT model

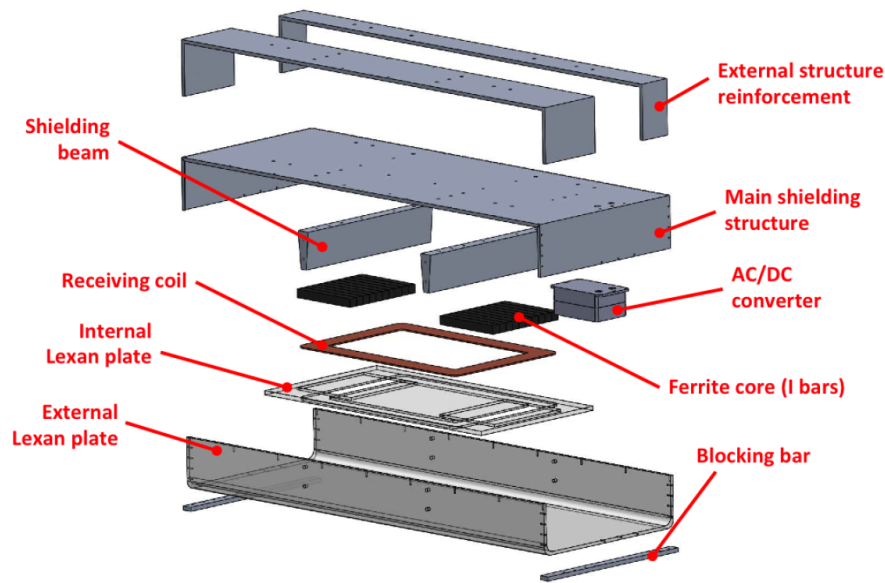


Fig. 4.18 CAD model of the main components of the receiver structure from [85]

Using the CAD model from the WPT system receiver used for experiments at PoliTO (decomposed on figure 4.18), the complete WPT model has been reproduced with COMSOL. For the receiving device, only the main shielding structure optimized with the shielding beams, along with the double U-shaped coils (displayed in orange on figure 4.19) topped by the 3F3 ferrite cores has been considered. While only the transmitting coil in the ground has been modeled for the transmitter. This 3D FEM model is displayed on figure 4.19.

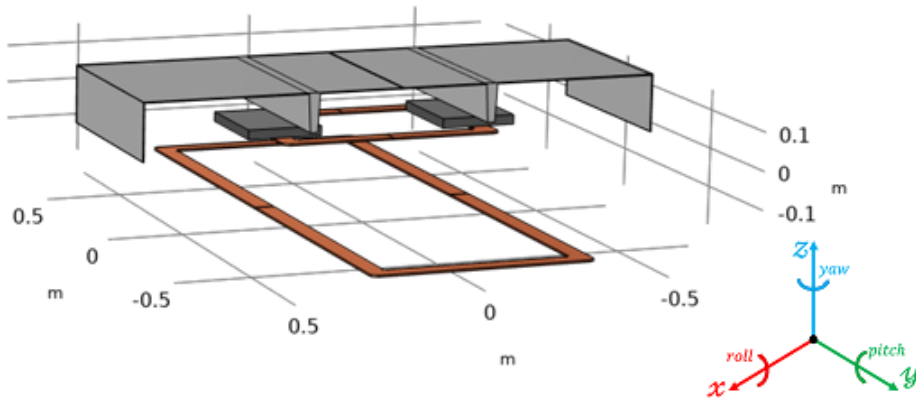


Fig. 4.19 COMSOL model for the complete PoliTO model with 3F3 ferrites cores and an optimized shielding structure

Because this model is fitting a real model available inside the laboratory, the effects of some parameters such as the shield conductivity (or relative permeability) studied on the first COMSOL model (see section 3) have not been considered. It would be hard to easily modify on a real model the shield conductivity of such a system. Therefore the various considered parameters are mostly design-based with notably:

- the dimensions and number of turns of both coils
- the misalignment in translation and rotation between both coils
- the ferrite cores geometrical and physical parameters

These parameters are fully described in table 4.7. Only one ferrite core is parameterized as the other is obtain by symmetrizing along the receiving coil width.

4.3.2 Consistent predictor and sensitivity analysis

Sensitivity to the car movement

A first and straightforward application has been to try to compute a consistent predictor for the behavior of the coupling factor regarding the movement of the vehicle and the road profile. The considered parameters

Table 4.7 Relevant parameters tunable in the complete COMSOL model (the system coordinates are specified on figure 4.19)

variable	nominal value	unit	description
w_{rcoil}	0.5	m	receiving coil width
l_{rcoil}	0.3	m	receiving coil length
N_{re}	10	-	number of turns in receiving coil
w_{tcoil}	0.5	m	transmitting coil width
l_{tcoil}	0.5	m	transmitting coil length
N_{tr}	10	-	number of turns in transmitting coil
α	0	°	yaw of the transmitting coil
β	0	°	pitch of the transmitting coil
γ	0	°	roll of the transmitting coil
Δx	0	m	misalignment along the x-axis
Δy	0	m	misalignment along the y-axis
Δz	0.2	m	misalignment along the z-axis
w_f	0.2	m	ferrite core width
h_f	0.025	m	ferrite core height
l_f	0.25	m	ferrite core length
$x_f(\Delta x = 0)$	0.26	m	x position of the ferrite center
$y_f(\Delta y = 0)$	0	m	y position of the ferrite center
z_f	0.235	m	z position of the ferrite center
μ_{rf}	2000	-	relative permeability of the ferrite core

for this analysis are displayed in table 4.8. The Δx misalignment and the yaw α have been chosen to consider a car slightly deviating from the center of the road, while the Δy misalignment embodies the direction of motion.

The Δz misalignment along with the pitch β and the roll γ take into account the road profile.

The active learning metamodel algorithm managed to build a consistent predictor with $\varepsilon = 0.3$ and $m = 3$. The resulting metamodel uses $n_{samples} = 65$ and has a consistency of $LOO \simeq 3.002 \cdot 10^{-2}$. An example of the values produced by the active learning metamodel predictor is displayed on figure 4.20 for the variations of Δz and γ (a modification of the road profile) with the other parameters set at their nominal values ($\Delta x = \Delta y = 0$ m and $\alpha = \beta = 0^\circ$).

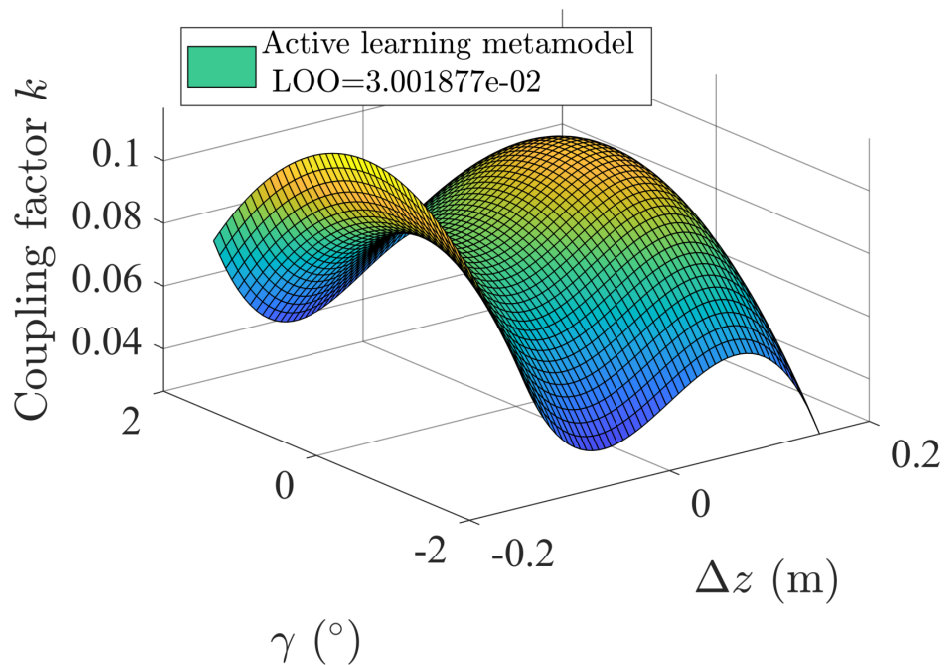


Fig. 4.20 Variations of the coupling factor k against the z misalignment Δz and the roll γ ($\Delta x = \Delta y = 0$ m and $\alpha = \beta = 0^\circ$)

Table 4.8 Parameters with their corresponding ranges for the analysis of a dynamic WPT system ($LOO \simeq 3.002 \cdot 10^{-2}$, $n_{samples} = 65$)

variable	min	max	description	S^T
Δx	-0.25 m	0.25 m	x misalignment	0.139
Δy	-0.5 m	0.5 m	y misalignment	0.138
Δz	-0.15 m	0.15 m	z misalignment	0.261
α	-10°	10°	yaw	0.136
β	-2°	2°	pitch	$1.973 \cdot 10^{-3}$
γ	-2°	2°	roll	0.634

Using this consistent predictor, the sensitivity analysis has been computed and is displayed on table 4.8. The most important parameters are the roll γ along with the Δz misalignment. As expected these two parameters greatly increase the distance between the two coils, which decrease significantly the coupling factor. Even if the pitch β also influences the gap between the receiver and the transmitter, for this small range $[-2^\circ, 2^\circ]$ corresponding to an imperceptible bump on the road, its effect is entirely negligible. The roll embodies a non-flatten road which has still a greater impact with such a small range. The other three parameters Δx , Δy and α are taking into account the dynamic aspect for the WPT and are of course not negligible.

Thus, for the building of future roads for dynamic WPT, a great care should be taken when flattening it. For the design of the car itself, the trajectory control is as expected crucial to maximize the effectiveness of the charging device. This analysis also confirms the need to automatically stop the charging if the driver gets too far from the center of the charging lane.

Sensitivity to various coil dimensions

Another interesting analysis is to assess the dependency of the coupling factor regarding the transmitter or receiver dimensions. This could emphasize where the greatest care should be taken when designing or building a new WPT system. The considered parameters with their ranges and Sobol' indices are displayed in table 4.9. The algorithm has been ran with

$\varepsilon = 0.3$ and $m = 3$ resulting in a metamodel with $LOO \simeq 1.410 \cdot 10^{-2}$ and $n_{samples} = 17$.

Table 4.9 Parameters with their corresponding ranges for the analysis of a dynamic WPT system ($LOO \simeq 1.410 \cdot 10^{-2}$, $n_{samples} = 17$)

variable	min	max	description	S ^T
w_{rcoil}	0.3 m	0.6 m	receiving coil width	0.105
l_{rcoil}	0.3 m	0.6 m	receiving coil length	0.177
w_{tcoil}	0.3 m	0.6 m	transmitting coil width	0.0614
l_{tcoil}	0.5 m	2 m	transmitting coil length	0.691

The length of the transmitting coil is by far the most important parameter regarding the coupling factor behavior. It ensures the totality of the Magnetic Flux generated is embraced by the receiving coil. Due to the chosen possible dimensions, for the same reason the length of the receiver is also extremely important. As the nominal gap between the coils is $\Delta z = 23.5$ cm, the width of the transmitter has a lesser influence as long as the totality of the Magnetic Flux can be directed to the receiver which is insured with a range $[0.3 \text{ m}, 0.6 \text{ m}]$ similar to the maximum dimensions of the receiver. The receiver dimensions are only limited by the car it can be put in and therefore cannot be extended.

Discussion

These two analysis have been performed to show the usefulness of the active learning metamodel algorithm on a complex and realistic model predictor. The results can be used for future designs and building of WPT systems for automotive applications.

Even if the two computed metamodels have a great consistency ($LOO < 3\%$), it can be seen that with higher input dimensions the number of

computed samples tends to explode. If one were to diminish the consistency threshold ε to less than 1% for example, the metamodel for the coil dimensions ($m = 3, d = 4$) would need at the maximum $n_{max} = 10657$ (see equation 4.1), while $n_{max} = 793585$ for the WPT dynamic analysis ($m = 3, d = 6$). Thus, the computation of a metamodel with higher consistency would be almost impossible as one datapoint takes ~ 1 min to compute if the resulting sub-metamodels are not consistent.

With such a complex model, much different than regular analytical functions to predict, a great drop of consistency can also be observed. Indeed, for the GP mutual inductance model (see section 4.2.3), the resulting consistencies are extremely low ($LOO < 10^{-3}$), while the various metamodels computed on this WPT model failed to reach similar consistency. Moreover, for both computed metamodels, the datapoints chosen by the algorithm are simply the corners of the input space (the first datapoints of the quad-tree subgridding algorithm). Even if the resulting metamodel is consistent enough, some parts of the input space are completely unexplored and the resulting metamodel could be consistent but not accurate.

Therefore, the algorithm shows its limitations for complex FEM model and high dimension input space. An easy solution to this problem is to decrease the number of input parameters. Using a maximum number of division of $m = 3$ with $d = 3$ parameters instead of $d = 5$ makes the maximum number of samples drop from $n_{max} = 91817$ to $n_{max} = 1241$, thus reducing by almost 99% the maximum computation time. A first wide analysis can be performed on various parameters, giving us a consistent predictor for the model able to perform an accurate sensitivity analysis. Using this sensitivity analysis, the relevant parameters can be extracted and a finer input space can be chosen with the negligible parameters ignored. Then a better and more consistent metamodel can be built on this smaller set of parameters as it will be able to fully explore the input parameter space thanks to its smaller dimension (see section 4.4.3 for example).

4.4 Multi-objective ferrites optimisation

As previously seen in section 4.3.2, a consistent metamodel for a complex WPT system can be computed at a low computation cost with some limitations. Using the corresponding predictor, many evaluations of this estimate can be performed and used for solving an optimisation problem. This approach has been formalized in the case of RSM for stochastic optimization [101]. For our metamodeling processes, in the field of electromagnetics, many Kriging-based optimization [102] or PCE-based optimization [103] have been recently developed. The goal in this section has been to investigate new configurations for an existing WPT system, especially the design of 3F3 ferrite cores on the available WPT model (see figure 4.19) which had not been done before. The gradient-based optimisation presented here consists in extracting the gradient of the cost function directly from its analytical expression. Indeed, instead of calling the PCK predictor during the optimisation process, the gradient is directly computed from the meta-parameters, thus, saving a lot of computation time in the case of complex high-dimensional models. This method has already been successfully developed for solving inverse problem for eddy-current testing configuration [104].

4.4.1 Optimisation method

Gradient computation

The main advantage of using a PCE-based metamodel is the direct analytical expression (equation 3.13) which allows an easy computation of its gradient [105]. Let P_n be the Legendre polynomial of degree n used as the polynomial basis for our metamodel, $\forall x \in [0, 1]$:

$$(n + 1)P_{n+1}(x) = (2n + 1)xP_n(x) - nP_{n-1}(x) \quad (4.5)$$

$$(1 - x^2)\frac{d}{dx}P_n(x) = -nP_n(x) + nP_{n-1}(x) \quad (4.6)$$

with the unidimensional input domain rescaled to the unit interval. These computations can be extended to other polynomial families (table 3.2) with

various recurrence relations [106, chapter 22]. By combining equations 4.5 and 4.6, the following differential equation is obtained:

$$\frac{d}{dx}P_{n+1}(x) = (n+1)P_n(x) + x\frac{d}{dx}P_n(x) \quad (4.7)$$

Using the equation 4.7 for the derivative from the unidimensional polynomials, the partial derivative for the multi-dimensional polynomials can be computed with the tensor product:

$$\frac{\partial}{\partial x_i}\psi_{\alpha}(\mathbf{x}) = \frac{d}{dx_i}\phi_{\alpha_i}^i(x_i) \bigotimes_{\substack{j=1 \\ j \neq i}}^d \phi_{\alpha_j}^j(x_j) \quad (4.8)$$

By linearity the partial derivatives of the metamodel $\widehat{\mathcal{M}}$ can be computed as:

$$\frac{\partial}{\partial x_i}\widehat{\mathcal{M}}(\mathbf{x}) = \sum_{\alpha \in \mathcal{A}} y_{\alpha} \frac{\partial}{\partial x_i}\psi_{\alpha}(\mathbf{x}) \quad (4.9)$$

with $\mathcal{A} \in \mathbb{N}^d$ the set of multi-indices for the metamodel. The resulting gradient vector is:

$$\nabla \widehat{\mathcal{M}}(\mathbf{x}) = \left(\frac{\partial}{\partial x_1}\widehat{\mathcal{M}}(\mathbf{x}), \dots, \frac{\partial}{\partial x_d}\widehat{\mathcal{M}}(\mathbf{x}) \right) \quad (4.10)$$

Gradient Particle Swarm Optimisation

Based on the well-known Particle Swarm Optimisation (PSO) algorithm [107], the Gradient Particle Swarm Optimisation (GPSO) adds a local gradient-based optimisation on top of the global PSO optimisation [108].

In the PSO algorithm, a group of particles is considered within the parameter space. At each iteration of the algorithm, every particle is moving with its direction of motion depending on its best known position \mathbf{P} and the best known position for its group \mathbf{S} . The metric to compare distances between particles is noted \mathcal{E} and is in our case the resulting predictor from the active learning metamodelling algorithm (see section 4.1.2). With GPSO a gradient-based $\nabla \mathcal{E}$ modifier is added to the usual equations of motion,

the motion of particle k (position \mathbf{x}_k) at the step i is:

$$\mathbf{v}_{k,i} = c_0 \mathbf{v}_{k,i-1} + c_p \text{rand}(0, 1)(\mathbf{P}_k - \mathbf{X}_k) + c_s \text{rand}(0, 1)(\mathbf{S}_{k,i} - \mathbf{X}_k) - c_g \eta \nabla \mathcal{E}(\mathbf{X}_k) \quad (4.11)$$

where c_0 is the inertia weight, c_p is the cognitive coefficient to the best position \mathbf{P}_k , c_s is the social coefficient to the best social position $\mathbf{S}_{k,i}$. The function $\text{rand}(0, 1)$ draws a random number between 0 and 1. The weight of the gradient optimisation is noted c_g with η the step size of the gradient descent $\nabla \mathcal{E}$. The gradient of the cost function is computed using the PC metamodelling approximation (see equation 4.10).

Discussions

The swarm consists of 100 particles and the social group consists of 3 informants. The subset topology has been built such as at every iteration, 3 random particles are drawn from the swarm making the social group. Using this social group instead of picking for example the n – nearest neighbors prevents the algorithm from being stuck in a local extremum. Keeping a low number of informants also prevents the swarm from agglomerating.

The optimisation stops when one of the following criteria is met:

- the accuracy on the minimum for the cost function \mathcal{E} is enough
- a maximum number of iterations, in case of an algorithm divergence
- a maximum convergence speed to prevent premature convergence of the algorithm

4.4.2 Optimisation problem

Using the combination of our active learning metamodelling algorithm with the aforementioned GPSO optimisation method (section 4.4.1) could make optimisation problem on complex models extremely fast. Hence why a problem never treated before on such a WPT system (see figure 4.19) has been chosen to try out the optimisation method: the design of the 3F3 ferrites of the system. The relevant parameters are displayed on figure

4.21 with their variation ranges on table 4.10: the position of the center of the ferrite $O_F(x_f, y_f, z_f)$ along with the ferrite dimensions (w_f, h_f, l_f) . The relative permeability μ_{rf} has been set to its nominal value of 2000 along with the gap value: $\Delta z = 20\text{cm}$. Both ferrites are taken symmetrical regarding (O_R, y, z) . Thus, only the coordinates for one center $O_F(x_f, y_f, z_f)$ are taken into account in the optimisation problem. The remaining parameters of the WPT system model had already been optimized by Vincenzo Cirimele during his PhD [85].

The objectives of the geometry optimisation are to:

- Maximize: $k = \frac{M}{\sqrt{L_R L_T}}$ the coupling factor between the transmitting coil (self-inductance L_T) and the receiving coil (self-inductance L_R) with M the mutual inductance
- Minimize: $V = w_f \cdot h_f \cdot l_f$ the ferrite volume used in the design

Table 4.10 Parameters ranges for the model displayed on figure 4.21

variable	min	max	description
w_f	0.05 m	0.25 m	ferrite width
h_f	0.01 m	0.035 m	ferrite height
l_f	0.1 m	0.5 m	ferrite length
Δx	-0.25 m	0.25 m	x misalignment
Δy	-0.5 m	0.5 m	y misalignment
$x_f(\Delta x = 0)$	0.125 m	0.375 m	x position of the ferrite center
$y_f(\Delta y = 0)$	-0.3 m	0.3 m	y position of the ferrite center

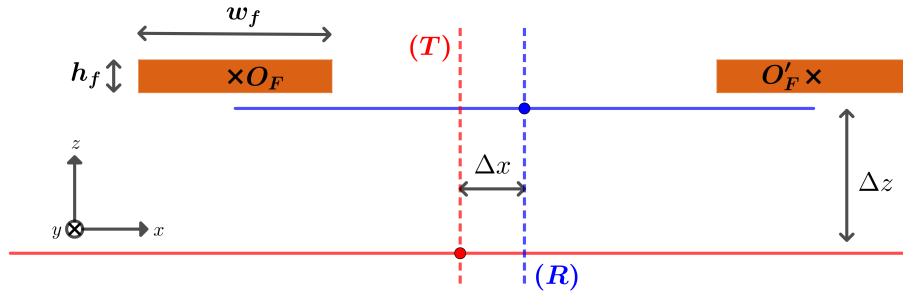


Fig. 4.21 Relevant geometrical parameters in the plane (x, z) for the optimisation problem on the COMSOL model displayed on figure 4.19

The charger is taken in a central position for the various optimisation problems: $\Delta x = \Delta y = 0$. Once a set of optimal parameters $(w_f, h_f, l_f, x_f, y_f)$ has been found for both minimizing V and maximizing k , the model will be validated with the optimized parameters to insure $k(\Delta x, \Delta y) > k_0(\Delta x, \Delta y)$ for the respective variation domains of Δx and Δy , with k_0 being the coupling factor for the nominal values.

4.4.3 Results

Single-Objective Optimisation

The GPSO algorithm has first been tried for a single-objective optimisation on the five parameters $(w_f, h_f, l_f, x_f, y_f)$ within their variation ranges (see table 4.10). With the five-parameters input space, the active learning metamodel has been run with $\varepsilon = 0.3$ and $m = 3$ on the WPT COMSOL model with the output being the coupling factor k . Then this metamodel has been used for the optimisation algorithm with the objective set to maximize k , hence minimizing $1 - k$ in the GPSO. The optimized geometry is displayed on figure 4.22. The optimized values of the five parameters along with their corresponding Sobol' indices are displayed on table 4.11.

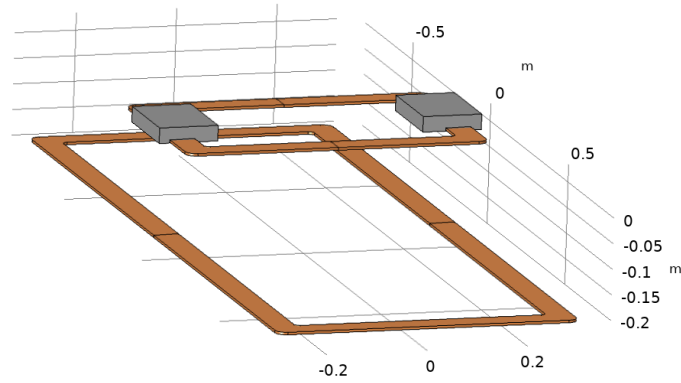


Fig. 4.22 Optimised geometry for the 3F3 ferrites cores for the complete PoliTO WPT model for maximizing the coupling factor k

Table 4.11 Optimized parameters for maximizing the coupling factor k with their Sobol' indices ($LOO \simeq 6.907 \cdot 10^{-10}$, $n_{samples} = 517$)

variable	value	S^T	description
w_f	0.1167 m	$5.856 \cdot 10^{-5}$	ferrite width
h_f	0.0304 m	$7.004 \cdot 10^{-5}$	ferrite height
l_f	0.1760 m	$7.727 \cdot 10^{-5}$	ferrite length
$x_f(\Delta x = 0)$	0.2627 m	0.881	x position of the ferrite center
$y_f(\Delta y = 0)$	-0.0049 m	0.161	y position of the ferrite center

As our GPSO algorithm is semi-stochastic, the optimisation has been run 100 times and the final displayed results have been averaged. Our active learning metamodel has been able to successfully compute a consistent predictor with $n_{samples} = 517$ with an overly low consistency $LOO \simeq 6.907 \cdot 10^{-10}$. The resulting optimised value for the coupling factor is $k = 0.0893$ (with $k_0 = 0.0890$ the nominal value) which represents a minor gain of only 0.3%.

The optimized values for both x_f and y_f are as expected close to the nominal values of the real system. But w_f , h_f and l_f have extremely different values from nominal ones. Indeed, when looking at the total Sobol' indices S^T , it can be seen that the effects of these three parameters is almost negligible on the coupling factor k regarding the position (x_f, y_f) of the center of the ferrite core.

As the results on the size parameters are not reliable when computed with the ferrite core position, the two analysis need to be performed separately for complete results. Thus for future analysis the position of the ferrite core has been set to its nominal one ($x_f = 0.26$ m, $y_f = 0$ m) while only the size parameters (w_f, h_f, l_f) will be varying and optimized.

Multi-Objective Optimisation

For the multi-objective optimisation on the size parameters (w_f, h_f, l_f) for the ferrite cores, another metamodel has been built with the active learning metamodeling algorithm with $\varepsilon = 0.3$ and $m = 3$ on the WPT COMSOL model with the output being again the coupling factor k . The two objectives are to minimize both $1 - k$ and the ferrite volume V . The Pareto front (a set of non-dominated solutions of the optimization problem) is displayed on figure 4.23. Due to the convexity of the Pareto front, the knee point which minimises the distance to the ideal point $(0, 0)$ for both objectives is chosen as our solution for the multi-objective optimization problem.

Table 4.12 Optimized parameters for maximizing the coupling factor k and minimizing the ferrite volume V with their Sobol' indices ($LOO \simeq 3.698 \cdot 10^{-5}$, $n_{samples} = 35$)

variable	value	S ^T	description
w_f	0.246 m	0.876	ferrite width
h_f	0.0102 m	$8.855 \cdot 10^{-3}$	ferrite height
l_f	0.234 m	0.126	ferrite length

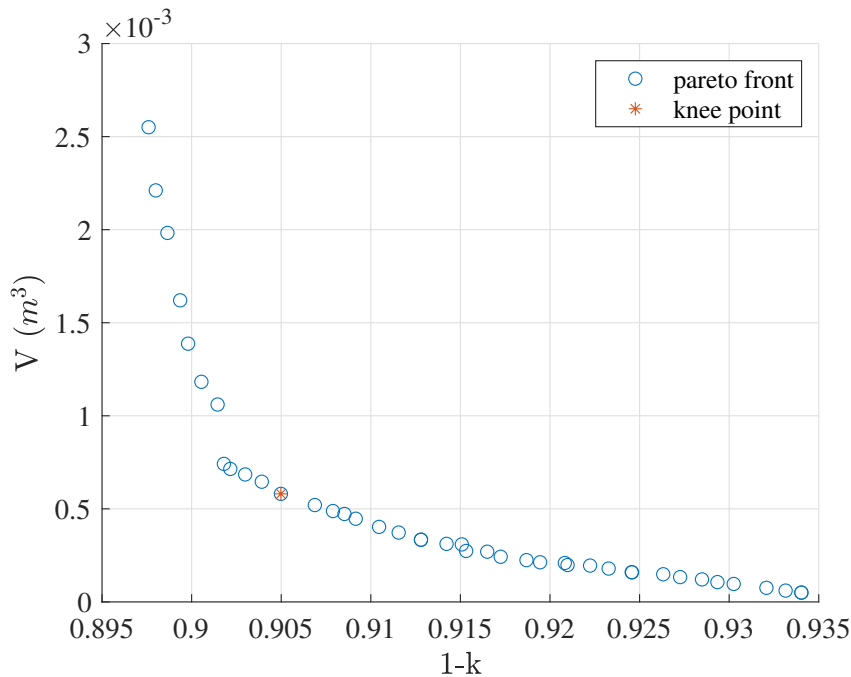


Fig. 4.23 Pareto front for the multi-objective optimisation to minimize the ferrite volume V and maximize the coupling factor k

Depending on the wanted trade-off or the application, other solutions can be chosen among the Pareto front set. The knee point solution is the point ($k = 0.0950$, $V = 5.806 \cdot 10^{-4} m^3$, drawn in red on figure 4.23) which corresponds to the size parameter values displayed on table 4.12. Unlike the previous analysis (see section 4.4.3), when looking at the total Sobol' indices (table 4.12), the effects of the three parameters are not negligible between each others. The most important parameters are the width and length of the ferrite while its height is the least influential on the coupling factor.

When looking at the resulting ferrite geometry (figure 4.24), it can be seen that a ferrite core much thinner while being slightly wider and shorter suffice to maximize the coupling factor while greatly diminishing the ferrite volume compared to the nominal values (see geometry on figure 4.19). For the nominal values the resulting coupling factor is $k = 0.0896$ for a ferrite $V = 1.250 \cdot 10^{-3} m^3$. Therefore for this optimal geometry, the gain of coupling factor is almost 6% while the ferrite volume has been divided by more than 2 (and thus the building cost).

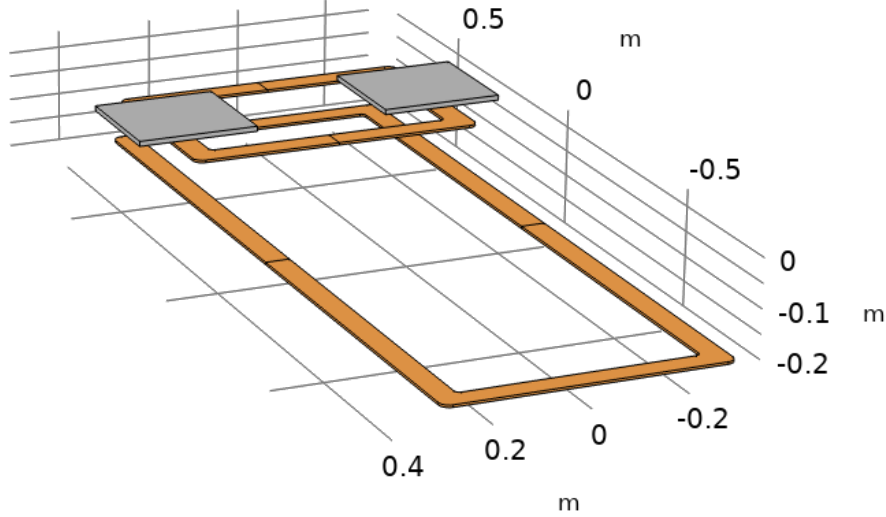


Fig. 4.24 Chosen optimised geometry (arbitrary coil misalignments) for the 3F3 ferrites cores for the complete PoliTO WPT model for maximizing the coupling factor k and minimizing the ferrite volume V

Validation

This optimisation has been conducted with the charger in a central position with both coil centers aligned. The goal has been to validate these results with the optimal parameters set to insure a gain of coupling factor $k(\Delta x, \Delta y)$ for a wide range of possible misalignments regarding the nominal coupling factor $k_0(\Delta x, \Delta y)$. The optimized coupling factor has been computed using the active learning metamodel algorithm with $\varepsilon = 0.3$ and $m = 3$ ($LOO \simeq 2.237 \cdot 10^{-4}$, $n_{samples} = 13$), with $(\Delta x, \Delta y) \in [-0.25\text{m}, 0.25\text{m}] \otimes [-0.5\text{m}, 0.5\text{m}]$. The coupling factor k_0 with the nominal parameter values has been computed similarly ($LOO \simeq 1.588 \cdot 10^{-4}$, $n_{samples} = 13$).

The gain in percentage $\left(\frac{k - k_0}{k_0}\right)$ from the nominal coupling factor is displayed on figure 4.25. Over the wide domains of variations of Δx and Δy the percentage gain is ranging from 2% to 8% with an average value of 6.1%. Thanks to the optimisation, the cost of 3F3 ferrites can be divided by 2 on a

practical system using the optimal set of parameters, while not diminishing, but slightly increasing the WPT coupling factor for the PoliTO model.

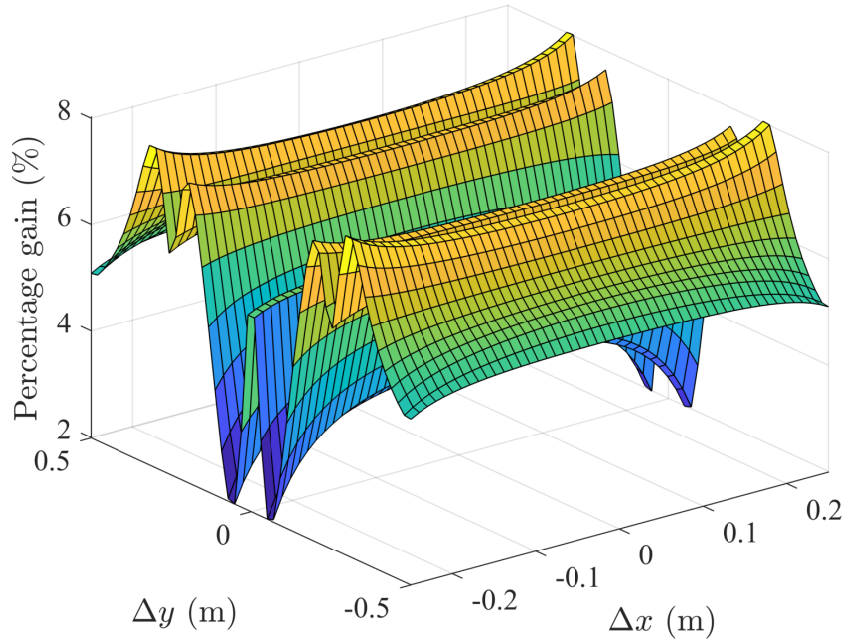


Fig. 4.25 Percentage gain for the coupling factor k with the optimized geometry from the coupling factor with the nominal geometry k_0 against the misalignments Δx and Δy

4.5 Conclusions

Based on preliminary observations on both simple and complex WPT models (see chapter 3), metamodelling has been proven quite useful at interpolating a costly computational model behavior and thus at performing sensitivity analysis or building a consistent predictor at a low computation cost. Using existing datasets, some random samples have been drawn and used as input samples to build various PCK metamodelling processes. This leads to the obvious need to study sampling strategies for our metamodelling processes. Although many space-filling strategies have been developed for surrogate models experimental design [109], such simple static strategies are not suitable for metamodelling in order to greatly reduce

the total computation time. Indeed, even if the global consistency of the metamodel could be sufficient, many local discrepancies could subsist.

Therefore, in order to insure both a local and global accuracy of the metamodel, the idea is to use an adaptive sampling strategy (see figure 4.2). The active learning metamodel aims at detecting the regions of interest where the consistency of the metamodel is not compliant and thus, adding new samples in these areas. This sequential method can lead to more accurate results but also longer computations. The critical part is to define a sampling strategy for the new samples and two metrics (along with their corresponding stopping criteria) for the local and global accuracy of the metamodel. This triplet is entirely depending on the studied system and the surrogate process considered. For Kriging, RBF or PCE surrogate models, various adaptive sampling strategies have been presented in the literature [88]. But in the case of PCK metamodeling, only a handful of active learning strategies have been developed in the literature. For example, in [110], Yu et al. used radial centralized adaptive sampling for reliability analysis of thermal-elastic coupled gears.

Therefore, when exploring what has been done for other metamodeling processes, we decided to use an easy-to-implement partitioning algorithm for subdividing the input parameter space. To avoid further calls of our computational model, the chosen non-intrusive local metric has been the CV LOO error within a subdivision with its threshold ε . Instead of using some variance-based criterion which would require additional call of the model, this insure the build of a predictor extremely consistent locally. In the mind of limiting the total number of calls of the input model, the nodes of the partitioning have been ideally included in the sub-sampling. The steps of subdividing and drawing additional samples can therefore be joined together using a quad-tree algorithm design [94], which has already been used for interpolation processes [95]. The global metric came evidently to tackle the curse of dimensionality: limit the maximum number of divisions m of the initial domain. The use of this metamodeling algorithm (see 4.1.2) with the quad-tree based uniform sampling has been compared with other sampling strategies using various test functions (see section 4.1.3).

Then, our algorithm has been tried on a real analytical model available through a collaboration in the MICEV Project [2]. The first test of our algorithm has been successful on this GP algorithm for mutual inductance in the case of a dynamic WPT system. Using this real model, some default values have been determined for the consistency threshold ε and the maximum number of divisions m . This validation analysis has been pursued using a more complex COMSOL-based WPT model from PoliTO, the algorithm has been tried to compute a consistent predictor for various problems: some simple sensitivity analysis to the optimisation of 3F3 ferrite cores (placement and dimensions) on the WPT system using a metamodel-based optimisation process.

Finally, the developed algorithm has been proven powerful at computing predictor at a low computation cost for various input dimensions on both simple and complex models. Another complex problem for high-power IPT systems is the assessment of human exposure regarding guidelines and standards. Thus, the algorithm has been further developed to be used along a voxel-based human 3D model to insure the safety of various devices.

Chapter 5

Human exposure assessment

In the growth of electric mobility, the development of wireless chargers for electric cars is crucial for diminishing battery sizes. This brings the crucial need to properly assess the levels of magnetic field to insure the safety of such WPT devices regarding human exposure standards and guidelines. Moreover, in the industry a wide range of high-power systems are present and need proper human exposure assessment, such as mid-frequency Direct Current (MFDC) welding applications on which the human exposure will be assessed later in this chapter. As already stated in chapter 2, such analysis are made in two steps: first, the magnetic field is mapped on a defined area, then, a voxelized 3D human model is placed in the B-field in order to compute the induced E-field in various areas within the human body.

As already developed earlier, due to the complexity of most WPT devices, in order to perform an accurate sensitivity analysis on the human exposure (regarding the variations of several input parameters), several accurate mappings of the magnetic field would require too many calls of the WPT system computational model. Thus, a surrogate PCK model can be used to compute a consistent predictor of the B-field values (or any field values). But here, an additional computation is required for the human exposure analysis: the induced E-field needs to be computed throughout the human body. As suggested by the ICNIRP [19], the E-field should be averaged over a small volume of $2\text{ mm} \times 2\text{ mm} \times 2\text{ mm}$. For the Duke's model [27]

considered here, more than 300 tissues and organs are taken into account (among 77 different tissue types) and the model resolution can go down to $0.5 \text{ mm} \times 0.5 \text{ mm} \times 0.5 \text{ mm}$. Thus, the computation of such a complex model is extremely long as the grid is usually made of over 10 million cells depending on the posture.

Hence why, for the computation of human exposure to WPT systems, many computational methods have been recently developed which aim at reducing computation time. For automotive applications, Yavolovskaya et al. developed an adapted method of moments using volume integral equations to bypass the use of FDTD or FEM methods [111]. Various alternatives to voxelized human models have been proposed such as in [112] where tetrahedral models are introduced to minimize stair-casing effects on curved boundaries. For computing induced current densities in the human body, the Scalar-Potential Finite-Differences (SPFD) method [113] has already been used in PoliTO for pulsed magnetic fields (such as MFDC welding guns) [114]. Classical FEM methods have also been used at the GeePs and PoliTO for safety assessment of automotive applications [85][115]. Finally, metamodels and especially PCK has already been successfully used for computational dosimetry by Kersaudy et al. for the exposure of a fetus to RF electromagnetic fields [72], where the samples were generated by a nested Latin Hypercube sampling [116].

Therefore, our adaptive sampling strategy for PCK metamodeling could help in saving even more computation time as it already showed better results than an adaptive LHS technique (see section 4.1.3). The active learning metamodeling algorithm (see chapter 4) previously developed has been proven quite efficient at building predictors and performing accurate sensitivity analysis on both complex and simple IPT systems. Due to the great complexity of the two steps of our human exposure analysis, the algorithm has been used here to save computation time by avoiding to many calls of the input system model and the human model. The human exposure regarding three different systems has been performed: a realistic computational model of a standardized WPT charger for automotive applications, an MFDC spot welding gun system and finally a practical WPT system available at the GeePs where some experiments have been conducted.

5.1 Exposure to a standardized WPT charger

Firstly the exposition to a standardized WPT charger has been assessed (see figure 5.1). The considered WPT system model is the WPT3 (11.1 kV A at 85 kHz) class Z3 (Z height $\in [170, 250]$ mm) from the SAE J2954 standard [117] displayed on figure 5.1. In order to assess the worst case in term of exposure, the WPT system has been modelled with the maximum misalignment allowed by the standard between the receiving and transmitting coils, thus creating a high level of magnetic flux density in the surrounding area exceeding the reference levels (see section 2.2.1).

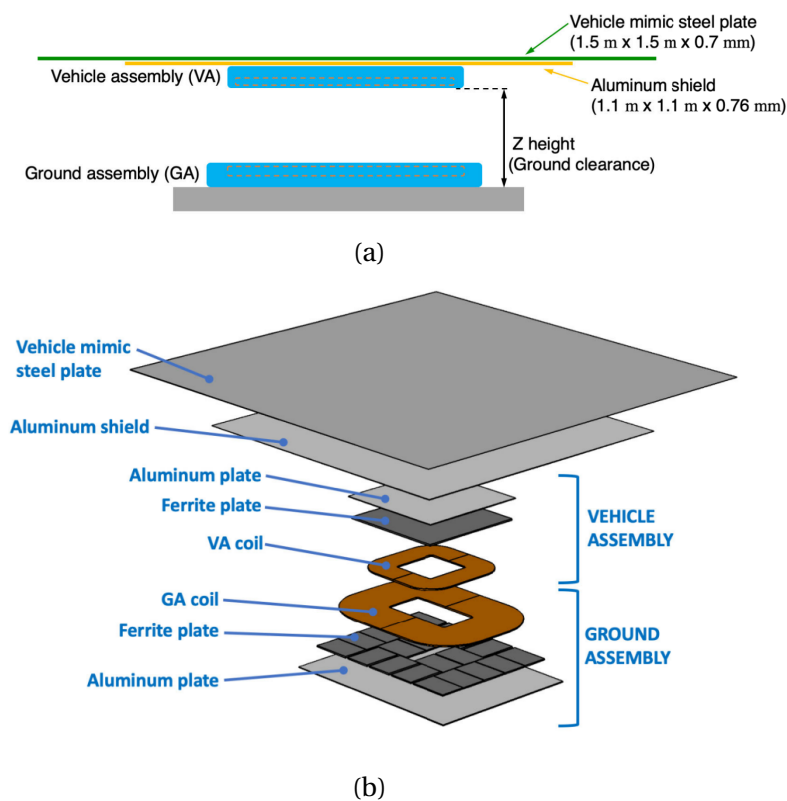


Fig. 5.1 Cut plane (a) and 3D view (b) of the WPT3 (class Z3) system taken from from the SAE J2954 standard [117]

PoliTO provided the computation for the magnetic vector potential for such a system using a hybrid method coupling the surface impedance boundary conditions with the boundary element method [118]. The magnetic vector potential has been computed only in a vicinity area (see figure

5.2), where x is the direction of motion for the car, y is the orthogonal direction and z the gravity axis.

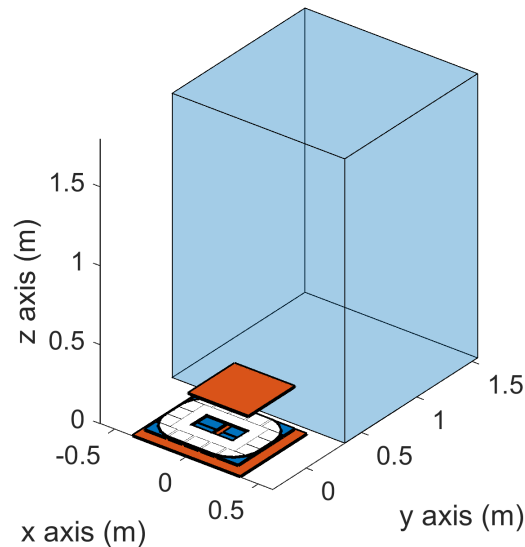


Fig. 5.2 WPT3/Z3 system model from SAE J2954 (maximum misalignment between the coils) with the investigation area (blue box of $1.2\text{ m} \times 1.2\text{ m} \times 1.8\text{ m}$ along the x , y and z axis)

5.1.1 Posture analysis

Using the already provided magnetic vector potential in the vicinity area, the goal has been to try various realistic postures for the human body around a WPT charger for automotive applications. The Sim4Life software from SPEAG [27] has been used to compute the induced E-field in the whole body and inside the pelvis area.

Three different postures (displayed on figure 5.3) have been investigated in this analysis and placed within the investigation area:

- standing position for the human body with a straight posture aside the charger, the normal position for a bystander
- crouching on the side of the charger, which embodies an operator working on the car while it is charging for example

- standing position but bent over with hands opened towards the car, like someone ready to open one of the doors

These three postures have been chosen relying on already analyzed exposure situations in the literature [119][120], the choice could have been made differently but these positions made the most sense for us regarding possible situations of a practical WPT system.

Table 5.1 Maximum, 99.9th percentile and volume-averaged induced E-field (V m^{-1}) in the whole body and the pelvis area for the three studied postures exposed to the WPT3/Z3 charger

	posture	max E	99 th E	$\langle E \rangle$
Whole body	standing	3.66	0.54	0.015
	bent over	0.59	0.58	0.0033
	crouching	6.07	0.68	0.012
Pelvis	standing	3.59	0.42	0.033
	bent over	0.16	0.10	0.16
	crouching	1.09	0.52	0.032

The maximum, 99.9th percentile and volume-averaged induced E-field (V m^{-1}) in the whole body and the pelvis area for the three studied postures exposed to the WPT3/Z3 charger are displayed on table 5.1. For the induced E-field in the whole body, the 99.9th is the highest for the crouching posture next to the WPT charger. The volume-averaged E-field are logically close for the standing position and the crouching position, while the bent over position has a lower one as some part of the human body are further from the charger compared to the other two positions, hence why the peak E-field value in this case is close to the 99.9th value. The same analysis can be made for the critical pelvis area, where the crouching position seems the worst. In this case the difference in terms of 99.9th E-field value is even greater. Therefore for the remaining posture analysis, the crouching posture will be the one further investigated. Thus, the analysis will tackle the human exposure issue for an operator working on a charging car.

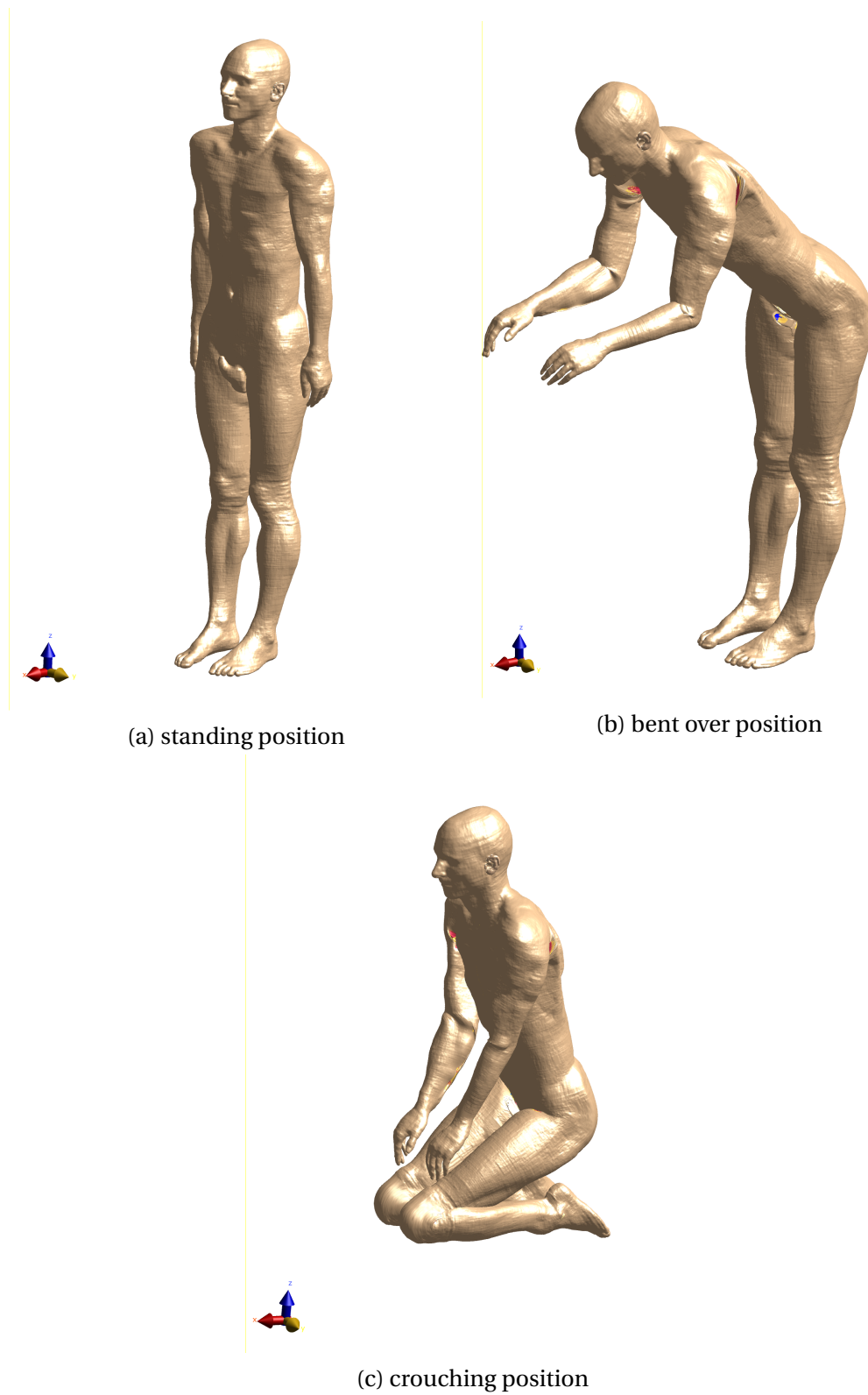


Fig. 5.3 Investigated positions for the human exposure around the WPT3/Z3 charger displayed with Sim4Life

5.1.2 Sensitivity analysis regarding the position of the human body around the charger

The next goal has been to compute a predictor for an exposition factor for the crouching posture regarding the (x, y) position around the WPT3/Z3 charger with maximum coil misalignment. Thus, the previously used computing box has been extended to a $2\text{ m} \times 2\text{ m} \times 3\text{ m}$ along the x , y and z axis on the side of the charger. The active learning metamodel algorithm (see section 1) can be used to compute such a predictor and provide us a Sobol'-based sensitivity analysis on the (x, y) position in order to define a safety area for the operator around the charger.

Choice of an exposure factor

According to the ICNIRP guidelines [19], for a specific tissue, the 99.9th E-field value is the relevant value to compare with the restrictions in terms of exposure (both general and occupational exposure). As the considered crouching posture (see section 5.1.1) embodies an operator, the chosen reference levels will be based on the occupational exposure (higher than the general exposure ones). For a given tissue within the human body, the 99th percentile E-field ($E_{99\text{th}}^i$) can be computed. Given a frequency value (e.g. 85 kHz) and using the reference levels provided by the ICNIRP, an exposure index EI^i can be defined for each tissue i within the human body:

$$EI^i = \frac{E_{99\text{th}}^i}{E_{lim}^i} \quad (5.1)$$

where E_{lim}^i is the basic restriction for general public exposure for the induced E-field in tissue i at the given frequency.

For quantifying the safety of a position (x, y) regarding the WPT system, the chosen exposure criteria is the maximum among all exposure indices available: $EI_{\max} = \max(\{EI^i, \forall i \text{ tissue}\})$. When this value exceeds the unity, the basic restrictions are violated in at least one part of the human body, thus, the given position is not compliant with the standard. The goal of the analysis is to build a consistent predictor for $EI_{\max}(x, y)$ using the

aforementioned adaptive surrogate modelling, which could then be used to define a safety area around the WPT system.

Safety area around the WPT3/Z3 system

The active learning metamodelling algorithm has been used to compute a predictor for $EI_{\max}(x, y)$ around the WPT3/Z3 system. The maximum number of division has been set to $m = 2$ instead of the usual $m = 3$ because of the complexity of the model. Indeed, the 3D Duke model from Sim4Life requires a grid of cubes with sides not bigger than 2 mm in order to accurately compute the induced E-field inside the various parts of the human body. The resulting grid is made of approximately 50 million of cells, which takes around 7 minutes to compute. Moreover, the provided magnetic vector potential consists of two parts: the real and imaginary parts, thus, two computations are needed for every datapoint and the results are joined together afterwards. Due to the bidimensional input space and with $m = 3$, the maximum number of computed datapoints (see equation 4.1) is $n_{\max} = 290$ which could make the computation last 34 h instead of 10 h with $m = 2$ ($n_{\max} = 82$). The *LOO* threshold has been set to $\varepsilon = 0.3$ as previously. The resulting metamodel needed only $n_{\text{samples}} = 35$ with a consistency of $LOO = 1.945 \cdot 10^{-1}$. The resulting predictor has been plot on the color map of figure 5.4 with different levels for the exposure factor ($EI_{\max} = [0.3, 0.5, 0.7]$).

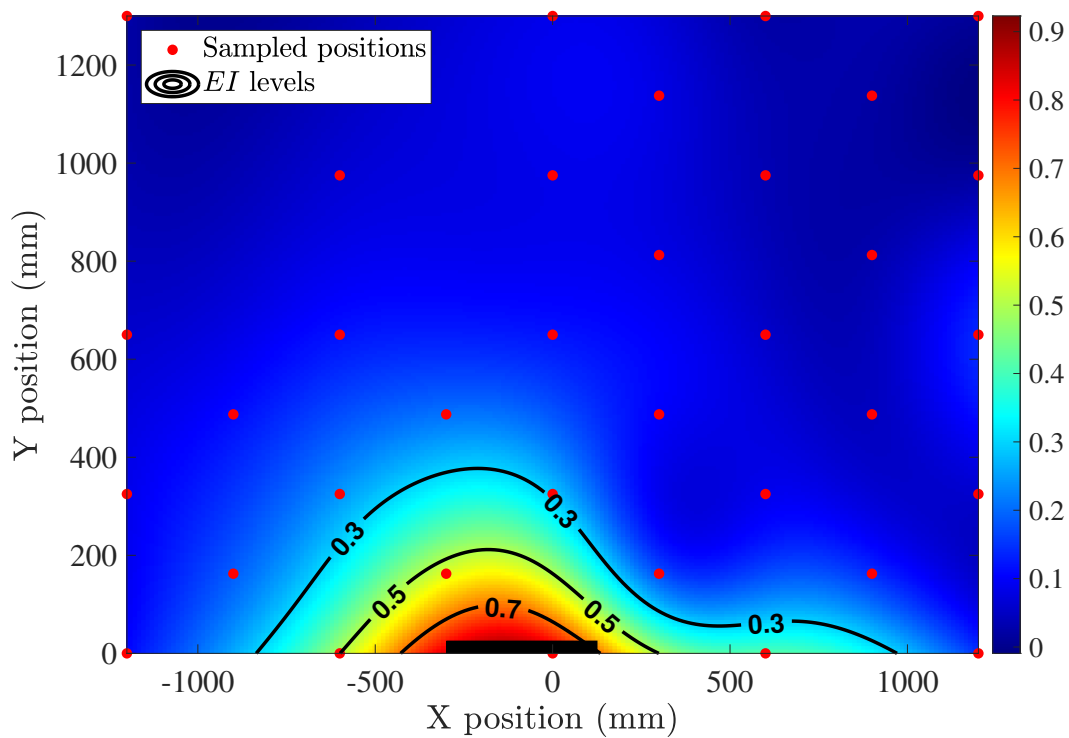


Fig. 5.4 PCK metamodel ($n_{samples} = 35$, $LOO = 0.1945$) of $EI_{max}(x, y)$ for various positions of a crouched operator around the WPT3/Z3 system (black rectangle)

The analysis of Fig. 5.4 shows that there is no need to define a safety area for the operator around the WPT system as even close to the device the exposure index does not exceed 0.9. Moreover, when looking at the contour levels in figure 5.4, inside the main part of the investigation volume the exposure index does not exceed 30%. Since the coil misalignment is the greatest, and the posture leading to the worst exposure scenario has been considered, it can be assumed that the WPT3/Z3 device is compliant for all postures considered here.

Another interesting result is the Sobol'-based sensitivity analysis, giving us the following total Sobol' indices: $S_x^T = 0.432$ and $S_y^T = 0.777$. Even if the analysis cannot be completely trusted due to the low consistency of the metamodel, the logical observation is confirmed as the y position is more important than the x position. As the magnetic field is decaying inversely proportional to the distance from the coils, far away from the device, thus, along the y -axis, the exposure factor is brutally decaying away from the

WPT system and is highly sensible to the y position. Again the safety to stay far away from the charging device is logically confirmed.

Discussion

The first thing to notice is the high value for the LOO , with almost 20%. The algorithm stopped because of small enough LOO on every subdomain from the quad-tree grid (the LOO on every subdomain is not greater than 1%). This can be explained by the fact that EI_{\max} is not a regular scalar output but the maximum of a list of different values. For two different sampled positions for the human body, the maximum of the list ($\{EI^i, \forall i \text{ tissue}\}$) can be obtained for two different tissue types. For example, at the position $(-1200, 650)$ the maximum value for EI^i corresponds to the tissue i being inside the wrist, whereas at the position $(-300, 325)$ the maximum is the value for the testicle. Therefore, the small LOO values for the sub-metamodels can be explained by the fact that inside a subgrid of 5 samples the maximum is obtained for the same tissue i . Thus, a metamodel for the list ($\{EI^i, \forall i \text{ tissue}\}$) could be built using the algorithm and would result in a more consistent metamodel. Yet, this consistency is sufficient enough to draw tendencies on the safety of the WPT system regarding the position of the human body.

Finally, the analysis developed here is only of small interest on this device due to its total safety for an operator. But the protocol which has been used and develop to assess the safety of this WPT system is the interesting part. The analysis can be extended to not necessarily more complex systems but needier systems. Indeed, this protocol has also been used to insure the safety of other high-power systems such as MFDC welding guns.

5.2 Exposition to an MFDC spot welding gun



(a)



(b)

Fig. 5.5 Working area where welding operations are performed (a) with an MFDC welding gun (b), taken from [121]

The previously developed dosimetric protocol has been applied to an MFDC welding gun (see figure 5.5b) in order to investigate the human exposure of resistance spot welding processes. This resistance welding process consists in heating the metal at the joint using a high current pulse (~ 10 kA, 100 ms). Thus, the levels of magnetic field generated by this IPT device in the vicinity (see figure 5.5a) are extremely high compared to WPT systems. Moreover, because the generated magnetic field comes from a current pulse, the device does not work at a fixed frequency unlike the WPT3/Z3 system studied earlier. Therefore the challenge is to properly assess the human exposure of the gun while taking into account all the frequencies in the

pulse spectrum, indeed, the reference levels are dependent on the body area but also on the input frequency.

5.2.1 Simple model for a welding gun

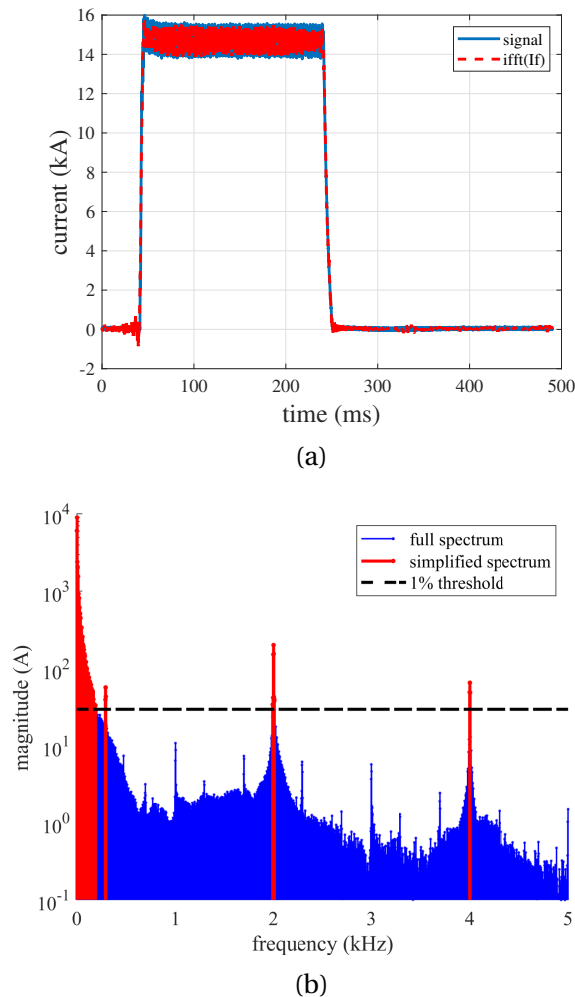


Fig. 5.6 Real welding current pulse measured at PoliTO (in blue) with the simplified pulse considered in our simulation (in red) (a), original and simplified spectrum of the measured current pulse with the black line at 1% of the fundamental (b)

The welding pulse taken into account in the analysis has been measured on a real system at PoliTO. The considered current pulse (shown in blue on figure 5.6a) is a rectangular pulse with 5 ms of raising time, an amplitude of 15 kA and a weld time of 200 ms. As observed on its spectrum (displayed on

figure 5.6b), many components are irrelevant in the analysis and are making it extremely dense, thus, difficult to work with for the analysis. Therefore, all the components below 0.5% of the fundamental have been considered negligible and removed from the spectrum. The resulting spectrum is displayed on figure 5.7 with the corresponding signal computed with an inverse fast Fourier transform displayed on figure 5.6a in red. This signal will be the one considered in this analysis.

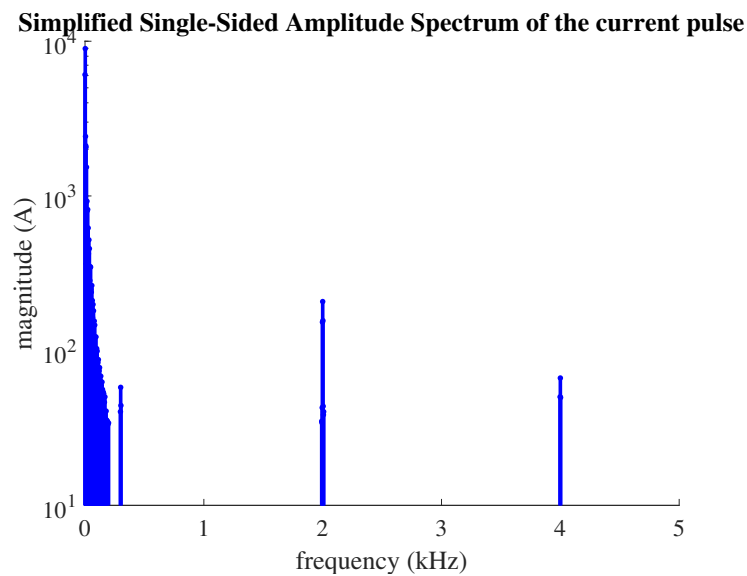


Fig. 5.7 Simplified spectrum for the MFDC current pulse with all the components below 0.5% of the fundamental ignored

The gun body along with the MF transformer is considered shielded. Therefore, a simple rectangular current loop (0.5 m by 0.2 m, in blue on figure 5.8) has been considered (as made in [122]) for the modelization on Sim4Life. The gun is simulated at a fixed height ($z = 1.25$ m in the different simulations). At a given frequency, the magnetic vector potential and the Magnetic Flux density can be computed using the built-in LF solver and then, the Duke's model is placed in the vicinity area (see figure 5.8) with its position (x, y) centered in $(0, 0)$ the position of the loop center.

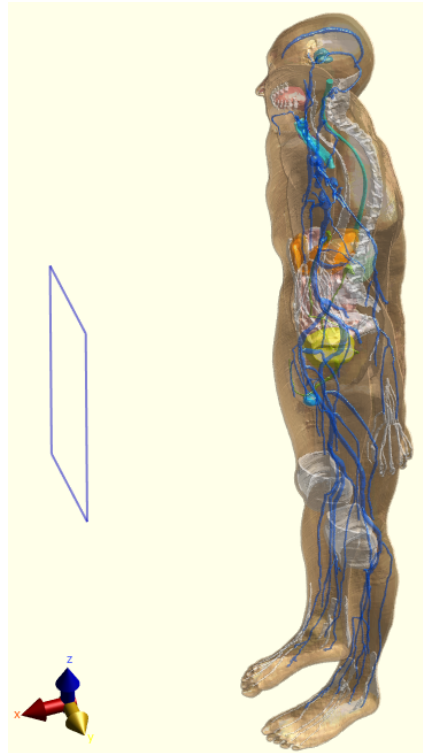


Fig. 5.8 Duke's model for the operator facing the rectangular current loop (in blue) from the MFDC spot welding gun

5.2.2 Multi-frequency metamodelling

Choice of an exposure factor

Unlike a WPT system, the waveforms generated for MFDC welding guns are pulses, thus, producing non-sinusoidal fields. Therefore the computation of the exposure factor (see section 5.1.2) must be performed differently. The weighted peak method [123] (WPM) based on the SENN model [124] and suggested by ICNIRP low-frequency EMF guidelines defines an exposure index E_i including all frequencies for a pulsed magnetic field. For a given tissue i in the human body, EI^i must verify:

$$EI^i = \left| \sum_j \frac{E_{99\text{th}}^i}{E_{\text{lim}}^i(f_j)} \cos(2\pi f_j t + \theta_j + \varphi_j) \right| < 1 \quad (5.2)$$

where $(E_{99^{\text{th}}}^i, \theta)$ is the 99th percentile of the induced E -field RMS value and its phase, (E_{lim}^i, φ) the corresponding reference level and phase at the given frequency f_j . The WPM is simply a low-pass filter whose magnitude is $1/E_{lim}^i$ and the phase is φ_j . Both of these parameters are defined by the exposure requirements from ICNIRP 2010 guidelines [19]. The characteristics of the filter for a central nervous system (CNS) tissue of the head in the case of occupational and general public exposure are displayed in Fig. 5.9.

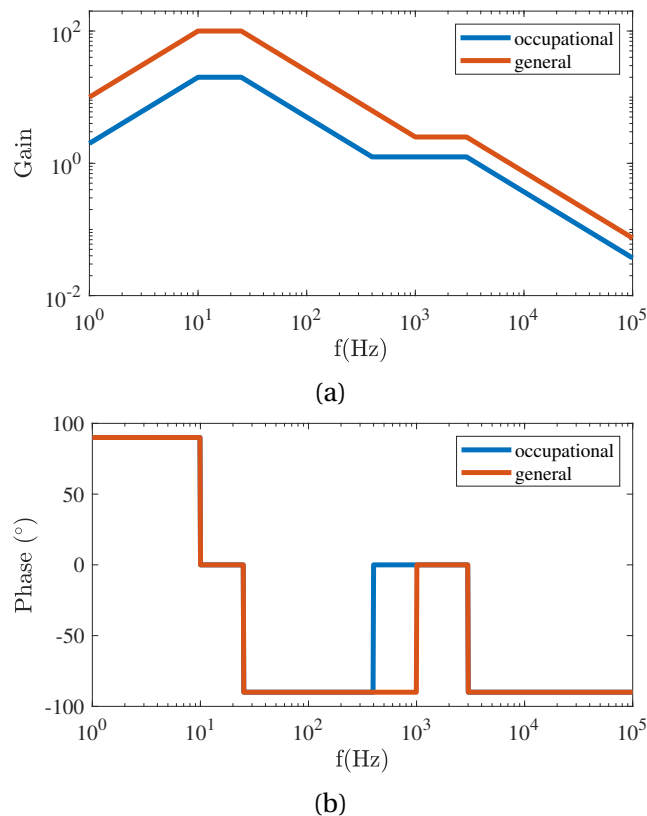


Fig. 5.9 Gain (a) and phase (b) of the WPM filter for CNS tissue of the head in the case of an occupational exposure (blue) and general exposure (red) for the induced E-field

Similarly as the previous analysis, for assessing the safety of the given position for the operator of the welding gun, the chosen exposure criteria is the maximum among all exposure indices available: $EI_{\max} = \max(\{EI^i, \forall i \text{ tissue}\})$. When this value exceeds the unity, the reference levels are violated in at least one part of the human body, thus, the given position is not safe for the operator.

Frequency scaling

In order to compute the total exposure index EI_{\max} for a single position (x, y) of the human body around the welding gun, a lot of computation would be needed due to all the frequencies in the pulse spectrum and all the different tissues in the human body. Using our active learning metamodel directly on this input model would take too much time or could not provide us a predictor consistent enough in a small amount of time. Thus, the computation of both a safety area and a sensitivity analysis of the operator's position would be impossible.

Therefore, the goal is to simplify the electromagnetic problem in order to compute the dosimetric quantities only at a given frequency. At each position (x, y) investigated in the active learning algorithm, only one call of the Sim4Life model is made. The resulting dosimetry quantity can then be used to compute the total exposure index EI_{\max} at this single position by post-processing.

The computation of the induced E -field in a given tissue i can be performed at a single frequency f : $\vec{E}^i(f)$. Then, this result can be transposed to any frequency using frequency scaling with the quasi-static approximation [125]:

$$\forall f', \vec{E}^i(f') = \left(\frac{f'}{f}\right) \left(\frac{\sigma + j\omega\varepsilon}{\sigma' + j\omega'\varepsilon'}\right) \left(\frac{I'}{I}\right) \vec{E}^i(f) \quad (5.3)$$

with (σ, σ') and $(\varepsilon, \varepsilon')$ the conductivity and permittivity of tissue i at the frequencies f and f' , and I, I' the amplitude in the simplified spectrum of the current pulse at the angular frequencies $\omega = 2\pi f$ and $\omega' = 2\pi f'$. The quasi-static approximation is valid here as for $f_{\max} = 4$ kHz, $\lambda \simeq 7.49 \times 10^5$ m which is huge compared to the size of the body. The variation of the dielectric properties regarding the frequency for all considered tissues have been computed using the values from the IT'IS database [28].

Discussion

The frequency scaling is relying on the known variation of the dielectric properties $(\sigma^i, \varepsilon_r^i)$ against the frequency for all considered tissues. Unfortu-

nately the frequency dependency of most tissue properties is not yet fully reliable for frequencies below 1 MHz. Indeed as developed in the analysis of this new formulation [122], some variations can be observed for the peak of the WPM signal between the full model and the simplified model: for most tissues the percentage error is negligible ($< 10\%$) but can go up to 30%. The higher values are corresponding to tissues with extremely low exposure factor and therefore not modifying the safety of the device. This can be explained by the fact that the conductivity of these tissues has only been assessed a few times and the resulting frequency-dependent model cannot be trusted.

Thus, for the exposure assessment of the MFDC spot welding gun, the weighted peak method has only been applied to a handful of tissues. The chosen tissues are the ones among the IT'IS database with many studies conducted on it. Moreover, a second selection of critical tissues has been done, which are known in the literature to exceed exposure limits in the vicinity of MFDC welding guns [126][127]. This enables us to compute fewer dosimetric quantities and speeds up at the same time the complete computation of the metamodel by preventing to compute irrelevant data regarding the safety of the device.

The chosen tissues with the number of samples used for building the dielectric model against the frequency are displayed in table 5.2. For example, the low frequency variation of the different conductivity are displayed on figure 5.10. Even if the frequency variation can be considered as negligible for the Bone Marrow (Red) and the Skin, for all the other tissues considered the frequency is highly affecting the conductivity value, thus, the frequency scaling must take into account the variation of the conductivity as it cannot be considered constant within the frequency range.

Table 5.2 Relevant tissues considered in our WPM analysis with the number of studies in the literature used to build the low frequency dielectric model in the IT'IS database [28]

Tissue	number of studies
Bone Marrow (Yellow)	25
Cerebellum	33
Brain (Grey Matter)	214
Brain (White Matter)	194
Fat	91
SAT (Subcutaneous Fat)	91
Skin (Dry)	7
Spinal Cord	60

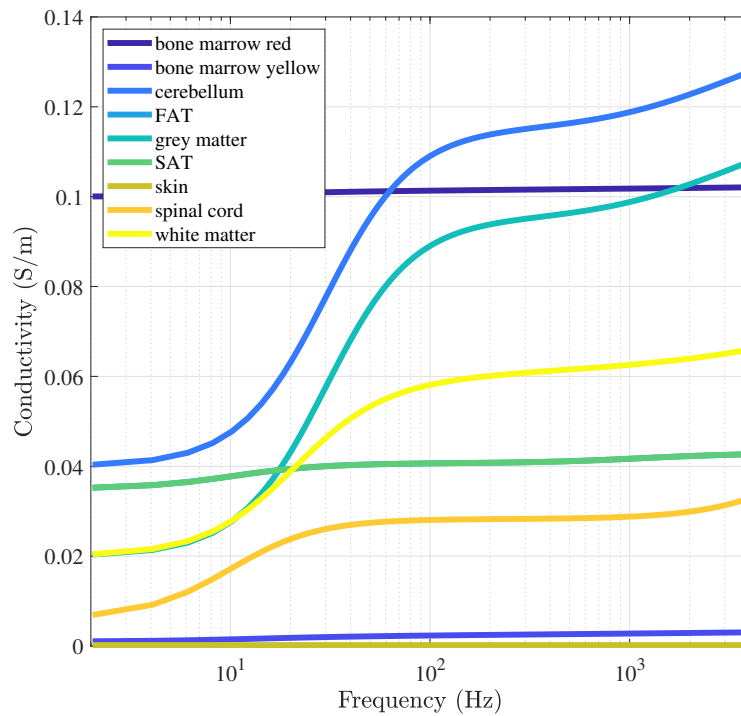


Fig. 5.10 Variation of the conductivity against the frequency for the considered tissues in the exposure analysis

5.2.3 Compliance safety areas

Input dataset for the metamodel algorithm

The spot welding gun is considered at a stationary position throughout the analysis and the Duke's model is moved in a vicinity area behind the gun (see figure 5.11) along the x and y axis. The possible ranges of variations for the (x, y) position of the human body (center of the box surrounding the Duke's model) are $x \in [140\text{mm}, 640\text{mm}]$ and $y \in [-700\text{mm}, 700\text{mm}]$.

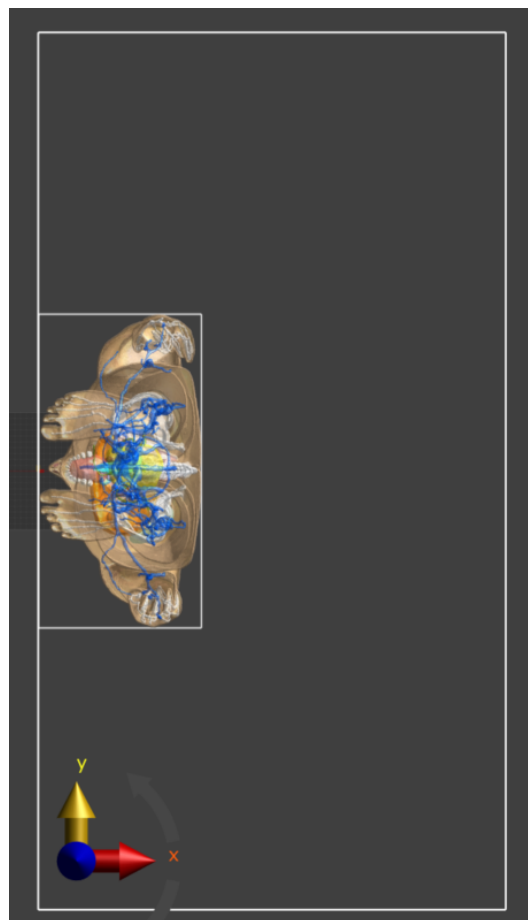


Fig. 5.11 Vicinity area considered for the exposure problem behind the MFDC welding gun

The computations have been performed at $f = 46.94$ Hz which fits a current value $I = 346.8$ A and phase $\phi = -86.94^\circ$ in the pulse spectrum (see 5.7). The given current, phase and frequency have been set for the current loop in

Sim4Life to compute the magnetic potential in the whole computation grid. Then, for a given position (x, y) , the 99.9th percentile induced electric field is computed in each of the 8 relevant tissues. A datapoint for the metamodel is therefore the position (x, y) and the corresponding 8 by 1 vector for the induced E-fields. Thus, using the active learning metamodel algorithm (with $m = 2$ and $\varepsilon = 0.3$ as in section 5.1.2), 8 different metamodels are computed for the 99.9th percentile induced electric field for every tissue type considered at $f = 46.94$ Hz against the position of the human body. The resulting sensitivity analysis is displayed on table 5.3.

Table 5.3 Sensitivity analysis for the 99.9th percentile induced E-field in the relevant tissues considered in our WPM analysis against the position of the human body behind the welding gun ($n_{samples} = 28$, mean $LOO = 5.454 \cdot 10^{-2}$)

Tissue	S_x^T	S_y^T	LOO
Bone Marrow (Yellow)	0.789	0.391	$4.793 \cdot 10^{-2}$
Cerebellum	0.775	0.272	$9.302 \cdot 10^{-3}$
Brain (Grey Matter)	0.918	0.151	$6.239 \cdot 10^{-3}$
Brain (White Matter)	0.872	0.186	$1.140 \cdot 10^{-2}$
Fat	0.683	0.478	$9.432 \cdot 10^{-2}$
SAT (Subcutaneous Fat)	0.696	0.478	$6.949 \cdot 10^{-2}$
Skin (Dry)	0.610	0.539	$1.153 \cdot 10^{-1}$
Spinal Cord	0.907	0.190	$8.234 \cdot 10^{-2}$

The active learning metamodeling algorithm has been successful at building the various predictors for all considered tissues. The computation of 28 datapoints took only few hours with a Duke's model voxelized with $2\text{ mm} \times 2\text{ mm} \times 2\text{ mm}$ voxels and the resulting LOO are not exceeding 10% apart from the metamodel for the Skin at 11.5%. Therefore the resulting predictor for each tissue are consistent enough to be used for sensitivity analysis but also exposure factor computations. As for the WPT structure (see section 5.1.1), regarding the sensitivity analysis, the conclusion is similar with the x axis being the most important direction for most tissues with the y position not negligible. Thus, the operator is safer at standing on the side of the gun instead of in front of it.

Safety area behind the gun

For a given position (x, y) of the Duke's model, using the available consistent predictor on each of the 99.9th percentile induced E-field at $f = 46.94$ Hz, with equation 5.3, the 99.9th percentile induced E-field can be computed at every frequency of the pulse spectrum. Then the weighted peak method (see section 5.2.2) can be applied to the 8 different tissues and 8 waveform are computed at a given position (x, y) . For example, the waveform corresponding to the exposure index for the skin is displayed on figure 5.12 for two different positions: $(x, y) = (400 \text{ mm}, -200 \text{ mm})$ (5.12a) and $(x, y) = (200 \text{ mm}, 0 \text{ mm})$ (5.12b). The exposure index waveform for position (a) is always under the limit ($\max(I_{WP}) \leq 1$), thus this position is safe. While for the position (b), ($\max(I_{WP}) \geq 1$) and this position is not safe regarding the exposure only of the skin.

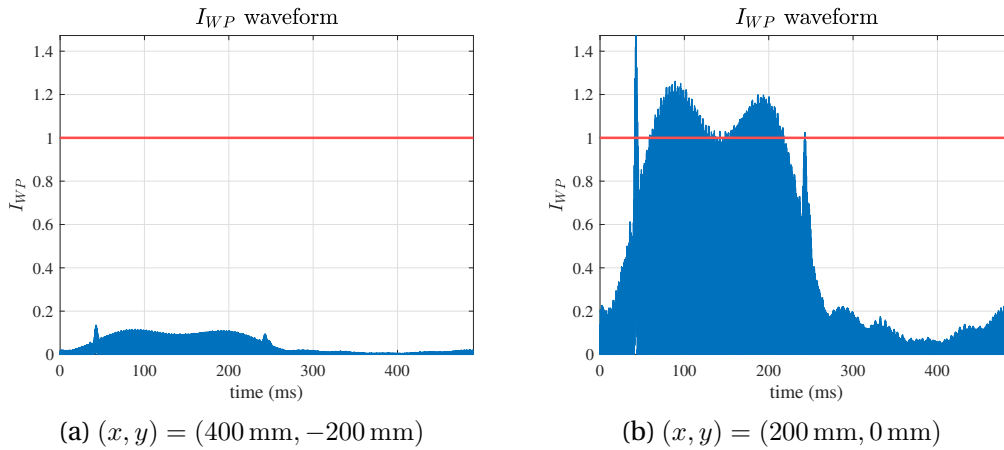


Fig. 5.12 Weighted peak method for the skin for two different positions (a) and (b) around the MFDC spot welding gun (the limit at $I_{WP} = 1$ is displayed in red)

For the tissue i , the peak I_{WP}^i can be detected in the waveform, if $I_{WP}^i > 1$, the position is not safe for this tissue. By computing the 8 peaks at the given position, one can confirm the safety of the position if all peaks do not exceed one. This leads to the definition of a safety area when analyzing $(x, y, \max(I_{WP}^i))$.

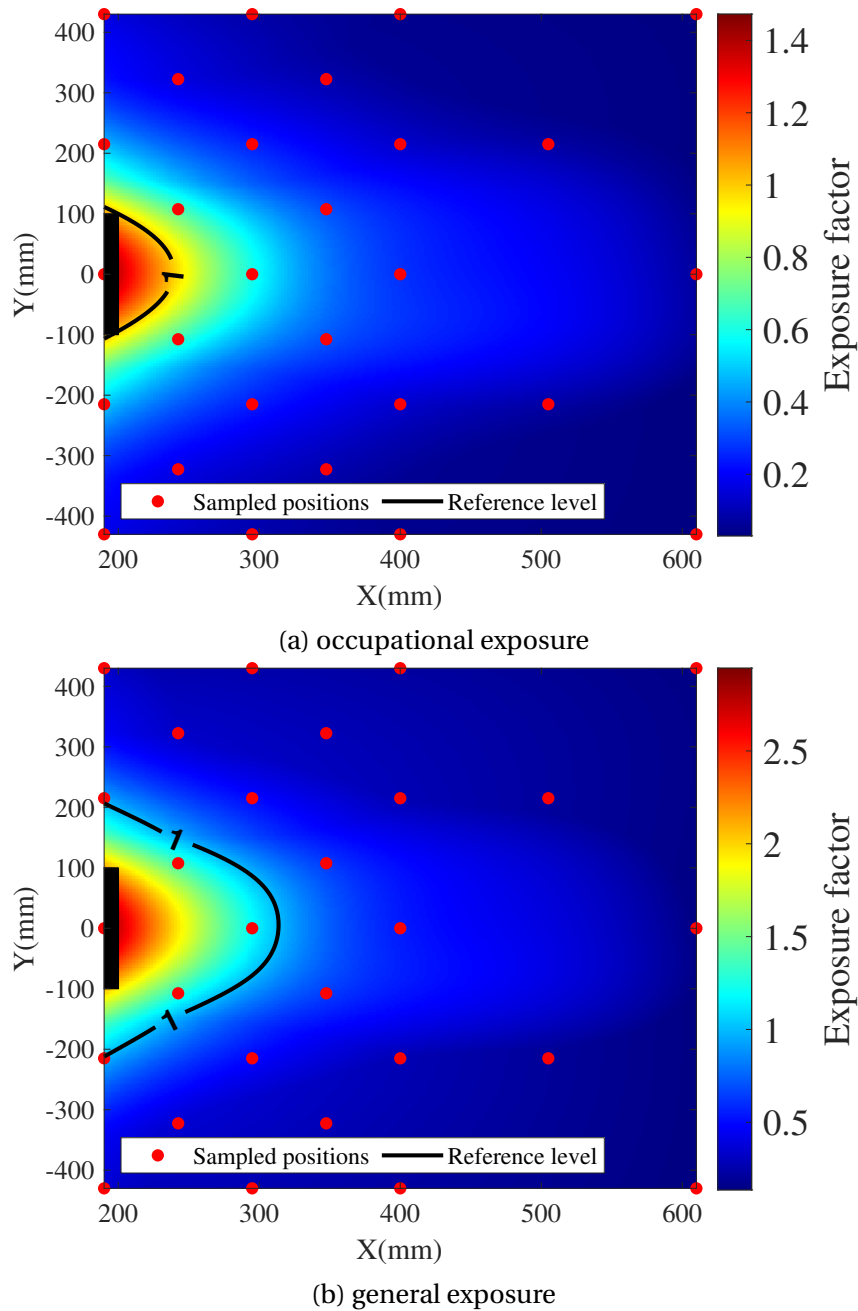


Fig. 5.13 Variation of the exposure index and safety area ($\max(I_{WP}^i) < 1$) behind the MFDC welding gun for occupational exposure (a) and general public exposure (b)

The variations of $\max(I_{WP}^i)$ behind the gun and the safety area where $\max(I_{WP}^i) < 1$ are displayed on figure 5.13a in the case of occupational exposure (blue filter on figure 5.9). Considering our computation box (see

figure 5.11), most of the vicinity area of the welding gun is safe for the operator. Close to the gun, the exposure factor is exceeding 1, meaning the 99.9th percentile induced E-field is above the limit for at least one of the 8 tissue types considered. Therefore, the safety area on all sides is at least 250 mm behind the gun.

From the industrial point of view, this safety area correlates the observation already made on existing operating devices in [121]. Indeed, in the case of public exposure, this system might be more dangerous. The same analysis can be performed for general exposure (orange filter on figure 5.9) with the safety area displayed on figure 5.13b. This time the safety area on all sides is at least 325 mm behind the gun. That is why some protections have been developed especially for the arms around the welding device.

Discussion

Using the predictors available for the 8 different tissues previously considered, the same safety area analysis can be performed on each tissue separately to see which tissues are the most endangered during the welding process. The resulting safety areas for each tissue (for general exposure) are displayed on figure 5.14. The critical tissues in our simulation are the skin along with the fat and subcutaneous fat as their safety area are the largest.

These three tissues (FAT, SAT, skin) are all constitutive of most body parts and are also the first tissue types exposed directly to the magnetic field. Indeed, the skin is first exposed to the outside on the human body, followed by a small layer of SAT on the whole body. Therefore a mitigation solution for the design of some specific protective clothing would decrease both the induced E-field in these critical parts but also the induced E-field in the other tissues inside the human body (after some layers of skin and/or SAT/FAT). In our study, the remaining tissues (apart from the bone marrow) are all parts of the CNS, thus, their exposure limit is much smaller at most frequencies than the FAT, SAT and skin. Yet, they are not the critical tissues regarding the exposure as their safety areas do not exist and the operator could be at a reasonable distance of the welding gun.

An explanation could be that all the CNS is perfectly protected within the human body under several layers of FAT, SAT, skin but also several liquids (like the cerebrospinal fluid for example) acting like buffers to absorb both physical and chemical dangers. For example, the cerebellum considered within the human body is always safe regarding its exposure ($I_{WP} < 0.04$) during our simulation as it is encapsulated at the back of the head behind the skin followed by a layer of SAT, the skull (made of bone marrow) and several layers of dura mater, arachnoid mater, and pia mater into which the cerebrospinal fluid is circulating. A complete study could also be performed by considering all parts of the human body but the computation time would explode as in the Duke's model, more than 77 different tissue type are considered. That is why only some relevant critical tissue types have been considered here.

Moreover, this simulation is all based on a considered magnetic pulse (see figure 5.6) and the results provided here could be different for another pulse. This simulation has been performed in order to display the tendencies of such an high-power device and to show the use of the various methodologies coupled with our metamodel algorithm. Compared to the existing methodologies for the exposure assessment of MFDC welding guns cited earlier, our development brings a great decrease in computation time for this extremely complex system. As in [126], thanks to the reliable computed predictor, various mitigation solutions for the welding gun could be analyzed fastly along with the influence of various welding parameters such as the rising time of the pulse or the peak current.

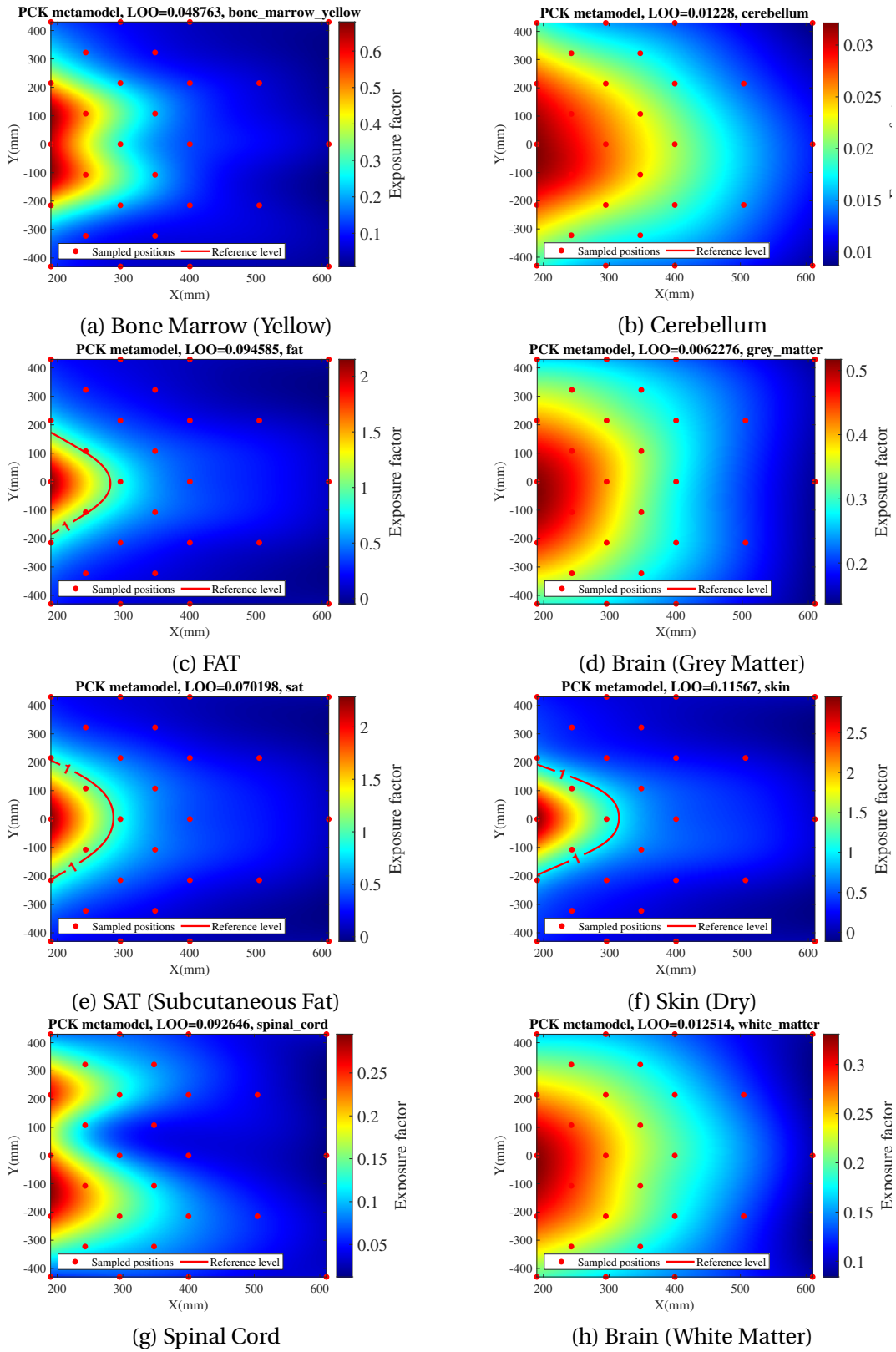


Fig. 5.14 Variation of the exposure factor and safety area ($I_{WP} < 1$) behind the MFDC welding gun for the different tissues investigated in the case of general exposure

5.3 Exposure to a practical WPT system

Surrogate models and especially PCK metamodelling have been proven extremely useful at building consistent predictors for complex WPT systems so far. But all the models developed before have been challenged only against simulation results. Hence why in this section, the goal has been to present some results obtained on a real coupling structure aimed at dynamical WPT charging for automotive applications. The idea has been to use metamodelling to predict the magnetic field values around the charger at high power using only few experimental values.

The WPT system studied in this section has been developed during Wassim Kabbara's PhD [128] between the GeePs and Renault. The various experiments have been performed by Chloé Bourion and German Orlov during a master's degree project with Mohammed Bensetti and Lionel Pichon.

5.3.1 Experimental WPT system

The coupling structure available on the experimental bench is made of two identical coils on the top of each other (see figure 5.15). Each coil is made of:

- 8 coil turns of litz wire
- 60 plates of ferrite
- 8 capacitors of 33 μF

The working frequency is around 85 kHz. The material parameters are displayed on table 5.4.

Table 5.4 Material parameters of the coils in the WPT system studied at the GeePs (at 85 kHz)

material	conductivity (S m^{-1})	relative permittivity	relative permeability
Cu	$5.8 \cdot 10^7$	1	1
ferrite	0.01	12	1800

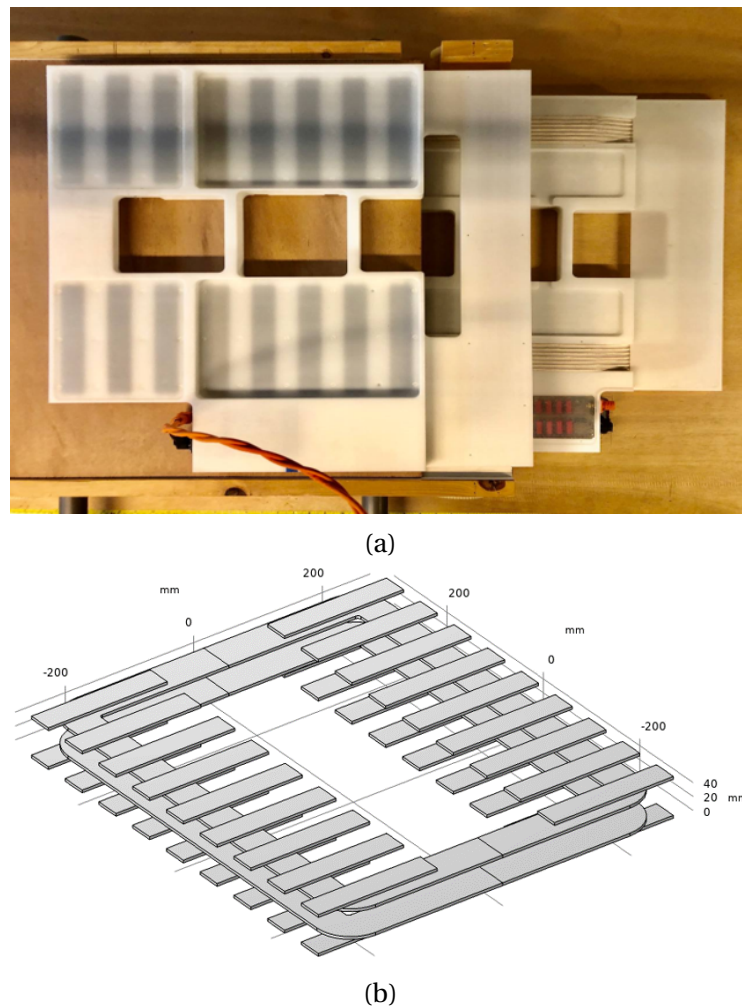


Fig. 5.15 WPT structure developed by Wassim Kabbara at the GeePs (a) and its corresponding COMSOL model (b)

5.3.2 Magnetic field mapping

Experimental setup

The bench for measurements is displayed on figure 5.16. The coupling structure is considered with both coils aligned and the magnitude of the B-field around the charger is measured with a WAVACONTROL SMP2 probe. The bench has been built without any metal parts (only wooden parts) to prevent any interaction with the coils during the induction. The transmitting coil is supplied by an inverter where the input current can be tuned to

modify the working power of the system. The receiving coil is connected to a resistive load-bank to match the maximal output power. Input and output currents along with the output power are measured at every point.

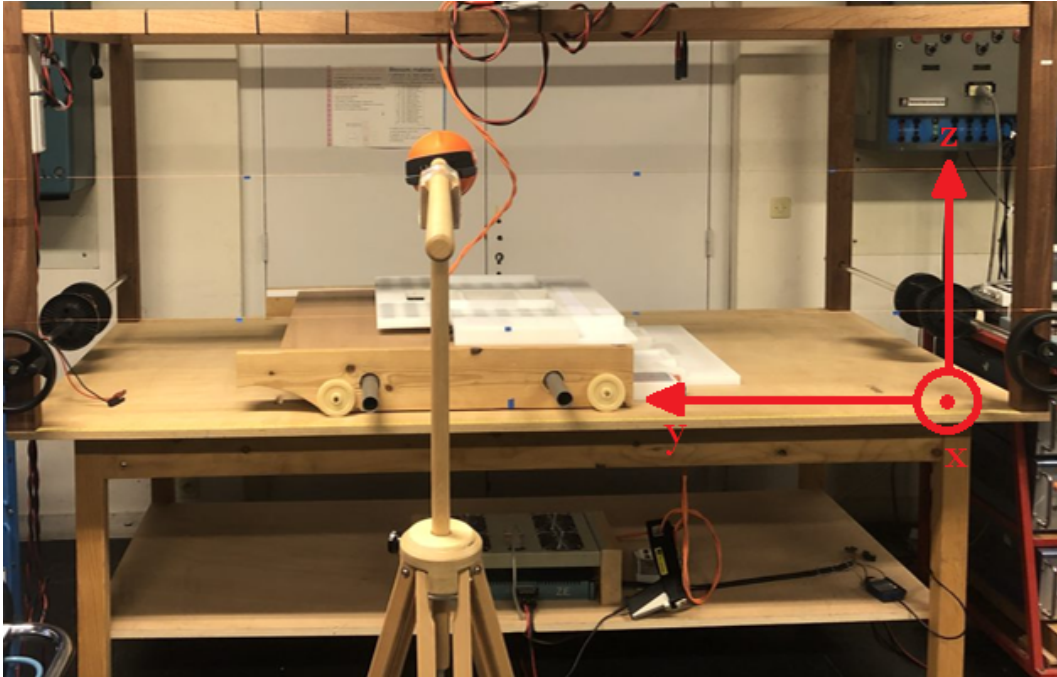


Fig. 5.16 Bench for measuring the magnetic field around the working WPT charger with the WAVACONTROL SMP2 probe

Input dataset

Two separate experiments have been performed: one at low power ($f = 86$ kHz, $P_{output} = 250$ W) and one at high power ($f = 88$ kHz, $P_{output} = 600$ W). For both experiments the amplitude of the B-field have been measured at the same points with an input dataset taking into account all combination in the following ranges:

- 3 points along the x axis: 642 mm, 792 mm and 942 mm
- 5 points along the y axis: 508 mm, 808 mm, 1108 mm, 1408 mm and 1708 mm
- 2 points along the z axis: 203 mm and 526 mm

The experimental design within the input parameter space is displayed on figure 5.17. The origin of the axes is the front right corner of the bench (see figure 5.16).

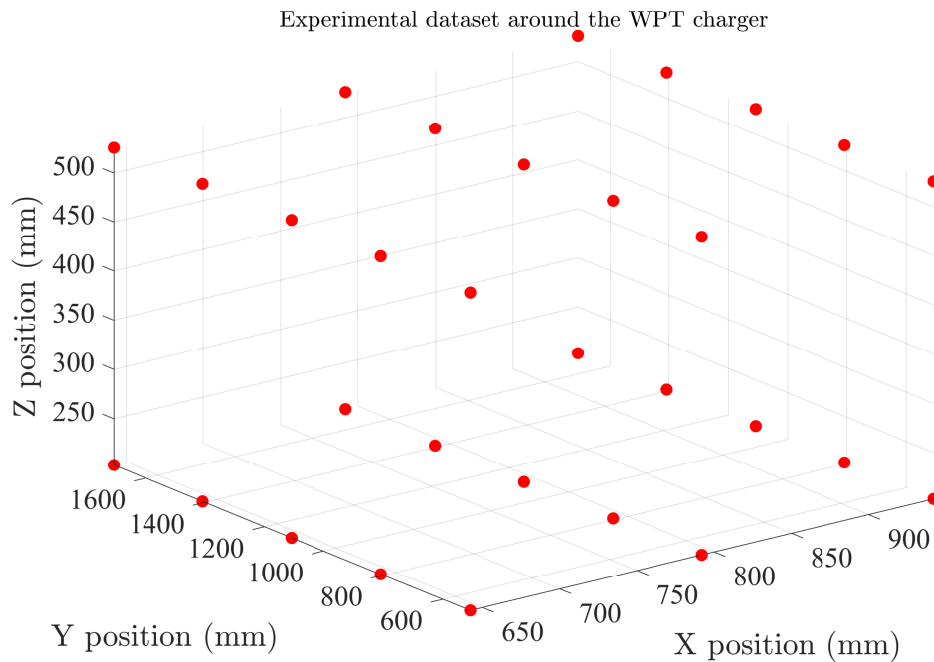


Fig. 5.17 Points around the charger where the magnitude of the B-field has been measured with the WAVACONTROL SMP2 probe

Results

Using this input dataset, a PCK metamodel has been computed for both high and low power setup. The resulting sensitivity analysis is displayed on table 5.5. The first thing to notice is the consistency which falls in an acceptable range of values even with experimental data ($LOO < 4\%$). Thus, the corresponding predictors are consistent enough to provide us an accurate sensitivity analysis. For the low power system, the total Sobol' indices are similar to the analysis conducted on the simulation model of the WPT3/Z3 system (see section 5.1.2): the x position is more important than the y and z positions. As the magnitude of the magnetic field is inversely proportional to the distance from the coupling structure, the x axis is the

most influential direction with the y and z axis having similar influence regarding the considered range of variation.

Table 5.5 Sensitivity analysis and consistency of the PCK metamodels built from the experiments on the real WPT structure at the GeePs

Power	LOO	S_x^T	S_y^T	S_z^T
250 W	$3.250 \cdot 10^{-2}$	0.642	0.449	0.147
600 W	$3.865 \cdot 10^{-2}$	0.659	0.308	0.320

The differences observed for the high power system can mainly be explained by the low accuracy on the measured values. Indeed, the measured B-field values have been compared to the values from the equivalent COMSOL model and the average percentage error is 11.33% for $P_{output} = 600$ W (ranging from 0.02 to 24.55%). Whereas for the low power system at $P_{output} = 250$ W, the average percentage value is 5.89% (ranging from 0.23 to 16.39%). Between the low power experiment and the high power experiment, the measuring process has not been fully reproduced which can explain the higher uncertainty on the probe measurements. Fortunately most of these inaccurate values are positions far from the coils, mainly in the range $x = 792$ mm or 942 mm, where the magnetic field strength is so low that it does not affect the human exposure assessment ($B < 3 \mu\text{T}$).

The map of the B-field around the coupling structure working at $P_{output} = 600$ W is displayed for various cut planes on figure 5.18. The results from the uncertainties mentioned earlier can be observed around $X = 850$ mm on subplots (a), (c) and (d). The position of the WPT device is marked in black. As observed in the sensitivity analysis, the brutal decay of the magnetic field strength along the x axis can be observed.

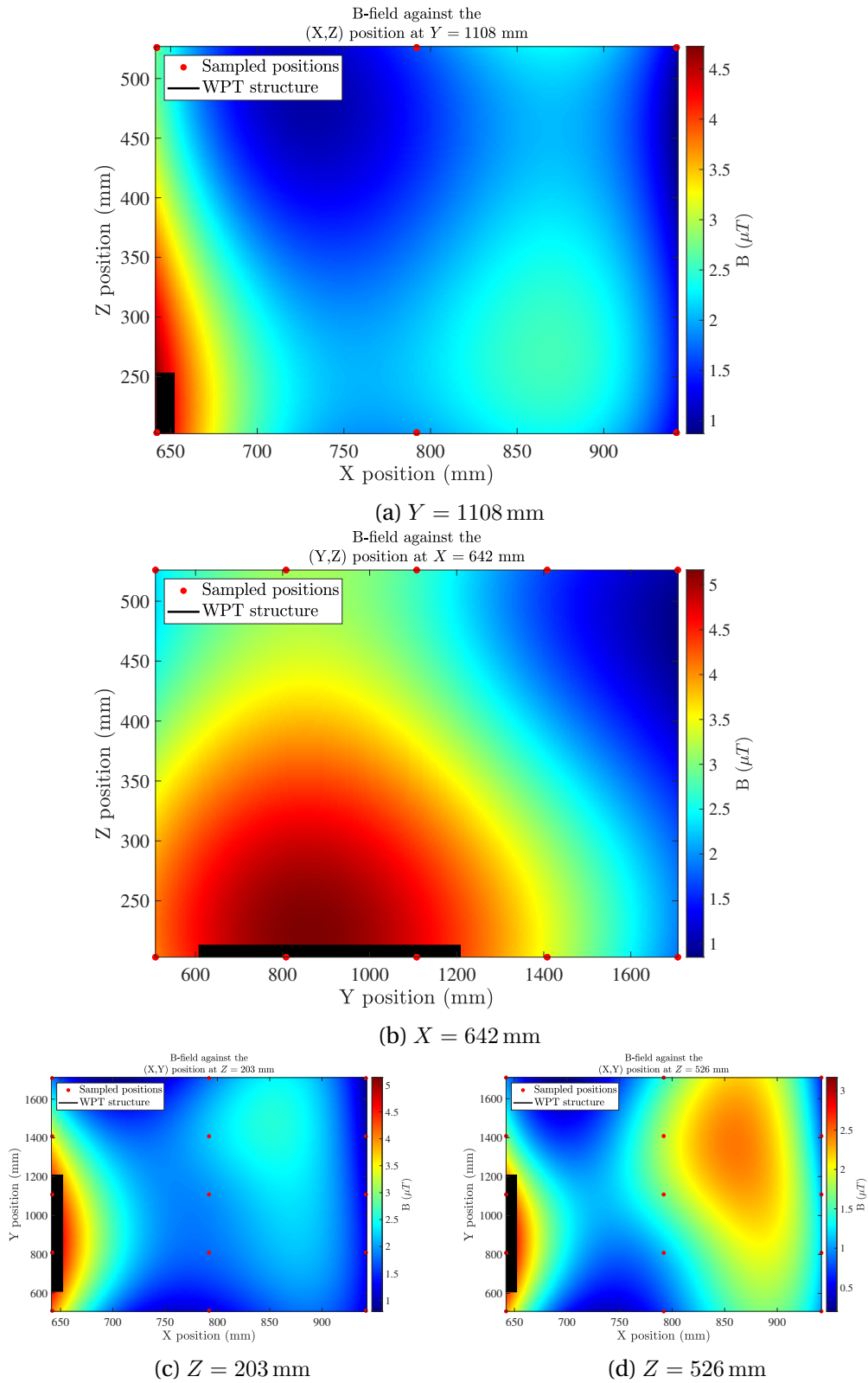


Fig. 5.18 Magnitude of the B-field predicted with the PCK metamodel (sampling points in red) for the experimental WPT structure (in black) on various cut planes at $P_{output} = 600$ W

Safety area around the WPT structure

The experimental device measured here is perfectly safe as the magnetic field strength does not exceed $B = 5.166 \mu\text{T}$ at $P_{\text{output}} = 600 \text{ W}$ and $B = 4.178 \mu\text{T}$ at $P_{\text{output}} = 250 \text{ W}$. But these measurements have been conducted at the laboratory to insure a perfect safety of the people around it during the experiments, thus the output power has been voluntarily decreased to a lower value than the peak output power. In order to observe the effects of the real WPT system which can work at up to $P_{\text{output}} = 3 \text{ kW}$ at the laboratory, a basic power scaling has been applied to the currents in the coil and therefore to the output magnetic field strength measured. The resulting maps of the magnetic field strength are displayed on figure 5.19 along with the exposure limit at $f = 85 \text{ kHz}$ ($B < 27 \mu\text{T}$). A combination of the dataset at $P_{\text{output}} = 250 \text{ W}$ and $P_{\text{output}} = 600 \text{ W}$ has been scaled up to avoid the datapoints with the most uncertainty on the measured values.

Using the available experimental data, a consistent metamodel has been built ($LOO = 2.148 \cdot 10^{-3}$) for a scaled up B-field at $P_{\text{output}} = 3 \text{ kW}$. The resulting predictor is consistent enough to give us a safety area for the human body around the working WPT device (the safety area in 3D is displayed on figure 5.20). Further from the device (along the x axis), as expected, no need to worry about the B-field values. The main danger of the device is if someone is on top of it, which is impossible as the car should be there with a shielded frame to protect in the case of people seating inside the car while it's charging. Therefore the only recommendation which can be deduced from this analysis is the logical and basic one: do not get close to the device while it's working, one needs to step aside.

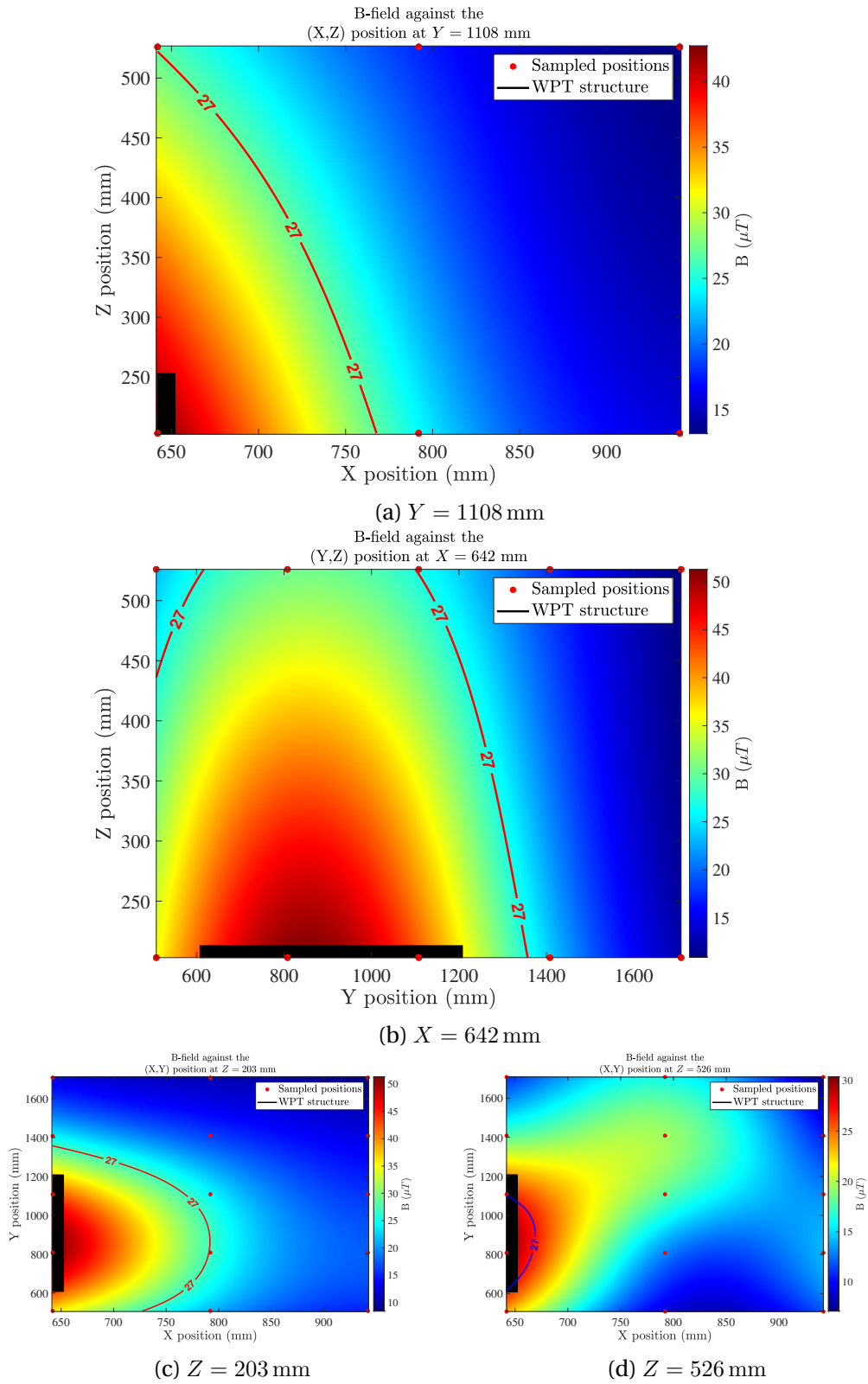


Fig. 5.19 Magnitude of the B-field predicted with the exposure limit for the experimental WPT structure (in black) on various cut planes for $P_{output} = 3$ kW (scaled up)

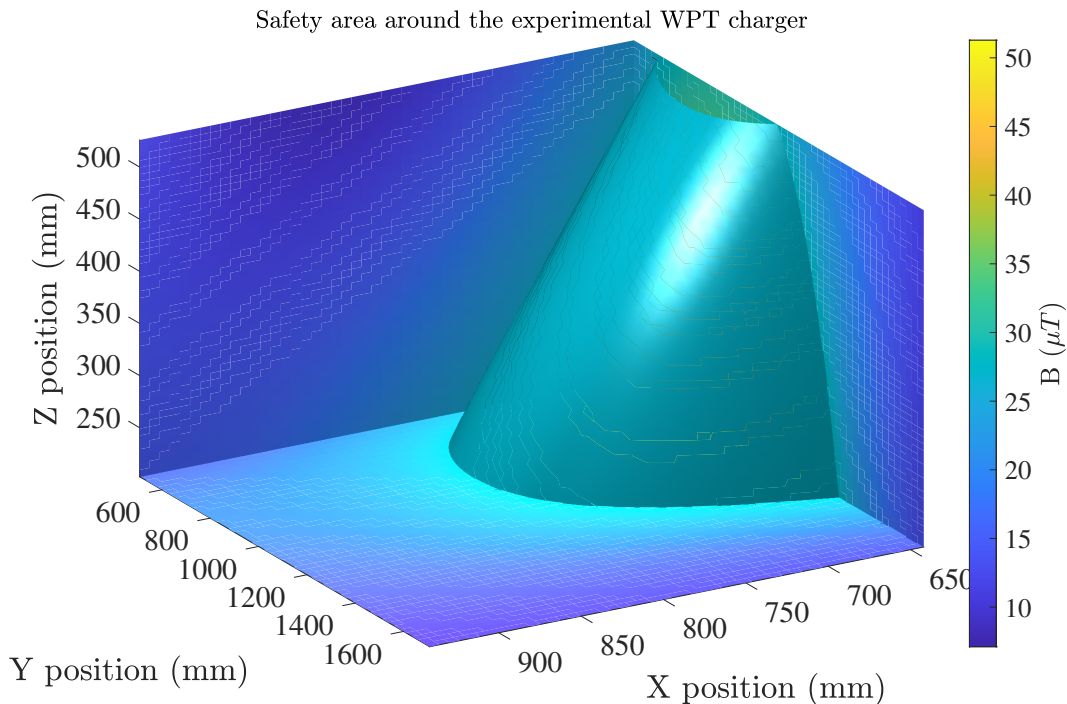


Fig. 5.20 Safety area ($B < 27 \mu\text{T}$) around the WPT structure at $P_{\text{output}} = 3 \text{ kW}$ (scaled up)

5.4 Conclusions

Our goal was here to demonstrate the usefulness of our active learning metamodelling algorithm and of metamodelling in general for complex electromagnetic problems in the case of human exposure. These analysis are more difficult to compute than classical problems as the magnetic field need to be computed in the first place then a voxel-based 3D human model can be placed within and the dosimetric analysis computed. Then, the results can be used to try out mitigation solutions or define safety area around high-power devices.

The algorithm has been first successful at estimating exposure around the simulated WPT3 (class Z3) from the Standard SAE J2954 on its worst case (maximum misalignment between coils). Even if the interest is of no use as the system is perfectly safe (the exposure factor didn't exceed 0.45), the methodology employed here can be of use for future exposure analysis

around high-power systems. The combination of the quad-tree algorithm for samples with Sim4Life for datapoints computation on a provided B-field managed to provide a consistent predictor for the exposure regarding the position of a crouching posture (worst posture) around the working WPT device. Then, this dosimetric protocol has been extended to a system where the human exposure problem is more critical: MFDC welding guns, another high-power system. By using just a simple model (planar coil) for the gun with a magnetic current pulse, a multi-frequency metamodel for the exposure factor on some critical tissues has been obtained for any position of the human body behind the gun. Using the corresponding predictor, some compliance safety areas around the device have been defined using the WPM for 8 particular tissues.

Our methodology based on metamodeling has been proven quite useful for fast and reliable computation in terms of exposure assessment. It proposed an alternative to existing time reducing solutions presented earlier (see section 5). The main advantages of using our metamodeling algorithms instead of other numerical methods is first its overall simplicity in its setup: the model definition itself is needed along with the input parameter space, once a consistent metamodel has been built, no additional computations are required. Then, the resulting predictor can be used easily for various other applications such as optimisation or global sensitivity analysis as detailed in chapter 4. But using the adaptive algorithm brings also a potential drawback as a tweak of the active learning parameters (ε and m) might be needed if different high-power systems, in terms of exposure scenario or model complexity, are to be studied. This would take several roll of the algorithm to compute a consistent metamodel, thus increasing the global computation time while still being lower than classical numerical methods.

Finally, metamodeling processes have been tried out on experimental data from a WPT coupling structure available at the laboratory. The dataset provided has been used to compute a consistent metamodel for the magnetic field strength around the working WPT device at $P_{output} = 600$ W. By scaling up low power results to $P_{output} = 3$ kW, a spatial definition of the classical ICNIRP limit at $f = 85$ kHz ($B < 27$ μ T) has been made possible.

Even if the measurements were limited, the analysis proved the possible use of surrogate models for experimental electromagnetic problems.

Chapter 6

Conclusion

This work presented the successful use of innovative non-intrusive stochastic methods known as surrogate models or metamodels, in the case of WPT systems. Considering the complexity of such systems, human exposure assessment and especially dosimetric analysis have been computed easily at a low computation cost using an adaptive PCK metamodeling algorithm. The core of this work relies on the development and application of the aforementioned algorithm. The choice of a PCK metamodel regarding other surrogate models available (notably Kriging and PCE) in the literature has been justified on various IPT systems. The adaptive sampling strategy has been chosen as a uniform quad-tree algorithm compared to other sequential space-filling strategies for minimizing as much as possible the calls of an expensive computational model. These choices have been made based on the analysis of several test functions which could have been taken completely differently.

Nonetheless, this algorithm has been validated several times on different input models. The output of the algorithm is a consistent metamodel along with its predictor which produces an accurate sensitivity analysis. First, an easy to solve analytical case of a dynamic WPT mutual inductance model has been treated successfully with a fast and accurate sensitivity analysis with few model calls. This led to initial thoughts on the definition of the two parameters of the algorithm: the local stopping criteria (the *LOO* threshold ε) and the global stopping criteria (the maximum number

of the initial domain division allowed m). Then, the algorithm has been confronted to a realistic WPT system computational model and managed to produce consistent metamodels for various parametric analysis of various dimensionalities: a six parameters road profile case has been analyzed ($LOO \simeq 3.002 \cdot 10^{-2}$, $n_{samples} = 65$) along with the dependency to four dimensions of the two rectangular coils ($LOO \simeq 1.410 \cdot 10^{-2}$, $n_{samples} = 17$). Both of this metamodels have been built with fairly low amount of input datapoints compared to their respective input dimensionality.

Therefore, our active learning metamodel algorithm has been extremely helpful to treat human exposure assessment at a low computation cost. Using it, a dosimetric methodology has been developed to define safety areas around first a simulated standardized WPT charger and in a second time a practical dynamic WPT system available in our research unit where experimental data have been collected on. Even with the inherent complexity of both the considered WPT models and the 3D voxelized human model, accurate sensitivity analysis and consistent metamodels have been computed with yet again a low number of samples. Even if the dosimetric analysis coupled with metamodelling process has been proven adequate for minimizing the total computation, such human exposure assessment were useless as both of the system have been found perfectly safe for bystander positions in their vicinity.

Hence why the knowledge acquired on our algorithm with the complex models treated before has been put to a better use: treat the human exposure of a system needier of such analysis. The case of MFDC spot welding guns have been investigated where crucial human exposure assessment is required for operators. An additional complexity is added compared to previous studies as the generated magnetic field is a pulse, which forces a multi-frequency analysis. The dosimetric methodology to compute safety areas, initially used on WPT systems, has been extended in order to treat the case of time-dependent electromagnetic problems. With the definition of an equivalent frequency-dependent conductivity for various tissues, a metamodel to deal with the exposure to a specific pulsed magnetic field has been successfully built.

Finally, the methodology developed here has been particularly useful for fast and reliable human exposure assessment, especially for computing safety areas (in 2D or 3D) for humans around various electromagnetic devices. The curse of dimensionality for our algorithm is easily tackled if a fairly low input dimensionality is considered. But once the human exposure problem exceeds 3 input parameters (see equation 4.1) for example, the potential maximum number of datapoints computed is close to 200 (with a maximum division $m = 2$) which represents almost 24 hours of computation time for the Duke model. Moreover, the various surrogate processes used throughout this work are considering outputs with rather minor irregularities and no discontinuities. The results could not be reproduced for output models with different behaviors such as non-differentiable functions or periodic functions.

This work opened many possibilities in the studies of human exposure around electromagnetic devices. A first development in our research group could be to integrate a detailed study of the exposure around the WPT system detailed in section 5.3. By measuring the three components of the B-field in the vicinity area instead of simply the magnitude, the dosimetric methodology developed in section 5.1.2 could be applied to this real system and metamodelling would be used for both mapping the magnetic field and computing the safety areas regarding various tissues. A wider interest could be to assess the safety of various household appliances regarding human exposure. Such hot topics recently raised the interest on the exposure of fetuses or person wearing medical implants. With the recent development of 5G, such methodology could greatly help in quantifying the interaction (and the potential danger) between human tissues and millimeter-wave technologies.

References

- [1] Ming Lu and Khai DT Ngo. “Comparison of passive shields for coils in inductive power transfer”. In: *2017 IEEE Applied Power Electronics Conference and Exposition (APEC)*. IEEE. 2017, pp. 1419–1424.
- [2] Project number 16ENG08 EURAMET. *MICEV (Metrology for inductive charging of electric vehicles)*. 2016. URL: <https://www.micev.eu/>.
- [3] Tsunenobu Kimoto and James A Cooper. *Fundamentals of silicon carbide technology: growth, characterization, devices and applications*. John Wiley & Sons, 2014.
- [4] Andrea Saltelli and Stefano Tarantola. “On the relative importance of input factors in mathematical models: safety assessment for nuclear waste disposal”. In: *Journal of the American Statistical Association* 97.459 (2002), pp. 702–709.
- [5] Qinxian Chelsea Curran, Douglas Allaire, and Karen E Willcox. “Sensitivity analysis methods for mitigating uncertainty in engineering system design”. In: *Systems Engineering* 21.3 (2018), pp. 191–209.
- [6] Max D Morris. “Factorial sampling plans for preliminary computational experiments”. In: *Technometrics* 33.2 (1991), pp. 161–174.
- [7] Hyunseok Oh et al. “Probabilistic lifetime prediction of electronic packages using advanced uncertainty propagation analysis and model calibration”. In: *IEEE Transactions on Components, Packaging and Manufacturing Technology* 6.2 (2016), pp. 238–248.
- [8] Donald E Livesay and Kun-Mu Chen. “Electromagnetic fields induced inside arbitrarily shaped biological bodies”. In: *IEEE Transactions on Microwave Theory and Techniques* 22.12 (1974), pp. 1273–1280.
- [9] World Health Organization. Radiation, Environmental Health, and World Health Organization. *Establishing a dialogue on risks from electromagnetic fields*. World Health Organization, 2002.
- [10] Kjell Hansson Mild et al. “Exposure of workers to electromagnetic fields. A review of open questions on exposure assessment techniques”. In: *International Journal of Occupational Safety and Ergonomics* 15.1 (2009), pp. 3–33.

- [11] Ben Greenebaum and Frank Barnes. *Bioengineering and biophysical aspects of electromagnetic fields*. CRC press, 2018.
- [12] Anders Ahlbom et al. “Possible effects of electromagnetic fields (EMF) on human health—opinion of the scientific committee on emerging and newly identified health risks (SCENIHR)”. In: *Toxicology* 246.2-3 (2008), pp. 248–50.
- [13] Camelia Gabriel, Azadeh Peyman, and Edwin H Grant. “Electrical conductivity of tissue at frequencies below 1 MHz”. In: *Physics in medicine & biology* 54.16 (2009), p. 4863.
- [14] Silvanus Phillips Thompson. “A physiological effect of an alternating magnetic field”. In: *Proceedings of the Royal Society of London. Series B, Containing Papers of a Biological Character* 82.557 (1910), pp. 396–398.
- [15] Sol M Michaelson. “Human exposure to nonionizing radiant energy—Potential hazards and safety standards”. In: *Proceedings of the IEEE* 60.4 (1972), pp. 389–421.
- [16] J Arthur Lazell. “Radiation Control for Health and Safety Act of 1968”. In: *Health Physics* 16.4 (1969), pp. 525–526.
- [17] An Act. “Occupational safety and health act of 1970”. In: *Public Law* 91 (1970), p. 596.
- [18] International Commission on Non-Ionizing Radiation Protection et al. “Guidelines for limiting exposure to time-varying electric, magnetic, and electromagnetic fields (up to 300 GHz)”. In: *Health physics* 74.4 (1998), pp. 494–522.
- [19] Jiali Lin et al. “ICNIRP Guidelines for limiting exposure to time-varying electric and magnetic fields (1 Hz to 100 kHz).” In: *Health physics* 99 (2010), pp. 818–836.
- [20] Michael H Repacholi. “WHO’s international EMF project”. In: *Radiation protection dosimetry* 83.1-2 (1999), pp. 1–4.
- [21] “IEEE Standard for Safety Levels with Respect to Human Exposure to Electric, Magnetic, and Electromagnetic Fields, 0 Hz to 300 GHz”. In: *IEEE Std C95.1-2019 (Revision of IEEE Std C95.1-2005/ Incorporates IEEE Std C95.1-2019/Cor 1-2019)* (2019), pp. 1–312. DOI: [10.1109/IEEESTD.2019.8859679](https://doi.org/10.1109/IEEESTD.2019.8859679).
- [22] International Commission on Non-Ionizing Radiation Protection et al. “Guidelines for limiting exposure to electromagnetic fields (100 kHz to 300 GHz)”. In: *Health physics* 118.5 (2020), pp. 483–524.
- [23] Nicolas Siauve et al. “Electromagnetic fields and human body: a new challenge for the electromagnetic field computation”. In: *COMPEL—The international journal for computation and mathematics in electrical and electronic engineering* (2003).

- [24] A Bossavit. “A theoretical approach to the question of biological effects of low frequency fields”. In: *IEEE transactions on magnetics* 29.2 (1993), pp. 1399–1402.
- [25] Oriano Bottauscio and R Conti. “Magnetically and electrically induced currents in human body models by ELF electromagnetic fields”. In: (1997).
- [26] Trevor W Dawson and Maria A Stuchly. “High-resolution organ dosimetry for human exposure to low-frequency magnetic fields”. In: *IEEE transactions on magnetics* 34.3 (1998), pp. 708–718.
- [27] Marie-Christine Gosselin et al. “Development of a new generation of high-resolution anatomical models for medical device evaluation: the Virtual Population 3.0”. In: *Physics in Medicine & Biology* 59.18 (2014), p. 5287.
- [28] PA Hasgall et al. “IT’IS Database for thermal and electromagnetic parameters of biological tissues Version 4.1”. In: (Feb. 2022).
- [29] Michael J Ackerman. “The visible human project”. In: *Proceedings of the IEEE* 86.3 (1998), pp. 504–511.
- [30] Tomoaki Nagaoka et al. “Development of realistic high-resolution whole-body voxel models of Japanese adult males and females of average height and weight, and application of models to radio-frequency electromagnetic-field dosimetry”. In: *Physics in Medicine & Biology* 49.1 (2003), p. 1.
- [31] Anthony V Fiacco. “Sensitivity analysis for nonlinear programming using penalty methods”. In: *Mathematical programming* 10.1 (1976), pp. 287–311.
- [32] Richard H McCuen. “The role of sensitivity analysis in hydrologic modeling”. In: *Journal of Hydrology* 18.1 (1973), pp. 37–53.
- [33] Etienne de Rocquigny, Nicolas Devictor, and Stefano Tarantola. *Uncertainty in industrial practice: a guide to quantitative uncertainty management*. John Wiley & Sons, 2008.
- [34] Jon C Helton. “Uncertainty and sensitivity analysis techniques for use in performance assessment for radioactive waste disposal”. In: *Reliability Engineering & System Safety* 42.2-3 (1993), pp. 327–367.
- [35] Jack PC Kleijnen. “Sensitivity analysis and related analyses: a review of some statistical techniques”. In: *Journal of statistical computation and simulation* 57.1-4 (1997), pp. 111–142.
- [36] H Christopher Frey and Sumeet R Patil. “Identification and review of sensitivity analysis methods”. In: *Risk analysis* 22.3 (2002), pp. 553–578.
- [37] Bertrand Iooss and Paul Lemaître. “A review on global sensitivity analysis methods”. In: *Uncertainty management in simulation-optimization of complex systems* (2015), pp. 101–122.

- [38] Ronald Christensen. *Linear models for multivariate, time series, and spatial data*. Vol. 1. Springer, 1991.
- [39] Andrea Saltelli and Ilya M Sobol. “About the use of rank transformation in sensitivity analysis of model output”. In: *Reliability Engineering & System Safety* 50.3 (1995), pp. 225–239.
- [40] Ilya M Sobol. “Sensitivity analysis for non-linear mathematical models”. In: *Mathematical modelling and computational experiment* 1 (1993), pp. 407–414.
- [41] RI Cukier, JH Schaibly, and Kurt E Shuler. “Study of the sensitivity of coupled reaction systems to uncertainties in rate coefficients. III. Analysis of the approximations”. In: *The Journal of Chemical Physics* 63.3 (1975), pp. 1140–1149.
- [42] Benjamin Auder and Bertrand Iooss. “Global sensitivity analysis based on entropy”. In: *Safety, reliability and risk analysis-Proceedings of the ESREL 2008 Conference*. 2008, pp. 2107–2115.
- [43] Claude Elwood Shannon. “A mathematical theory of communication”. In: *The Bell system technical journal* 27.3 (1948), pp. 379–423.
- [44] Imre Csiszár. “I-divergence geometry of probability distributions and minimization problems”. In: *The annals of probability* (1975), pp. 146–158.
- [45] Emanuele Borgonovo. “A new uncertainty importance measure”. In: *Reliability Engineering & System Safety* 92.6 (2007), pp. 771–784.
- [46] IM Sobol. “Quasi-monte carlo methods”. In: *Progress in Nuclear Energy* 24.1-3 (1990), pp. 55–61.
- [47] Curtis B Storlie and Jon C Helton. “Multiple predictor smoothing methods for sensitivity analysis: Description of techniques”. In: *Reliability Engineering & System Safety* 93.1 (2008), pp. 28–54.
- [48] Kai Cheng et al. “Surrogate-assisted global sensitivity analysis: an overview”. In: *Structural and Multidisciplinary Optimization* 61.3 (2020), pp. 1187–1213.
- [49] Michael D McKay, Richard J Beckman, and William J Conover. “A comparison of three methods for selecting values of input variables in the analysis of output from a computer code”. In: *Technometrics* 42.1 (2000), pp. 55–61.
- [50] Wojciech Jarosz et al. “Orthogonal array sampling for Monte Carlo rendering”. In: *Computer Graphics Forum (Proceedings of EGSR)* 38.4 (July 2019), pp. 135–147. DOI: [10/gf6rx5](https://doi.org/10/gf6rx5).
- [51] Mervyn Stone. “Cross-validation and multinomial prediction”. In: *Biometrika* 61.3 (1974), pp. 509–515.
- [52] J-M Bourinet. “Rare-event probability estimation with adaptive support vector regression surrogates”. In: *Reliability Engineering & System Safety* 150 (2016), pp. 210–221.

- [53] G Gary Wang and Songqing Shan. “Review of metamodeling techniques in support of engineering design optimization”. In: (2007).
- [54] Christian G Bucher and Ulrich Bourgund. “A fast and efficient response surface approach for structural reliability problems”. In: *Structural safety* 7.1 (1990), pp. 57–66.
- [55] Xiaopeng Luo, Zhenzhou Lu, and Xin Xu. “Reproducing kernel technique for high dimensional model representations (HDMR)”. In: *Computer Physics Communications* 185.12 (2014), pp. 3099–3108.
- [56] Herschel Rabitz and Ömer F Aliş. “General foundations of high-dimensional model representations”. In: *Journal of Mathematical Chemistry* 25.2 (1999), pp. 197–233.
- [57] Romain SC Lambert et al. “Global sensitivity analysis using sparse high dimensional model representations generated by the group method of data handling”. In: *Mathematics and Computers in Simulation* 128 (2016), pp. 42–54.
- [58] Corinna Cortes and Vladimir Vapnik. “Support-vector networks”. In: *Machine learning* 20.3 (1995), pp. 273–297.
- [59] Kai Cheng et al. “Mixed kernel function support vector regression for global sensitivity analysis”. In: *Mechanical Systems and Signal Processing* 96 (2017), pp. 201–214.
- [60] Rolland L Hardy. “Multiquadric equations of topography and other irregular surfaces”. In: *Journal of geophysical research* 76.8 (1971), pp. 1905–1915.
- [61] Mattias Björkman and Kenneth Holmström. “Global optimization of costly nonconvex functions using radial basis functions”. In: *Optimization and Engineering* 1.4 (2000), pp. 373–397.
- [62] Daniel G Krige. “A statistical approach to some basic mine valuation problems on the Witwatersrand”. In: *Journal of the Southern African Institute of Mining and Metallurgy* 52.6 (1951), pp. 119–139.
- [63] Jean Lefebvre et al. “Prediction from wrong models: the Kriging approach”. In: *IEEE Antennas and propagation Magazine* 38.4 (1996), pp. 35–45.
- [64] Jeremy E Oakley and Anthony O’Hagan. “Probabilistic sensitivity analysis of complex models: a Bayesian approach”. In: *Journal of the Royal Statistical Society: Series B (Statistical Methodology)* 66.3 (2004), pp. 751–769.
- [65] Pierrick Hamel et al. “Kriging method combined with GISM to generate ionospheric scintillation map”. In: *The 8th European Conference on Antennas and Propagation (EuCAP 2014)*. IEEE. 2014, pp. 2693–2697.
- [66] Norbert Wiener. “The homogeneous chaos”. In: *American Journal of Mathematics* 60.4 (1938), pp. 897–936.

- [67] Géraud Blatman and Bruno Sudret. “Efficient computation of global sensitivity indices using sparse polynomial chaos expansions”. In: *Reliability Engineering & System Safety* 95.11 (2010), pp. 1216–1229.
- [68] Roland Schobi, Bruno Sudret, and Joe Wiart. “Polynomial-chaos-based Kriging”. In: *International Journal for Uncertainty Quantification* 5.2 (2015).
- [69] Luiz Lebensztajn et al. “Kriging: A useful tool for electromagnetic device optimization”. In: *IEEE Transactions on Magnetics* 40.2 (2004), pp. 1196–1199.
- [70] Norman Haussmann et al. “Efficient Assessment of the Human Exposure to Low-Frequency Magnetic Fields Based on Free Space Field Measurements”. In: *Compumag 2021* PD-P2.17 (2022).
- [71] Peter Offermann and Kay Hameyer. “A polynomial chaos meta-model for non-linear stochastic magnet variations”. In: *COMPEL-The international journal for computation and mathematics in electrical and electronic engineering* (2013).
- [72] Pierric Kersaudy et al. “A new surrogate modeling technique combining Kriging and polynomial chaos expansions—Application to uncertainty analysis in computational dosimetry”. In: *Journal of Computational Physics* 286 (2015), pp. 103–117.
- [73] Gladwin Jos Kurupasseril Tomy and Kalarickaparambil Joseph Vinoy. “A fast polynomial chaos expansion for uncertainty quantification in stochastic electromagnetic problems”. In: *IEEE Antennas and Wireless Propagation Letters* 18.10 (2019), pp. 2120–2124.
- [74] Susana Naranjo-Villamil et al. “Lightning-Induced Magnetic Fields Inside Grid-Like Shields: An Improved Formula Complemented by a Polynomial Chaos Expansion”. In: *IEEE Transactions on Electromagnetic Compatibility* 63.2 (2021), pp. 558–570.
- [75] Yao Pei et al. “Multiobjective optimization based on polynomial chaos expansions in the design of inductive power transfer systems”. In: *COMPEL-The international journal for computation and mathematics in electrical and electronic engineering* (2022).
- [76] Stefano Marelli and Bruno Sudret. *UQLab: A framework for uncertainty quantification in Matlab*. American Society of Civil Engineers, 2014.
- [77] Thomas J Santner et al. *The design and analysis of computer experiments*. Vol. 1. Springer, 2003.
- [78] Vincent Dubourg. “Adaptive surrogate models for reliability analysis and reliability-based design optimization”. PhD thesis. Université Blaise Pascal-Clermont-Ferrand II, 2011.
- [79] Carl Edward Rasmussen and Hannes Nickisch. “Gaussian processes for machine learning (GPML) toolbox”. In: *The Journal of Machine Learning Research* 11 (2010), pp. 3011–3015.

- [80] Oliver G Ernst et al. “On the convergence of generalized polynomial chaos expansions”. In: *ESAIM: Mathematical Modelling and Numerical Analysis* 46.2 (2012), pp. 317–339.
- [81] Bruno Sudret. “Uncertainty propagation and sensitivity analysis in mechanical models—Contributions to structural reliability and stochastic spectral methods”. In: *Habilitation à diriger des recherches, Université Blaise Pascal, Clermont-Ferrand, France* 147 (2007), p. 53.
- [82] Roland Schöbi, Bruno Sudret, and Stefano Marelli. “Rare event estimation using polynomial-chaos kriging”. In: *ASCE-ASME Journal of Risk and Uncertainty in Engineering Systems, Part A: Civil Engineering* 3.2 (2016), p. D4016002.
- [83] Rui Teixeira et al. “Reliability analysis using a multi-metamodel complement-basis approach”. In: *Reliability Engineering & System Safety* 205 (2021), p. 107248.
- [84] Bruno Sudret. “Global sensitivity analysis using polynomial chaos expansions”. In: *Reliability engineering & system safety* 93.7 (2008), pp. 964–979.
- [85] Vincenzo Cirimele. “Design and Integration of a Dynamic IPT System for Automotive Applications”. 2017SACLS032. PhD thesis. Université Paris-Saclay, Politecnico di Torino, 2017. URL: <http://www.theses.fr/2017SACLS032/document>.
- [86] Carl Edward Rasmussen and C Williams. “Gaussian processes for machine learning, ser. Adaptive computation and machine learning”. In: *Cambridge, MA, USA: MIT Press* 38 (2006), pp. 715–719.
- [87] Walter Gautschi. “Is the recurrence relation for orthogonal polynomials always stable?” In: *BIT Numerical Mathematics* 33.2 (1993), pp. 277–284.
- [88] Haitao Liu, Yew-Soon Ong, and Jianfei Cai. “A survey of adaptive sampling for global metamodeling in support of simulation-based complex engineering design”. In: *Structural and Multidisciplinary Optimization* 57.1 (2018), pp. 393–416.
- [89] Ping Jiang et al. “A novel sequential exploration-exploitation sampling strategy for global metamodeling”. In: *IFAC-PapersOnLine* 48.28 (2015), pp. 532–537.
- [90] André Elisseeff, Massimiliano Pontil, et al. “Leave-one-out error and stability of learning algorithms with applications”. In: *NATO science series sub series iii computer and systems sciences* 190 (2003), pp. 111–130.
- [91] Vijaya K Devabhaktuni and Qi-Jun Zhang. “Neural Network training-driven adaptive sampling algorithm for microwave modeling”. In: *2000 30th European Microwave Conference*. IEEE. 2000, pp. 1–4.

- [92] Franz Aurenhammer. “Voronoi diagrams—a survey of a fundamental geometric data structure”. In: *ACM Computing Surveys (CSUR)* 23.3 (1991), pp. 345–405.
- [93] Shengli Xu et al. “A robust error-pursuing sequential sampling approach for global metamodeling based on voronoi diagram and cross validation”. In: *Journal of Mechanical Design* 136.7 (2014), p. 071009.
- [94] Raphael A Finkel and Jon Louis Bentley. “Quad trees a data structure for retrieval on composite keys”. In: *Acta informatica* 4.1 (1974), pp. 1–9.
- [95] Thierry Braconnier et al. “Towards an adaptive POD/SVD surrogate model for aeronautic design”. In: *Computers & Fluids* 40.1 (2011), pp. 195–209.
- [96] Jack PC Kleijnen and WCM Van Beers. “Application-driven sequential designs for simulation experiments: Kriging metamodeling”. In: *Journal of the operational research society* 55.8 (2004), pp. 876–883.
- [97] IM Sobol’. “On the systematic search in a hypercube”. In: *SIAM Journal on Numerical Analysis* 16.5 (1979), pp. 790–793.
- [98] John H Halton. “On the efficiency of certain quasi-random sequences of points in evaluating multi-dimensional integrals”. In: *Numerische Mathematik* 2.1 (1960), pp. 84–90.
- [99] Kateryna Stoyka et al. “Behavioral Models for the Analysis of Dynamic Wireless Charging Systems for Electrical Vehicles”. In: *2020 IEEE Int. Symp. on Circuits and Systems (ISCAS)*. Oct. 2020.
- [100] Kateryna Stoyka et al. “Behavioral modeling of Wireless Power Transfer System coils”. In: *Mathematics and Computers in Simulation* 183 (2021), pp. 208–220.
- [101] Robin P Nicolai et al. “Automated response surface methodology for stochastic optimization models with unknown variance”. In: *Proceedings of the 2004 Winter Simulation Conference, 2004*. Vol. 1. IEEE. 2004.
- [102] ES Siah et al. “Fast parameter optimization using Kriging meta-modeling [antenna EM modeling/simulation]”. In: *IEEE Antennas and Propagation Society International Symposium. Digest. Held in conjunction with: USNC/CNC/URSI North American Radio Sci. Meeting (Cat. No. 03CH37450)*. Vol. 2. IEEE. 2003, pp. 76–79.
- [103] Yao Pei et al. “Fast Shielding Optimization of an Inductive Power Transfer System for Electric Vehicles”. In: *IEEE Access* 10 (2022), pp. 91227–91234.
- [104] Charles Boulitrop, Marc Lambert, and Sándor Bilicz. “Polynomial chaos within the frame of non-destructive testing”. In: *2021 XXXIVth General Assembly and Scientific Symposium of the International Union of Radio Science (URSI GASS)*. IEEE, pp. 1–4.

- [105] B. Sudret and C.V. Mai. “Computing derivative-based global sensitivity measures using polynomial chaos expansions”. In: *Reliability Engineering & System Safety* 134 (2015), pp. 241–250. ISSN: 0951-8320. DOI: <https://doi.org/10.1016/j.res.2014.07.009>. URL: <http://www.sciencedirect.com/science/article/pii/S0951832014001641>.
- [106] M. Abramowitz and I.A. Stegun. *Handbook of Mathematical Functions with Formulas, Graphs, and Mathematical Tables*. Applied Mathematics Series. U.S. Government Printing Office, 1948. URL: <https://books.google.fr/books?id=RSC002LFbY0C>.
- [107] J. Kennedy and R. Eberhart. “Particle swarm optimization”. In: *Proceedings of ICNN'95 - International Conference on Neural Networks*. Vol. 4. Nov. 1995, pp. 1942–1948. DOI: [10.1109/ICNN.1995.488968](https://doi.org/10.1109/ICNN.1995.488968).
- [108] Mathew M Noel. “A new gradient based particle swarm optimization algorithm for accurate computation of global minimum”. In: *Applied Soft Computing* 12.1 (2012), pp. 353–359.
- [109] Luc Pronzato and Werner G Müller. “Design of computer experiments: space filling and beyond”. In: *Statistics and Computing* 22.3 (2012), pp. 681–701.
- [110] Zhenliang Yu et al. “RCA-PCK: A new structural reliability analysis method based on PC-Kriging and radial centralized adaptive sampling strategy”. In: *Proceedings of the Institution of Mechanical Engineers, Part C: Journal of Mechanical Engineering Science* 235.17 (2021), pp. 3424–3438.
- [111] E Yavolovskaya et al. “Simulation of human exposure to electromagnetic fields of inductive wireless power transfer systems in the frequency range from 1 Hz to 30 MHz”. In: *2016 International Symposium on Electromagnetic Compatibility-EMC EUROPE*. IEEE, 2016, pp. 491–496.
- [112] Alice CONCHIN GUBERNATI. “Human exposure to low-frequency magnetic field: new methodologies for numerical dosimetry”. PhD thesis. Politecnico di Torino, 2022. URL: <http://hdl.handle.net/11583/2968460>.
- [113] Trevor W Dawson, Krys Caputa, and Maria A Stuchly. “Electric fields induced in humans and rodents by 60 Hz magnetic fields”. In: *Physics in Medicine & Biology* 47.14 (2002), p. 2561.
- [114] Aldo Canova et al. “Exposure of working population to pulsed magnetic fields”. In: *IEEE Transactions on Magnetism* 46.8 (2010), pp. 2819–2822.
- [115] Ping-Ping Ding et al. “Evaluation of electromagnetic fields in human body exposed to wireless inductive charging system”. In: *IEEE Transactions on Magnetism* 50.2 (2014), pp. 1037–1040.
- [116] G Gary Wang. “Adaptive response surface method using inherited latin hypercube design points”. In: *J. Mech. Des.* 125.2 (2003), pp. 210–220.

- [117] SAE Standard. “J2954, wireless power transfer for light-duty plug-in/electric vehicles and alignment methodology”. In: *Accessed: Feb 9* (2016), p. 2019.
- [118] Fabio Freschi, Luca Giaccone, and Maurizio Repetto. “Algebraic formulation of nonlinear surface impedance boundary condition coupled with BEM for unstructured meshes”. In: *Engineering Analysis with Boundary Elements* 88 (Mar. 2018), pp. 104–114. ISSN: 0955-7997. DOI: [10.1016/J.ENGANABOUND.2017.12.008](https://doi.org/10.1016/j.enganabound.2017.12.008).
- [119] Takuya Shimamoto, Ilkka Laakso, and Akimasa Hirata. “In-situ electric field in human body model in different postures for wireless power transfer system in an electrical vehicle”. In: *Physics in medicine & biology* 60.1 (2014), p. 163.
- [120] Valerio De Santis, Luca Giaccone, and Fabio Freschi. “Influence of Posture and Coil Position on the Safety of a WPT System While Recharging a Compact EV”. In: *Energies* 14.21 (2021), p. 7248.
- [121] Aldo Canova, Fabio Freschi, and Luca Giaccone. “How safe are spot welding guns to use?: An analysis of occupational exposure to their magnetic field”. In: *IEEE Industry Applications Magazine* 24.3 (2018), pp. 39–47.
- [122] Aldo Canova et al. “A simplified procedure for the exposure to the magnetic field produced by resistance spot welding guns”. In: *IEEE Transactions on Magnetics* 52.3 (2015), pp. 1–4.
- [123] Kari Jokela. “Restricting exposure to pulsed and broadband magnetic fields.” In: *Health physics* 79.4 (2000), pp. 373–388.
- [124] J Patrick Reilly, Vanda T Freeman, and Willard D Larkin. “Sensory effects of transient electrical stimulation-evaluation with a neuro-electric model”. In: *IEEE transactions on biomedical engineering* 12 (1985), pp. 1001–1011.
- [125] Arthur W Guy et al. “Determination of electric current distributions in animals and humans exposed to a uniform 60-Hz high-intensity electric field”. In: *Bioelectromagnetics: Journal of the Bioelectromagnetics Society, The Society for Physical Regulation in Biology and Medicine, The European Bioelectromagnetics Association* 3.1 (1982), pp. 47–71.
- [126] Luca Giaccone. “Compliance of non-sinusoidal or pulsed magnetic fields generated by industrial sources with reference to human exposure guidelines”. In: *2020 International Symposium on Electromagnetic Compatibility-EMC EUROPE*. IEEE. 2020, pp. 1–6.
- [127] Fabio Freschi, Luca Giaccone, and Massimo Mitolo. “Arc welding processes: an electrical safety analysis”. In: *IEEE Transactions on Industry Applications* 53.2 (2016), pp. 819–825.
- [128] Wassim Kabbara et al. “WIRELESS CHARGING SYSTEM FOR AN IN-MOTION EV”. In: *INTERNATIONAL CONFERENCE ON MOBILITY CHALLENGES*. 2021.

Titre : Métamodélisation pour le calcul rapide d'exposition des personnes aux systèmes haute puissance

Mots clés : Analyse de sensibilité, transfert de puissance inductif, exposition des personnes

Résumé : Les systèmes de transfert de puissance inductifs (WPT) représentent un atout majeur dans la course au développement des véhicules électriques. Un tel système en fonctionnement génère des niveaux de champs magnétiques importants susceptibles d'être dangereux pour les humains à proximité. Ainsi, lors du dimensionnement de nouveaux systèmes WPT, l'exposition des personnes doit être quantifiée en adéquation avec les standards et normes existantes.

Les travaux présentés ici démontrent l'utilisation de méthodes stochastiques non-intrusives pour construire des prédicteurs de modèles numériques complexes (à coûts de calcul élevés). Le prédicteur est un métamodèle, une simple fonction analytique à bas coût de calcul qui peut être utilisé à la place du modèle réel pour calculer des analyses de sensibilités ou optimiser le système.

Partant d'observations sur des métamodèles simples de systèmes WPT, un algorithme d'apprentissage itératif a été développé afin de construire un estimateur précis de la sortie d'un modèle complexe de WPT à bas coût de calcul. L'utilisation de cet algorithme a été validé sur divers cas: estimation d'inductance mutuelle pour système WPT dynamique, dimensionnement de ferrites par optimisation...

Enfin, en couplant cet algorithme à des modèles 3D de corps humain, une méthodologie a été développée pour une analyse dosimétrique à bas coût de l'exposition des personnes à un système WPT (modélisation et expérience). Cette méthodologie a été étendue avec succès à un système générant des impulsions magnétiques, un pistolet de soudure moyenne fréquence, un système industriel plus complexe à étudier.

Title : Metamodel-based methodology for fast prediction of human exposure to high power systems

Keywords : Sensitivity analysis, inductive power transfer, human exposure

Abstract : Wireless power transfer systems (WPT) are a key factor in the development of electric mobility. Such high power systems create a high level of magnetic field in the vicinity area, which can be dangerous for operators or bystanders. Thus, when designing new WPT systems, the human exposure needs to be properly assessed in order to be compliant with the current standards and guidelines.

The work presented here used non-intrusive stochastic tools to build a consistent predictor of complex computational models. The resulting predictor is a metamodel which is simply an analytical function that can be used afterwards to perform fast computation on the outputs of the real model such as Sobol'-based sensitivity analysis or optimization.

Based on initial observations on basic metamodels for both simplified and realistic WPT systems, an active learning metamodeling algorithm has been developed to build consistent predictor and perform accurate sensitivity analysis at a low computation cost. The algorithm has been validated for various cases: dynamic WPT system, ferrite...

Finally, a dosimetric methodology for assessing the safety of WPT systems at a low computation cost, using the adaptive algorithm coupled with a voxelized 3D human model, has been developed (simulated and real WPT system). The methodology has been applied to a system needier of human exposure assessment: mid-frequency Direct Current welding guns, treating the case of exposure to a pulsed magnetic field.